Synthesis and Thermo-Mechanical Properties of Sol-Gel Derived Zirconia Toughened Alumina Nanocomposite

A thesis submitted in fulfillment of the requirements for the Doctor of Philosophy in Ceramic Engineering

by

DEBASISH SARKAR

DEPARTMENT OF CERAMIC ENGINEERING
NATIONAL INSTITUTE OF TECHNOLOGY
ROURKELA – 769 008, ORISSA (INDIA)

23rd February 2007

ACKNOWLEDGEMENT

In the researching and writing of this thesis I have been helped by a great many people in many ways, only a few of whom I can acknowledge on this page.

I would first like to thank my supervisor, Prof. Sukumar Adak, for his encouragement, guidance, and confidence in me. Secondly, this work could not have been completed without the invaluable advice and assistance from Prof. N. K. Mitra (Co-Supervisor), Emeritus Professor, Ceramic Engineering Division, Department of Chemical Technology, University of Calcutta, Kolkata. He generously has given me the fundamental knowledge and analysis of chemical synthesis process as well as thermo-mechanical characterization.

I express my heartfelt thanks to Prof. S. K. Sarangi, Director, NIT Rourkela for providing the facilities to carry out this investigation.

There are many other colleagues and students who I would like to thank for practical assistance, discussion, advice and friendship: Prof. S. Bhattacharyya, Prof. R.C. Behera, Prof. J. Bera, Deepak and Sambarta. I am indebted to my family and friends for their love, encouragement, understanding and patience during this long journey.

Most especially I would like to thank my wife Shubhra, son Achyut and my parents, for their unstinting support throughout, which kept me going to the end. I would also like to acknowledge the support of Advanced Engineering Group of Korea Research Institute of Science and Standards (KRISS), South Korea. Access to their Mechanical and Microscopy Laboratory was provided by the Technical Education Quality Improvement Program (TEQIP), which was funded by World Bank.

Above all, I thank our saving Lord Krishna for giving me all these people to help and encourage me, and for the skills and opportunity to complete this thesis.

(**DEBASISH SARKAR**)

P R E F A C E

Chapter – I introduces the topic and background of the existing field. **Chapter – II** deals with detailed literature review. Attempts have been made to systematically classify the available information under different sections. This chapter incorporates background information to assist in understanding the aims and results of this investigation, and also reviews recent reports by other investigators with which these results can be compared. The review finds unresolved questions in the literature that can't be answered by a single research work. **Chapter – III** deals with the objectives of the present investigation. **Chapter – IV** deals with the detail experimental process related to this research work. **Chapter – V** deals with the results and discussion systematically with respect to powder synthesis, characterization, densification study and evaluation of thermo-mechanical properties. **Chapter – V**I summarizes the conclusions, whereas, the **Chapter – VII** illustrates the possibility of Future Works.

A complete list of references has been given towards the end of the thesis. Finally, a concise list of publications in-peer reviewed international journals related to present research work as well as other selected publications is attached at the end.

Table of Content

List of Figures

List of Tables

ABSRACT

Al_2O_3-ZrO_2 composite precursor powder containing 5-15mol% ZrO_2 is prepared by wet chemical route. The washed gel containing pseudoboehmite and amorphous zirconia are characterized with respect to DTA/TG, XRD and IR spectroscopy. In the calcined powder phase evolution of Al_2O_3 follows the sequence: pseudoboehmite → bayerite → boehmite → γ-Al_2O_3 → θ-Al_2O_3 → α-Al_2O_3; while that of ZrO_2 follows amorphous ZrO_2 → t-ZrO_2 → (t + m)-ZrO_2. However, the crystallization behavior of aluminum-hydroxide is somewhat affected with addition of zirconia. FTIR study reveal the number of M-OH and M-O bond increases on increasing mol% of ZrO_2 due to a change in the cationic charge of the composite powder. The formation of amorphous material before crystallization can also be predicted from TEM study, where particle exhibits different morphology; and show smooth, distinct and faceted surfaces at different temperature. A bimodal particle size distribution is observed because of both unagglomerated and partial agglomerated particles in the range from15 to 210nm for highest zirconia content, however, the specific surface area of powder decreases with increasing zirconia content. The addition of 5wt% uncalcined precursor enhances the consolidation process. The sintered zirconia toughened alumina nano-composite with 98% relative density has been achieved at 1550^{o}C for 4h. The average grain size ratio d_{Al2O3}/d_{ZrO2} varies in between 4.35 for Al_2O_3-5ZrO_2 and 2.29 for Al_2O_3-15ZrO_2, whereas average grain size of alumina and zirconia in Al_2O_3-10ZrO_2 composite are 360nm and 125nm respectively. EPMA confirms the near uniform distribution of zirconia particles in the alumina matrix. For homogenous dispersion of ZrO_2 in Al_2O_3, the optimum amount of ZrO_2 is found to be 10mol% and up to the critical amount of ZrO_2 addition, flexural strength and fracture toughness increase and the size of the intergranular zirconia strongly influences these properties. The room temperature fracture strength of these composite varies within ~500 to 700MPa, but drastic decrease of high temperature strength for lowest zirconia containing specimen is observed above 600^{0}C, where transformation toughening is no longer effective. The elastic modulus and hardness, both the properties decrease with ZrO_2 content. Thermal shock study reveals the retained flexural strength varies with zirconia content. The hystersis effect in the dilatation curve due to t→m transformation is also influenced by the grain size of ZrO_2.

Keywords: Sol-Gel, Alumina, Zirconia, ZTA, DTA, FTIR, XRD, TEM, SEM, Hardness, Fracture Toughness, Transformation Toughening, Elasticity, Thermal Shock, Flexural Strength, CTE.

To my Parents, Wife
and
Son Achyut

CHAPTER 1

1.0. INTRODUCTION

The demand for ceramic materials over metals is increasing. The application of ceramics varied from conventional/traditional to the more advanced fields like ball-bearing, automobile appliances, turbine blades, grinding media, cutting tools, space shuttles, radome of missiles to bio-implantations. The demand for a particular type of material largely depends on its applications. The main disadvantage of ceramic materials is relatively low fracture toughness; and different schools are engaged to work out the same. Conventionally well-accepted material such as zirconia can enhance the fracture properties of several oxide and non-oxide ceramics. Among other Zirconia Toughened Ceramics (ZTC), Zirconia Toughened Alumina (ZTA) has enormous potential for application in the field of structural ceramics and its abrasion resistance is three to four times higher compare with the pure alumina. Hence, several researchers are working in this field since three decade to improve different physico-chemical properties of it; specially thermal and mechanical.

Zirconia particles can be embedded in a variety of different matrices to form transformation-toughened ceramics provided the zirconia particles have a sufficiently small size, may be in submicron or below. Transformation-toughened materials include Al_2O_3, mullite, Si_3N_4, spinel, forsterite, glass, zircon, MgO etc. Requirements are that the matrix will not react with the ZrO_2 or vice-versa and that the matrix has sufficiently high elastic modulus to maintain a low M_s (martensitic transformation) temperature[1]. Zirconia Toughened Ceramics (ZTC) is generally formed by either mixing zirconia powder with the matrix powder and sintering or chemically preparing powder of mixed composition, for instance, by sol-gel technique. Most of the previous researchers have pointed out that the developed irregular intragranular zirconia particles within alumina grain have higher magnitude of stress concentration compare to spherical intergranular particles in alumina matrix. In this contrast, it can be emphasized that the enhancement of transformation toughening effect of ZTC depends strictly on distribution of zirconia particles. Hence, controlling of intragranular and/or intergranular ZrO_2 in matrix is a significant issue, when sintered specimens are densified either from chemical route or mixed powder technique.

Usually, zirconia particles are likely to separate from each other and grow during sintering. However, evidence suggests that zirconia particles are mobile in nature and move within the grain boundary of the matrix. The constraining stresses of the composite are smaller since the elastic moduli are less with increasing ZrO_2 content and agglomeration. The increased volume fraction of zirconia is also responsible to reduce the stability of the tetragonal phase[2]. The presence of dispersed tetragonal zirconia particles in the matrix can affect the strength and toughness of the material in two ways: (A) the stress field of a crack can initiate the martensitic transformation and compressive stress on the crack surface is developed due to the expansion of transformed particles against the matrix, and (B) the transformation may take place near the surface of the macroscopic piece due to surface grinding and result in a compressive surface which leads to higher strength values. Hence, an optimum amount of zirconia addition is expected to retain the favorable amount of tetragonal content which can enhance the thermal and mechanical properties of ZTC without any grain growth during sintering.

Among ZTC, ZTA exhibits a considerable improvement in strength and more importantly toughness. Interests in the ZTA also evolved in attempts to alleviate the problem of the loss of transformation toughening with increase in temperature and to enhance the fracture strength at elevated temperature. The modest and variable results can be attributed to various degrees of toughening contributed by the stress-induced transformation and by microcracking in ZTA materials. This is governed by the ability to retention of the tetragonal phase after processing and initiates the transformation during fracture. As a result, one needs to be able to characterize the various thermo-mechanical parameters contributing to the tetragonal phase retention and the ability to transform it. However, increase in tetragonal phase grain size of TZP ceramics with addition of yttria and ceria increase both the M_s temperature and the fracture toughness of these materials[3]. The grain-size dependent toughening is found to be associated with the increase in the M_s temperature with the increase in size of the tetragonal-phase precipitates and grains. In alumina-zirconia system, it is observed that the M_s temperature varies with the average zirconia grain size as well as grain size distribution[4]. Therefore, changes in grain size (and size distribution) can be a source of variations in the fracture toughness. At the same time, one ought to be able to optimize the fracture resistance of ceramics containing tetragonal grains by judiciously controlling the ZrO_2 grain size. Hence, synchronization of zirconia grain size and distribution within the alumina matrix is an important aspect to develop the ZTA composite material.

Compared to conventional powder mixing process, the chemical synthesis of ceramic materials from solution and its thermo-mechanical properties evaluation has been an interesting area of research from technical aspects since two decades. Solution-based routes have a number of distinguishing characteristics. All such routes begin with chemically reactive precursors, containing the components that are to be incorporated into the final product. The ease, by which many precursor chemicals can be purified, in comparison to oxide powders, makes chemical routes highly attractive for preparing ceramics where stoichiometry must be closely controlled. It is also pointed out that the importance of reaction chemistry and the structure of intermediate non-crystalline and/or crystalline materials on the structure and properties of the product cannot be under-emphasized. Therefore, in order to control the properties of the product, it is important to understand these aspects at each and every stages of the process. The most of the chemical routes are non-equilibrium in nature and occur at much lower temperature than conventional ceramic powder processing. The control over reaction kinetics provided by this type of reaction allows preparation of various metastable phases that cannot be observed by other routes. Furthermore, this approach also permits the synthesis of materials that are only stable at relatively low temperatures.

Chemical routes are advantageous because processing may take place at lower temperatures, reducing effective costs and allowing better control over the particle morphology; and even leading to entirely different properties. Excellent control over composition can be achieved, most notably in the preparation of multi-component oxides that are homogenous at a near-atomic scale. Monolithic with a gradient composition is also possible to prepare. A range of mechanisms allow excellent control over porosity and other meso-structures, and a very wide range of densities can be achieved. Different processes can produce ceramic bodies that are very close to theoretical density after sintering or extremely low-density aerogels. Finally, in many routes the oxide can be formed into a wide range of shapes either as an intermediate stage or to form a final product, without firing.

On the basis of the above findings and importance, the particular interest of this study was to develop a series of Al_2O_3-ZrO_2 composites through chemical route. The purpose also was to develop such composite from the combination of uncalcined precursor powder and calcined precursor, which provide excellent thermo-mechanical response under stresses.

In brief, present investigation is an attempt to achieve the series of zirconia (5-15 mol%) dispersed alumina precursor powders from multiphase hydrogel systems of Al and Zr-hydroxides, which has been prepared from their inorganic salts following chemical

route. The formed hydrogel is aged for proper growth and orientation at room temperature followed by drying at controlled temperature to minimize the agglomeration. The orientation, transformation and particle size/morphology of these hydroxide bonds are affected by hydroxide content. The effect is interpreted by Fourier Transform Infrared (FTIR), Differential Thermal Analysis (DTA), Thermo Gravimetric (TG) and X-Ray Diffractometer (XRD) analysis. The sol-gel derived precursor powders are shaped with 5wt% of corresponding uncalcined precursor powders instead of the addition of any organic binder or additives through uniaxial pressing followed by cold isostatic pressing, and pressureless sintering are carried out systematically in muffle furnace and the microstructural characterization is evaluated through electron microscopy techniques (SEM and TEM). Finally, the thermal and mechanical properties of a series of this composite material are investigated; and the obtained results are correlated.

Publication: Recently, parts of this thesis have been published in form of four peer-reviewed international journal papers. Significant results of *Chapter 5.1* to *5.3* sections were produced three publications in different journals, such as '*Composite Part A: Applied Science and Technology'*, '*Ceramics International'* and '*Journal of Material Science: Nano–Special Issue'*. However, part of the *Chapter 5.4* was published in the journal of '*Ceramics International'*. Presumably, compilation of important results and discussion on overall analysis will gather another two manuscripts within near future.

CHAPTER 2

2.0. LITERATURE REVIEW

The literature review is divided into four major sections. Section 2.1 to 2.4 provide background information on the composite material, identify significance of the zirconia bearing composites and specify the projected material with a discussion of relative advantages and disadvantages of the highlighted synthesis processes. The structural evolution of alumina, transition sequence of Al-hydroxide, crystal structure evolution of zirconia, classification, and the effect of stabilizer on zirconia are reported in Section 2.5. The toughening mechanism of zirconia toughened composite is discussed in Section 2.6. Section 2.7 and 2.8 discusses the physical properties of alumina, zirconia and ZTA and several applications of zirconia bearing composite materials, while Section 2.9 reviews the synthesis and properties of zirconia based ceramics.

This chapter incorporates background information to assist in understanding the aims and results of this investigation, and also reviews recent reports by other investigators with which these results can be compared. The review finds unresolved questions in the literature that can't be answered by a single research work.

2.1. Idea behind composite materials

The history of composite materials has developed from humble beginnings such as pre-historic mud bricks reinforced with straw etc., to a major topic of present-day Materials Science. Modern applications of composite materials include aerospace, sporting goods, automotives, military equipments, cutting tools, communication devices, prosthetics, refractories and building infrastructures, to name a few. Recent research and theories are able to analyze the behavior of both particulate and fibrous reinforced composites.

In general, composite materials (or composites for short) are engineered materials made from two or more constituent materials that remain separate and distinct on a macroscopic level while forming a single component. There are two categories of constituent materials: matrix and reinforcement. At least one portion (fraction) of each type is required. The matrix material surrounds and supports the reinforcement materials by maintaining their relative positions. The reinforcements impart special physical properties (mechanical and

electrical) to enhance the matrix properties. For example, the mechanical properties of a ceramic material can be enhanced through incorporation of zirconia particulate, which is governed by the transformation toughening and microcrack toughening mechanisms[5]. A synergism produces material properties unavailable from naturally occurring materials. Due to availability of the wide variety of matrix and reinforcement materials, the design potential is incredible.

Engineered ceramic composite materials must be formed to shape that involves strategically placing the reinforcements while manipulating the matrix properties to achieve a melding event at or near the beginning of the component life cycle. A variety of fabrication methods are used according to the end item design requirements. These methods are commonly named molding or casting processes, as appropriate and both the processes have numerous variations. The principal factors impacting the methodology are the natures of the matrix and reinforcement materials. Along with the composition of materials, another important factor is the production of gross quantity. The production of large quantities can be used to justify high capital expenditures for rapid and automated manufacturing technology. Small production quantities are accommodated with lower capital expenditures but higher labor costs at a correspondingly slower rate.

2.2. Significance of Zirconia Bearing Composites

One of the major characteristics, and the greatest disadvantage, of ceramics is their brittleness. There are only a few concepts available to compensate for this disadvantage and to improve the strength. Following Griffith's approach, the fracture strength of brittle materials can only be improved by an increase in fracture toughness or by a reduction in critical flaw size[6]. Therefore, much effort has been invested in sophisticated processing technology to reduce the size and density of processing flaws. However, the design of tougher flaw-tolerant ceramics is more accepted approach for wider industrial applications since it improves the reliability of a component. The fracture toughness can be increased by incorporating various energy-dissipating components into the ceramic microstructure. The synthesis of composite components can be adapted by incorporating inclusions such as whiskers, platelets or particles. The reinforcements serve to deflect the crack or to provide bridging elements hindering further opening of the crack. Another concept is to incorporate metallic ligaments into the ceramic matrix to form crack bridging elements that absorb energy by plastic deformation[7]. Finally, much benefit has resulted from incorporating a second phase which

undergoes a phase transition in conjunction with a volume expansion and associated with phase transformation that is initiated by the stress field of a propagating crack and can be applied as closing force on the crack. Therefore, the benefit of 'transformation toughening' and the composite materials have opened up the prospect of a host of new materials which have mechanical properties that can match the characteristics of metals, in addition to the advantages of ceramic materials.

Composites, where more than one phase is present, can have the opportunity of developing tailor-made properties with different materials having different intrinsic properties. 'Transformation toughening' is defined as a mechanism through which phase transformation decreases the driving force that is acting to propagate the crack. The crack can be pre-existing or formed under stress. The mechanism can be stress induced phase transformation, microcracking or compressive surface layer due to phase transformation. Toughened ceramics is the advance group of materials generating a lot of interest among researchers to utilize ZrO_2 in various ways. The brittleness of conventional ceramic materials is overcome through transformation toughening, compaction and composite matrix formation.

Zirconia toughening of ceramics, defined here in a rather broad sense: "Toughening", encompasses all types of mechanical property enhancements that can be achieved by utilizing either the tetragonal-to-monoclinic phase transformation of ZrO_2 particles dispersed in a ceramic matrix or other effects not directly associated with the transformation. Zirconia ceramics are distinguished based on the characteristic microstructural features and can be grouped as (a) Partially Stabilized ZrO_2 ceramics (PSZ) (b) Tetragonal Zirconia Polycrystals (TZP), and (c) Zirconia Toughened Ceramics (ZTC)[8]. Microstructural design criteria are presented based on experimental fabrications and results, together with prospects for future development. A detail study of different synthesis method of zirconia bearing composite and their properties are discussed in Section 2.7 to 2.8.

2.3. Why Zirconia Dispersed Alumina?

It has been observed from previous discussion that there is only one material, zirconia (ZrO_2) which has been utilized for transformation toughening till now to synthesize several composites like ZrO_2-TiB_2, WC-ZrO_2, Al_2O_3-ZrO_2, Mullite-ZrO_2, Si_3N_4-ZrO_2, Intermetallic (Fe-Al)-ZrO_2[9-12] etc. Among these, Zirconia Toughened Alumina (ZTA) ceramics have received significant scientific and technological attention during the last two decades for use

in cutting tools, dye or prosthesis components because of their excellent room temperature strength, toughness and wear resistance. These materials have following properties:

1. Lower density
2. A superior combination of high strength (from ZrO_2) and high hardness (from Al_2O_3)
3. Relatively low density; no open porosity
4. Very hard surface with good abrasion and wear resistance
5. Good flexural strength and fracture toughness
6. Excellent thermal properties and high temperature stability
7. Extreme corrosion resistance, nearly chemically inert
8. Electrically insulating behavior
9. Bio-compatibility
10. Typical applications in soldering processes, handling of components during thermal and chemical processes

However, the chemical composition, phase assemblage and their distribution as well as grain sizes of matrix and inclusion phase determine their end properties and service performance.

Zirconia dispersed toughened alumina have attracted special attention due to their excellent thermal and mechanical properties. The material has to be impervious to gases, and furthermore, mechanical strength and toughness must be sufficiently high to prevent breakdown of the device during use at elevated temperatures.

A small grain size of powder and/or sintered ZTA specimen can be very helpful for several other reasons. First, small grain size is favorable for obtaining superplastic deformation. The deformation rate is proportional to the inverse or the inverse square of the grain diameter, depending on the kind of deformation mechanism. Decreasing grain size to the nanoscale can also drastically increase both the deformation rate and total strain during hot-forging operation. Secondly, densification of zirconia dispersed alumina ceramics at relatively low temperatures is only possible when a very homogenous microstructure, i.e., highly uniform packing of the finest nonagglomerated powder, is present in the green compact[13]. Minimization of agglomeration is the subject of many researchers to attain low-temperature sintered bodies with a uniform nanograined microstructure[14,15].

To meet these requirements, several powder processing, forming and sintering processes were investigated. For powder synthesis, methods including attrition milling, CVD synthesis, spray-ICP, colloidal processing, hydrothermal reaction, evaporative decomposition,

hydrolysis coating, polymer/powder flocculation, plasma synthesis, sol-gel processing, and coprecipitated process were used[16-19]. However, a good control of the interacting liquid precursors (energy saving, less pollution, high homogeneity, and control of the final sintered product's morphology) can also be achieved through one of the pioneer sol-gel route.

On the basis of above advantages of Zirconia Toughened Alumina (ZTA), it is considered to go for a composite system with zirconia as particulate and alumina as matrix phase; where the precursor powder would be synthesized through sol-gel route. Refinement of zirconia particle in alumina matrix would enhance the toughening mechanism and governs the thermal and mechanical properties. Although extensive investigations have been made over the last half century, zirconia dispersed alumina still remains an interesting subject for ceramic researchers because of its great industrial and scientific potential. The advantages and disadvantages of highlighted sol-gel method are discussed in the next section.

2.4. Why sol-gel method?

An inhomogeneous mixing in terms of particle spacing and non-uniform ceramic microstructure cannot be avoided in the conventional powder mixing approach using P/M method. Hence, an alternative like sol-gel process can overcome this shortcoming. The level of mixing in the sol-gel process is in molecular range, which is never possible in solid state mixing. Hence, sol-gel mixing helps to evolve homogenous microstructure, most desirable criteria for compiling a composite. The crystalline temperature of obtained oxide materials is also lower than the conventional approach. Reduction of particle size of the individual ingredients is obviously at the highest level, which will be helpful in enhancing the sintering process without any additive. In order to retain tetragonal zirconia particles, the role of grain size is the most important factor that can be controlled only with this type of reactive particles.

According to Brinker [20] some advantages of the sol-gel method can be summarized as follows;

1. Better homogeneity – from raw materials
2. Lower temperature of preparation
3. Better purity – from raw materials
    - save energy
    - minimize evaporation losses
    - minimize air pollution
    - avoid reaction with container and so ensure purity

- by-pass phase separation
- by-pass crystallization

4. New non-crystalline solids
5. New crystalline phases from new non-crystalline solids
6. Better glass products determined by special properties of gel
7. Special products such as films

The most promising advantage of the sol-gel method is the possibility to prepare solids with pre-determined structure by varying the experimental conditions. For example, solutions containing a large amount of water and/or catalyzed ammonia lead to non-linear or network colloidal polymers in hydrolysis-polycondensation process. These polymers could be converted to bulk gels or powders. The solution with small water content lead to linear polymers when catalyzed by HCl. Fiber could be easily drawn from such solution immediately before gelation or films could be deposited. So, materials in different tailor made shapes as films, fibers and powders could be obtained.

Along with the advantages mentioned above the sol-gel method does have a few shortcomings.

1. High cost of raw materials
2. High shrinkage during processing
3. Residual fine pores
4. Residual hydroxyl groups
5. Health hazards
6. Long processing time

2.5. Origin, Crystal Structure and Classification of Al_2O_3 and ZrO_2

2.5.1. Alumina (Al_2O_3)

2.5.1.A. Origin and Crystal Structure of α-Alumina

Scientific investigations on alumina date back to the last century. The first knowledge of application however, goes back to 1907, when a patent describing the production of a high alumina ceramic material was applied for[21]. Alumina can be considered as a typical representative in the group of structural ceramics. These materials are intended particularly to serve as structural parts subjected to mechanical loads, in many cases at high temperatures. Thus, the common feature of structural ceramics is good mechanical behavior and, therefore,

efforts in developing, fabricating, and optimizing these materials are concentrated towards high strength. In many cases, the development of high-strength ceramics is carried out with the objective of substituting metallic materials. The other examples of structural ceramics, in addition to alumina, are some pure oxide ceramics such as yttria (Y_2O_3), titania (TiO_2), zirconia (ZrO_2), magnesia (MgO); and alumina-magnesia spinel ($MgAl_2O_4$), as well as the two non-oxide ceramics which are extensively used in gas turbine applications, silicon nitride (Si_3N_4) and silicon carbide (SiC)[22-23].

The extensive historic development of the discovery and research of the individual crystallographic phases of alumina has been traced by Gitzen[24] in his ample work on aluminum oxide ceramic technology. He has reported the presence of seven crystallographic phases of calcined, water free alumina had been found. Structural applications of aluminum oxide, however, are limited almost entirely to the α–phase (α-Al_2O_3), also called corundum or, in its single-crystalline form, sapphire. After Gitzen, the first approximate determination of the crystallographic structure of corundum dates back to the work of Brag and Brag in 1915; and the first exact attribution to the rhombohedral structure ("corundum structure") was made by Pauling and Hendricks in 1925. Further crystallographic studies were carried out by Winchell[25] and proposed a numerical procedure and particular stereographic projection map of corundum for the determination of the orientation of principal crystallographic planes and directions from Laue back-reflection patterns. A very detailed description of the crystallography of sapphire single crystals was given by Kronberg[26].

The structure of aluminum oxide consists of close packed planes of the large oxygen ions stacked in the sequence A-B-A-B, thus forming a hexagonal close packed array of anions. The cations are placed on the octahedral sites of this basic array and form another type of close packed planes which are inserted between the oxygen layers. To maintain charge neutrality, however, only two thirds of the octahedral sites available are filled with cations. Fig. 2.1a illustrates the packing of Al and O in the basal plane. Since the vacant octahedral sites also form a regular hexagonal array, three different types of cation layers can be defined, depending on the position of the vacant cation site within layer, which may be named as a, b and c, and which are stacked in the sequence a-b-c-a-b-c. This gives the complete stacking sequence of anion and cation layers of the form A-a-B-b-A-c-B-a-A-b-B-c-A. It is only reproduced after the sixth oxygen layer or after the sequence a-b-c is repeated twice (Fig. 2.1b). The unit cell of α-alumina defined in this way is called the crystallographic or structural unit cell, in contrast to the morphological unit cell, where the cation sequence is

repeated only once and the height is half that of the structural cell. This important difference between the two cells, which has given rise to some confusion in the literature dealing with crystallographic indices of sapphire, was pointed out clearly by Kronberg. The structure of α-Al_2O_3 results in coordination number of 6 and 4 for the cation and the anion, respectively. The ionic radii for this coordination are 0.053nm for Al^{3+} and 0.138nm for O^{2-}. Lattice parameters a_0 and c_0 are 4.7589 and 12.991Å respectively.

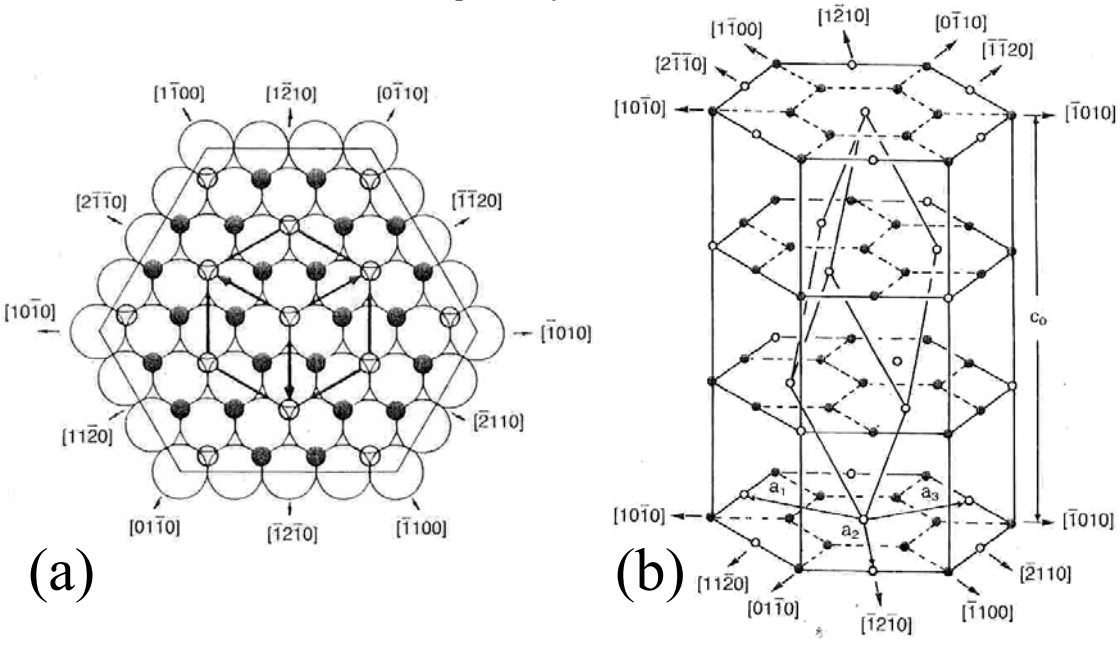

Fig.2.1. Basal plane of α-Al_2O_3 showing the hexagonal close packed anion sublattice (large open circles) and the cations occupying two-thirds of the octahedral interstices (small filled circles); small open circles are empty octahedral interstices (a).The cation sublattice in α-Al_2O_3 filled circles are Al, open circles are empty octahedral interstices (b)[29].

2.5.1.B. Sequence of Al-Hydroxide Transition

The synthesis of α-Al_2O_3 can be achieved by several methods. The aluminum hydroxide is produced from the alumina precursor powder, synthesized from inorganic or organic compound through chemical route and is sequentially transformed to produce α-alumina. The following sequence of transitions (shows graphically in Fig. 2.2), is mainly developed by Stumpf et. al and Tertian and Papée[27,28], are generally accepted, although there is different opinion about the X-ray identification of some phases and the existence of others. The sequences are affected not only by the starting materials but also by their coarseness of crystallinity, heating rates and impurities. The approximate temperature ranges of stability of the phases are included below:

Gibbsite Transitions

In vacuum, coarse or fine gibbsite transforms to rho (100 to 400°C), to eta (270 to 500°C), to theta (870 to 1150°C), to alpha (1150°C). Instantaneous dehydration at 800°C: gibbsite to eta, to theta, to alpha alumina. In air, fine gibbsite: gibbsite to chi (300 to 500°C), to kappa (800 to 1150°C), to alpha alumina. In air, coarse gibbsite: (1) gibbsite to chi, to kappa, to alpha alumina. (2) gibbsite to boehmite (60 to 300°C), to gamma (500 to 850°C), to delta (850 to 1050°C), to theta to alpha alumina.

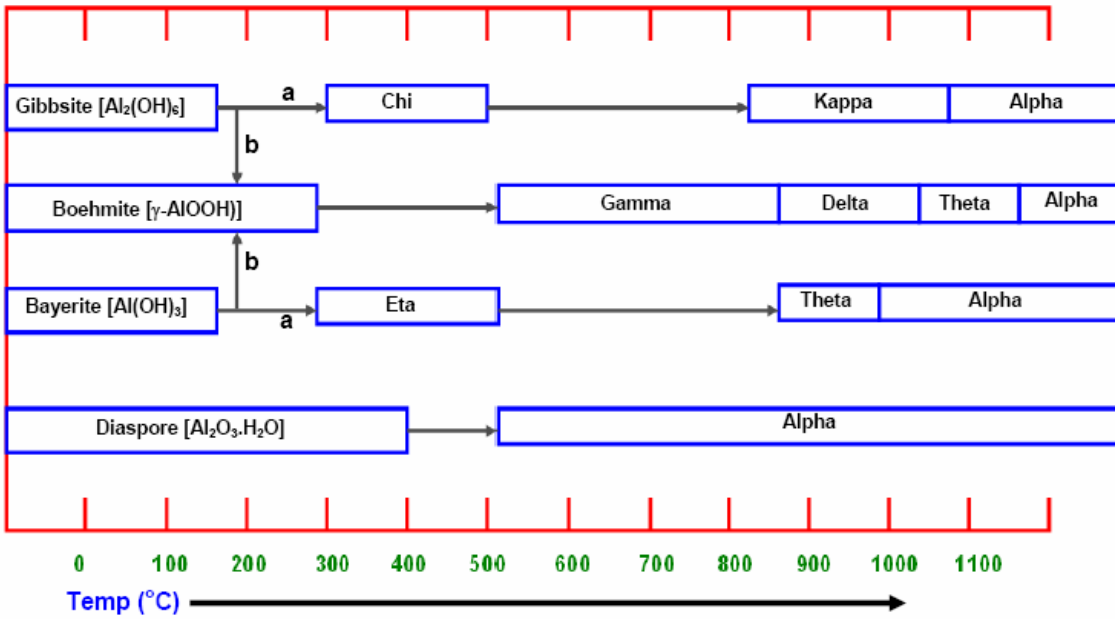

Fig.2.2. Dehydration sequence of Alumina hydrates in air. Enclosed area indicates range of stability. Open area indicates range of transition. Path 'b' is favored by moisture, alkalinity and relatively coarse particle size; path 'a' by fine crystal size. However, the sequences may be affected by starting materials, heating rates and incorporation of second phase.

Bayerite Transitions

The bayerite transitions are substantially similar to the gibbsite transitions except that fine bayerite in air transforms as follows: bayerite to eta (250 to 500°C), to thea (850 to 1150°C) to alpha alumina. The difference between bayerite and gibbsite transitions is the substitution of eta for chi alumina and the absence of kappa alumina in the bayerite transition.

Boehmite Transition

Fine boehmite (pseudoboehmite, 350 m^2/g): boehmite to bayrite, to eta (100 to 350°C), to theta, to alpha alumina. Coarse hydrothermal boehmite (less than 15m^2/g) prepared from

gelatinuous aluminum hydroxide, gibbsite, bayerite, or higher transition phases by digestion in H_2O at above 150^oC: boehmite to gamma (360 to 860^oC), to delta, to theta, to a-Al_2O_3.

Diaspore Transitions

Deflandre, in 1932, showed that diaspore transformed to corundum by an ordered process, without intermediate products, at about 450 to 600^oC. Herold and Dodd observed that diaspore clay formed corundum and gamma alumina at 400^oC. However between 400 and 750^oC, there was a gradual expansion in the size of the corundum unit cell, as determined by X-ray. Upon continued heat treatment at higher temperatures, the unit cell gradually reduces to the true dimensions.

A few instances of factors affecting either the temperature of transition or the sequence of phases have already been cited. Some of theses factors are: the starting material, particle size, the extent of disorder or activity, gases in the calcining atmosphere, impurities, and additives that either promote or suppress crystal growth or affect other properties. In general, the factors discussed here are those which affect loose powder transitions.

2.5.1.C. Improvement of Mechanical Properties of Al_2O_3

Aluminum oxide stands out due to it's favorable properties such as high hardness, and hence, high wear resistance and a low friction coefficient, high resistance to corrosion by practically all chemical reagents, a very high resistance to high temperature corrosion in air, thermodynamic stability, i.e., the absence of phase transformations within the entire temperature range of solid state, and the fact that the material retains its strength even at very high temperatures (≈ 1500-1700^0C). Its other properties include: its low strength as compared with the theoretical strength and with the strength of metallic alloys, the large statistical spread of its strength values, its great brittleness, i.e., the complete absence of plastic deformation until about 1200^oC, its low toughness and, hence, large susceptibility to thermal and mechanical shock loading, and the phenomenon of time-dependent strength. Due to these detrimental properties, the usage of Al_2O_3 (aluminum oxide) in engineering allocations, like that of many other structural ceramics, is still limited. To overcome this lacuna, many efforts have been made to increase the strength of ceramic materials like alumina. The strength of ceramics, σ, can be expressed as;

$$\sigma = K_{IC}/(YC^{1/2}) \quad \text{……..2.1}$$

where, K_{IC} is the fracture toughness, C is the flaw size, and Y is a geometrical factor of about 2. Equation 2.1 demonstrates that attempts to improve the strength of a ceramic effectively must aim at increasing either K_{IC} or decreasing C. Consequently, the effect of strengthening mechanisms discussed in the following sections either consists of increasing K_{IC}, as is the case for strengthening by second phases or by several mechanisms. However, the fracture toughness and strength of alumina can be tailor made with incorporation of toughened phase, like zirconia.

The basic idea of strengthening ceramics by a second phase is to impede the movement of dislocations, as in metals. Models have been presented by Lange[29] and by Evans[30] that permit the assessment of the increase in fracture energy or fracture toughness depending on the size, shape and concentration of second phase particles. The strengthening effect is thought to be due to the bowing of the crack line between two pinning obstacles. Since the crack front can be treated as having a line energy per unit length, crack front bowing means consumption of additional energy, which must be supplied by the elastic stress field ahead of the crack front, thereby leading to an increased value of the fracture energy at the moment of breakaway.

2.5.2. Zirconia (ZrO_2)

ZrO_2 was discovered in Brazil as the naturally occurring mineral, baddeleyite, by Hussak in 1892. This rich mineral usually contains about 80% ZrO_2, but it can be high as 90%. The major impurities in this mineral are usually TiO_2, SiO_2, Fe_2O_3 etc. The other main source of ZrO_2 is zircon ($ZrSiO_4$), which occurs as secondary deposits in India, Australia and U.S. ZrO_2 is not a rare substance and represents about 0.02 to 0.03% of the Earth's crust[31].

2.5.2.A. Crystal Structures and Transformation Characteristics

Pure undoped zirconia exhibits the following phase transformations:

$$monoclinic(m-ZrO_2) \underset{950^{\circ}C}{\overset{1170^{\circ}C}{\leftrightarrow}} tetragonal(t-ZrO_2) \xrightarrow{2370^{\circ}C} cubic(c-ZrO_2) \xrightarrow{2680^{\circ}C} liquid$$

The crystal structures of the three zirconia phases are shown in Fig. 2.3. The cubic zirconia has the ideal fluorite structure, whereas the other polymorphs (tetragonal and monoclinic) have distorted fluorite structure[32].

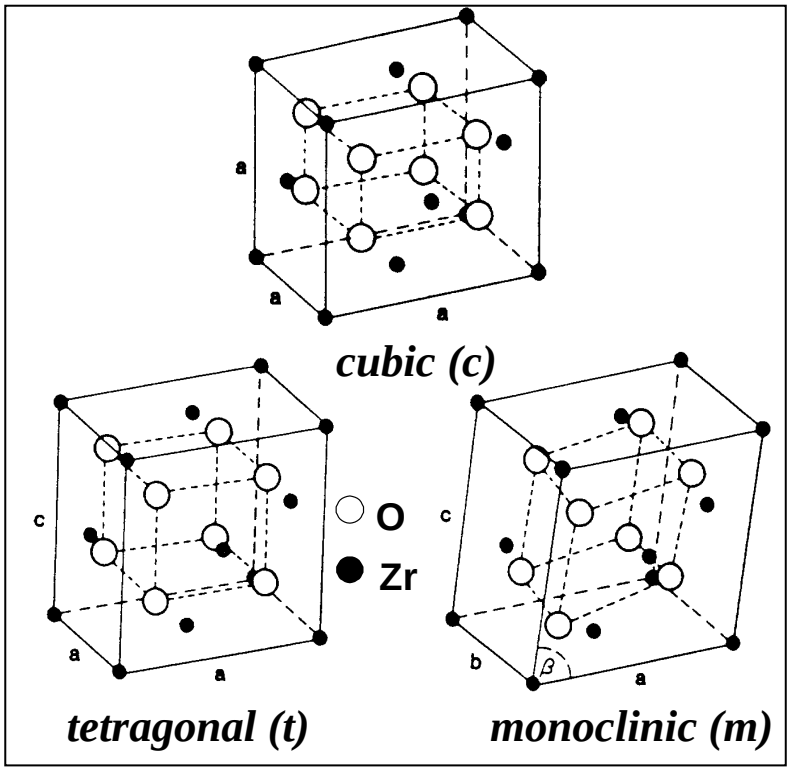

Fig.2.3. Crystal structures of the three most important zirconia polymorphic phases: cubic (c-ZrO_2), tetragonal (t-ZrO_2) and monoclinic (m-ZrO_2)[32].

The transformations between the different polymorphs are important as far as the processing and mechanical properties (strength, toughness, etc.) of zirconia ceramics are concerned. It has been well documented in the literature[1,2,5] that the t→m transformation in pure undoped zirconia during cooling is a reversible thermal martensitic transformation, associated with a large temperature hysteresis (around 200°C), a finite amount of volume change (4-5%), and a large shear strain (14-15%). The transformation leads to crumbling of the sintered part made from pure zirconia. Several dopants such as yttria, ceria, magnesia, calcia, etc. are added to stabilize the high temperature tetragonal and/or cubic phase in the sintered microstructure. The reported lattice parameters of the t-ZrO_2 at room temperature are 0.5102 nm (a-axis) and 0.5176 nm (c-axis) for 3mol % yttria stabilized zirconia.

The martensitic transformation of tetragonal zirconia (t-ZrO_2) to monoclinic (m-ZrO_2) can be induced either during thermal cooling or by external loading under isothermal conditions[4]. Both the transformation routes have their importance with respect to the technological applications of zirconia containing ceramics. While thermally induced transformation will dictate the amount of tetragonal phase that can be retained after thermal

cycling, the stress induced martensitic transformation of metastable t-ZrO_2 to m-ZrO_2 in the stress field around a propagating crack enhances the toughness of zirconia ceramics. The latter phenomenon is known as transformation toughening.

The review of classical theory of martensitic transformation suggests that three steps are essential for the formation of a martensite plate: a) nucleation of martensite from austenite; b) the lattice invariant deformation which produces an interface with no average distortion between the phases c) the deformation accommodating the shape strain of the martensite plate. While all these steps are involved in zirconia phase transformation (being martensitic in nature), the overall t→m ZrO_2 transformation process takes place in two major stages[8]. In the first stage, the transition of the lattice structure from tetragonal to monoclinic occurs by shearing displacement of zirconium ions. The second stage involves the diffusional migration of oxygen ions to their proper positions in the monoclinic symmetry. The displacement of the oxygen ions from the ideal fluorite positions along the c-axis is recently investigated by XRD[33]. It was hypothesized that, the rapid shear displacement of the zirconium ions is the rate-controlling factor for nucleation and longitudinal growth of the monoclinic plates and the diffusional migration of the oxygen ions controls the lateral growth of the plates. Furthermore, it is noted that the reverse m-t transformation is a diffusion-controlled process. The reverse transition of the lattice structure from 'm' to 't' symmetry and the migration of the Zr^{4+} and O^{2-} ions to their respective positions are controlled by the diffusional displacement of the respective ions [34].

Although c- ZrO_2, t- ZrO_2 and m- ZrO_2 are most commonly observed phases, the other zirconia phases, e.g. non-transformable tetragonal (t′-ZrO_2), rhombohedral (r-ZrO_2) etc. are found to exist under certain conditions[35]. It has become customary to refer to the tetragonal zirconia phase formed from the cubic phase by a diffusionless, displacive transformation as the t′-ZrO_2[36]. It is crystallographically the same as the transformable t-phase; the difference lies in the stabilizer content and the morphology. The t′-ZrO_2 generally can accommodate higher yttria content than the equilibrium t-ZrO_2, which is transformable. The transformable t-ZrO_2 grains are monodomain, whereas the non-transformable t-ZrO_2 phase consists of three variants or domain orientations. The extreme stability of the t′-ZrO_2 phase is largely related to both the higher amount of stabilizer and the microstructural feature like finer domain size (≈ 0.1μm). The t-ZrO_2 is not reported to undergo stress induced phase transformation; instead, the toughening of the ceramic materials containing t′-ZrO_2 is commonly attributed to the ferroelastic domain switching; and the same will be discussed in a subsequent section. XRD

experiments on the as machined, abraded and polished zirconia surfaces have recorded the existence of the r-ZrO_2 phase[37]. Mitra et al. suggested that the shear stresses as induced during cutting, for example, often favor the t→r transformation[37]. Burke et al. presented the experimental and microstructural evidence of the fact that r-ZrO_2 phase formed in an intermediate stage of the t-m transformation and that once formed could act as barrier to further transformation of the tetragonal phase[38]. More details of the crystal structure and the crystallographic data of all the zirconia phases can also be found in recent articles[35].

2.5.2.B. Classification and stabilization in zirconia based ceramics

ZrO_2 ceramics can be broadly classified into three important categories: a) TZP (tetragonal zirconia polycrystals), b) PSZ (partially stabilized zirconia), and c) ZTC (zirconia toughened ceramics). The representative microstructures of these three classes of materials are illustrated in Fig. 2.4. The detailed description of the different classes of zirconia ceramics can be found elsewhere.

TZP is a material with nearly 100% tetragonal ZrO_2 phase stabilized by yttria or ceria additions (Fig. 2.4a). Typical grain size of the tetragonal phase in TZPs is around 0.2-1 μm. The addition of stabilizers reduces the driving force for the transformation of the metastable t-ZrO_2 to the thermodynamically stable m-ZrO_2 and, as a result, the tetragonal phase is retained in the microstructure. The retention of t-ZrO_2 is analogous to the quenching of steel to stabilize the austenite phase at RT. Typical applications of TZP ceramics include wear resistant components in machinery, femoral ball heads, pump housing for aggressive chemicals, milling balls, etc. TZP ceramics are often prefixed with Ce- or CeO_2- to denote ceria-stabilized, or with Y- or Y_2O_3- to denote yttria-stabilized, and a number in front of the acronym generally denotes the mole percent of dopant. For example, 3Y-TZP represents a 3-mol% yttria-stabilized zirconia ceramics. Two most popular TZP materials are Y-TZP and Ce-TZP, stabilized by yttria and ceria; respectively.

Compared to TZP, PSZ has a coarse grained microstructure with the t-ZrO_2 precipitates embedded in c-ZrO_2 grains. By heat treating and/or annealing in the two-phase (c+t) field at high temperature around 1600°C, small lenticular shaped tetragonal phase is precipitated in cubic zirconia matrix (see Fig. 2.4b). PSZ is mostly used as wear resistant components in machineries. Similar nomenclature, as used for TZP, is also used to denote PSZ materials. Most of the commercially available PSZ ceramics are stabilized with MgO and CaO, and denoted as Mg-PSZ and Ca-PSZ respectively.

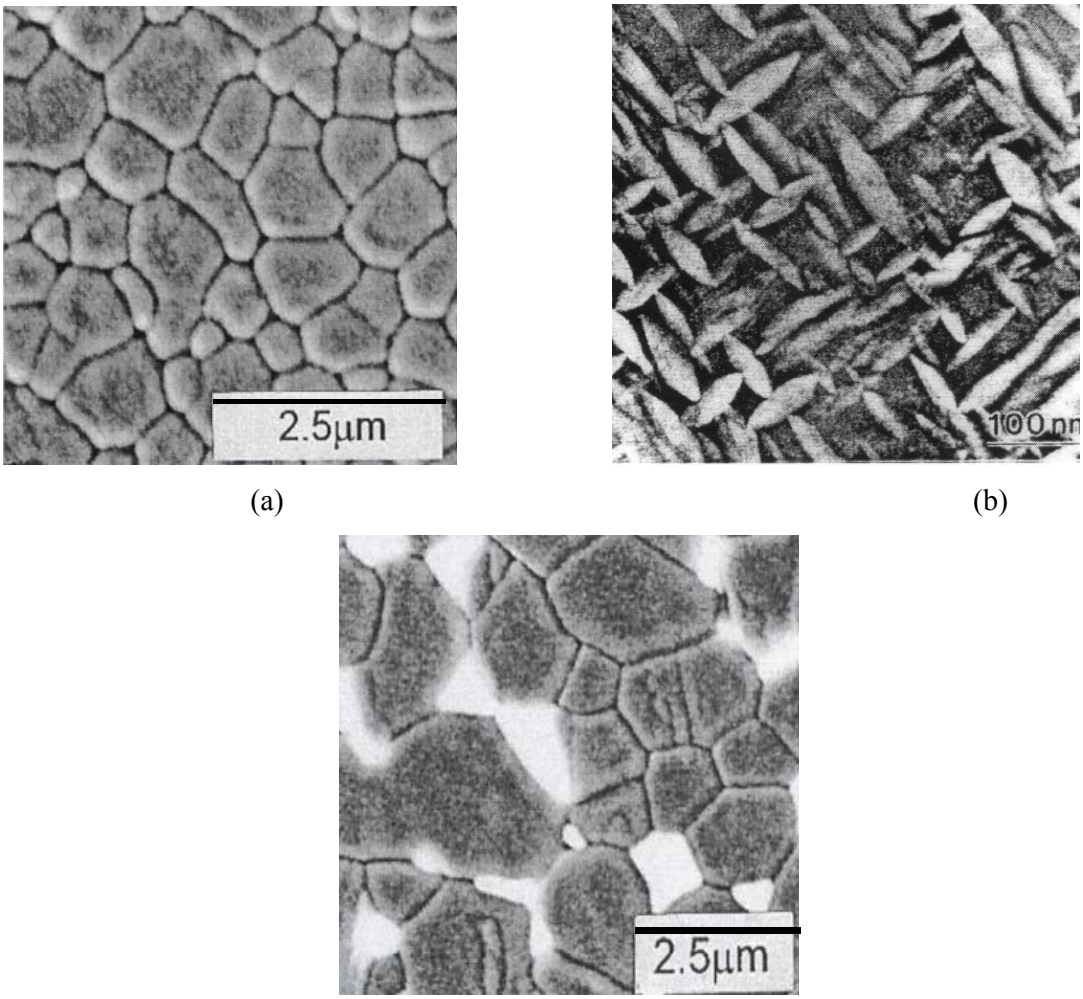

(a) (b)

(c)

Fig.2.4. Representative microstructures showing the distribution and morphology of tetragonal zirconia phase: polygonal equiaxed tetragonal grains in a 2.5Y-TZP (a), lenticular shaped tetragonal zirconia precipitates in a cubic matrix of a Mg-PSZ ceramic (b) and the intergranular zirconia grains (bright phase) in an alumina matrix (dark contrast) in ZrO_2-toughened Al_2O_3 ceramics (ZTA)[35].

The microstructure of ZTC consists of a ceramic matrix containing dispersed particles of zirconia. The difference in the coefficient of thermal expansion (CTE) between the matrix and the dispersed phases causes residual stresses, which control the stability of the zirconia particles during cooling from the sintering temperature. The mechanical properties, in particular toughness of ZTCs, depend on the transformability of the retained t- ZrO_2 phase. The increase in toughness results from the stress induced transformation of the dispersed tetragonal zirconia phase. When m-ZrO_2 is present in the microstructure, toughening via microcracking becomes operative. Among the ZTCs, the widely investigated material system

is zirconia toughened alumina (ZTA) with zirconia content of around 10-30vol%. Typically, ZTA has transverse bend strength between 500-1300 MPa and fracture toughness between 5-10MPa $m^{1/2}$. ZTC has found major applications as cutting tools, precision rollers and conveyer chains in heat treating furnaces, etc. A representative microstructure of ZTA containing 15vol.% stabilized tetragonal zirconia phase is shown in the Fig. 2.4c.

2.6. Transformation Toughening

In their seminal article 'ceramic Steel', Garvie, Hannink and Pascoe[39] were the first to realize the potential of zirconia for increasing both the strength and toughness of ceramics by utilizing the tetragonal → monoclinic phase transformation of metastable tetragonal particles induced by the presence of stress field ahead of crack. The volume change and the shear strain developed in the martensitic reaction were recognized to resist the opening of the crack and therefore acting to increase the resistance of the ceramic to crack propagation.

A great deal of intellectual energy has been expended in attempts to devise theories and to develop mathematical frameworks to explain the phenomenon. Several thorough reviews are available on this topic. The practical aspects and phenomena of transformation toughening have been reviewed with admirable clarity[4].

It is generally recognized that, apart from crack deflection which can occur in ZTA ceramics, the t → m transformation can develop significantly improved properties via two different mechanisms: Microcracking and Stress Induced Transformation Toughening. Transformation toughening is induced from the stress-induced transformation experienced by tetragonal zirconia particles when interacting with an advancing crack[29-30]. The effect of microcracks intrinsically related to such transformation, which then promote a toughening effect through the permanent dilatation and reduced modulus that they imply around the crack-tip.

2.6.1. Microcracking

The toughening of ZTA by microcaking is concerned with m-ZrO_2 phase. When cooled through the transformation temperature ($T_{t\rightarrow m}$), the volume expansion of 3-5% occurring in the ZrO_2 particles causes a crack to form (Fig. 2.5 and 2.6). Tangential stresses are generated around the transformed particle that induces microcracks in the matrix. The cracks have the ability to extend in the stress field for propagating crack or to deflect the propagating crack which can absorb or dissipate the energy of the crack, thereby increasing

the 'toughness' of the ceramic. The optimum conditions are met when the particles are large enough to transform but small in size to cause limited microcrack development. The ZrO_2 particle size can usually be controlled by milling time prior to sintering or ageing conditions after sintering to develop the desired size.

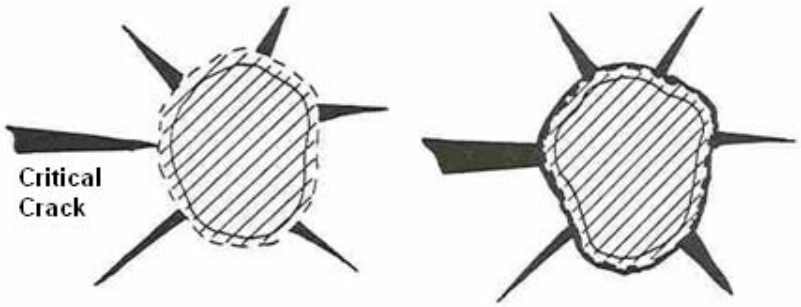

Fig.2.5. The martensitic transformation that occurs in ZrO_2 (tetragonal to monoclinic at 900-1100°C) with its 3-5% volume expansion, develops microcracks around the ZrO_2 particles (a). A crack propagating into the particle is deviated and becomes bifurcated (b), thus increasing the measured fracture resistance[30].

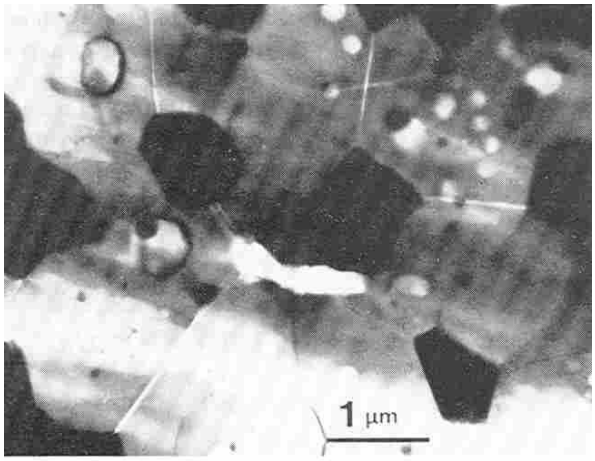

Fig.2.6. TEM of Al_2O_3-ZrO_2 showing the zirconia particles at the dark phase. The dimensions of the particles are such that they supercritical and transform when constraint is removed during the thinning process. The transformation develops high strains in the Al_2O_3 matrix which can only be accommodated by microcracking[30].

In order to obtain maximum toughness, the volume fraction of ZrO_2 inclusions must be at an optimum level[40]. It is observed that the toughness reaches to a maximum above which microcracks generated by the ZrO_2 particles will interact with one another, resulting in a decrease in strength.

2.6.2. Stress Induced Transformation Toughening

On cooling ZrO_2 from higher than 1200^oC to room temperature, the tetragonal → monoclinic transformation should occur. If, ZrO_2 is finely divided or constraining pressure is exerted on it by the matrix, the zirconia particles can retain their metastable tetragonal form. The particles can be introduced as a second phase during the initial fabrication, for example, zirconia in alumina or may be developed as a second phase by heat treatment, during or after sintering.The mechanism of toughening is considered to be a stress induced transformation of the metastable tetragonal particles to the monoclinic form. If a crack is allowed to extend under stress (Fig. 2.7), large tensile stresses are generated around the crack, especially ahead of the crack tip[41]. These stresses release the matrix constraint on the tetragonal zirconia particles and if sufficiently large, could result in a net tensile stress on the particle, which under the new conditions will transform to monoclinic symmetry. The volume expansion and shear strain developed in the particle cause the martensitic reaction resulting a compressive strain generated in the matrix. Since the strain occurs in the vicinity of the crack; extra work would be required to move the crack through the ceramic, accounting for the increase in toughness and strength.

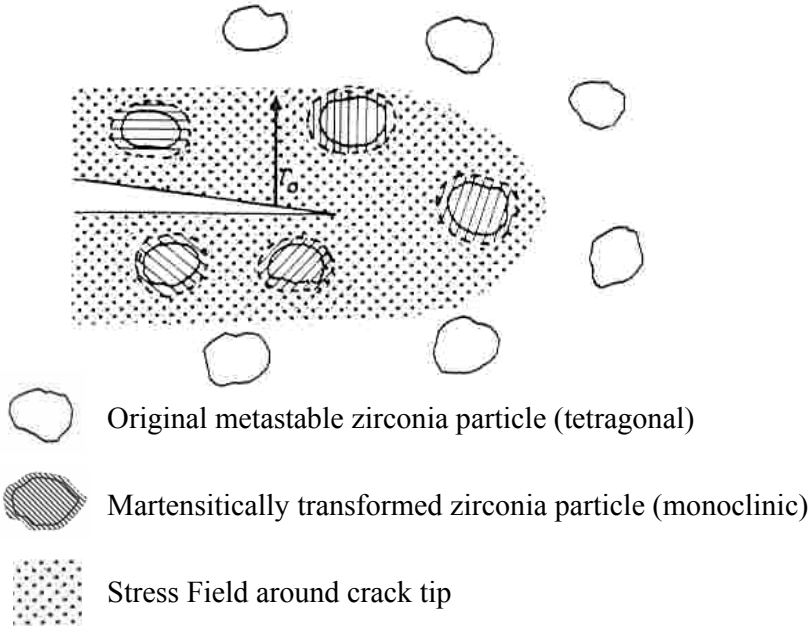

Fig.2.7. Stress induced transformation of metastable ZrO_2 particles in the elastic stress field of a crack[30].

A critical particle size range exists in zirconia within which tetragonal particles can be transformed by stress. If the particles are less than the critical size they will transform spontaneously. This critical size limit depends on the matrix constraint and the composition of

the system. The chemical free energy associated with the phase transformation decreases with the increasing amount of stabilizing oxides. Therefore, larger particles can be induced to remain in the metastable tetragonal form.

2.6.3. Compressive Surface Layers

The compressive surface layer developed in zirconia based transformation toughened ceramics is a well-known phenomenon[42,43]. Such stress develops as a result of spontaneous t-m transformation of zirconia particles in or near the surface, due to absence of the hydrostatic constraint near the free surface. The process is shown in the diagram (Fig. 2.8).

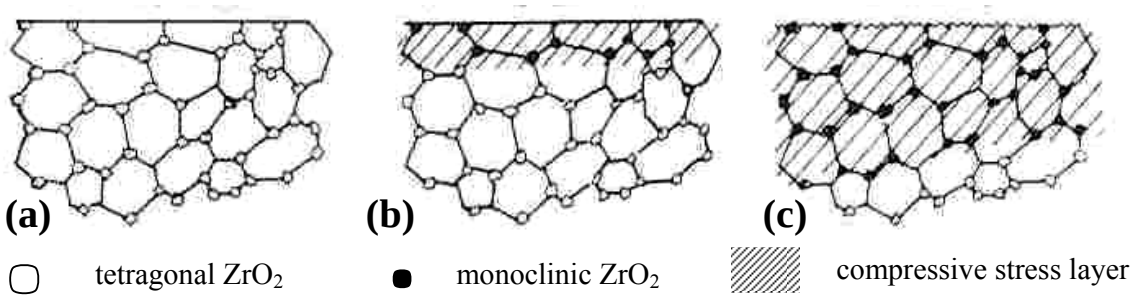

Fig.2.8. Diagram of a section through a free surface at (a) the sintering temperature. On cooling, particles of ZrO_2 near the surface (b) transform due to reduced constraint, developing a compressive stress in the matrix. The thickness of this compressively stressed layer can be increased. (c) by abrasion of machining[30].

A considerable increase in the fracture strength of the ceramic can be obtained; up to double the value for the fracture strength of the matrix is almost common. Surface grinding has been found to be the most effective method of inducing the metastable tetragonal particles to transform, because the compressive stress can be generated at some depth (10-100μm) below the abraded surface. The strengthening effect is known to be dependent on the severity of the grinding. However, it has also been shown that the amount of monoclinic phase present in the ground surface decreases rapidly when the surface is carefully polished away in steps[44]. It is also established that the maximum benefit can be realized if the thickness of transformed zone, i.e. the thickness of compressively stressed layer, is larger than the critical flaw size, but small enough in comparison with the cross section of the article.

The development of a compressive surface layer in the ceramic when it is abraded- or scratched is perhaps the most significant phenomenon associated with transformation toughened ceramics. For the first time, engineers have a material which is less sensitive to small surface defects, which may be introduced during handling. Any small abrasion, which is

less than the critical flaw size, introduced into the surface is immediately placed into compression that effectively removes the abrasion flaw from its possible role as a critical flaw. Since the maximum load is usually placed on the outer surface of a ceramic component, usually as a result of a bending stress due to alignment problems, it is the population of surface flaws which is most likely to provide the critical flaw. Hence, the importance of the compressive surface stresses is considerable.

2.6.4. Analysis of toughening Mechanisms

Two semi-quantitative approaches to the theory of toughening have been made. Lange[45] used a thermodynamic model whereas Evans[46] used a strain energy analysis to predict the strengthening and toughening behavior.

A generalized approach, based on the energy absorbed ahead of a crack movement, has been provided by Claussen and Rühle[47] on loading from zero to the propagation stress and the following equation has been proposed:

$$K_{IC} = K_o + \sqrt{2\,E\,\eta_T\,r_T} + \sqrt{2\,E\,\eta_m\,r_m}$$

Where, K_{IC} = Fracture toughness, K_o = Fracture toughness of the matrix, E = Elastic Modulus, η = Energy density absorbed ahead of a crack, r = Radius of the 'process zone', Subscript T = stress induced transformation mechanism, Subscript m = microcracking nucleation mechanism

Why detail review of Zirconia in Zirconia matrix and Zirconia in Alumina matrix is required?

The selected Al_2O_3-ZrO_2 composite material can be synthesized through incorporation of pure zirconia or PSZ in alumina matrix by several seminal methods. It has been noticed that after compaction and sintering of this composite, the zirconia particle may be dispersed and/or agglomerated within the alumina matrix as intra or inter-granular grain. While the properties of the zirconia particulate reinforced Al_2O_3-ZrO_2 composite is controlled by the content and distribution of zirconia phase. Hence, the process of synthesis and properties of zirconia in zirconia matrix are essential along with the projected zirconia in alumina matrix. A detailed literature review of both of these materials is discussed in the following section. Additionally, several applications[48-50] of both of these composites are discussed toward the end of this chapter.

2.7. Synthesis and Properties of Zirconia in Zirconia Matrix

Bansal et.al[51] studied the precipitation of a second phase in a PSZ material, where CaO and MgO were used as dopants. The microstructure of the furnace-cooled material was compared with the air-quenched material to room temperature and compared their microstructures. TEM study clearly showed the precipitation of monoclinic phase within the cubic grains. These intergranular precipitates are responsible for the change in thermal properties of the material. Wheat[52] studied the thermal shock resistance of the Ca-PSZ prepared by co-precipitation route followed by freeze-drying with an optimum amount of CaO (7-8mol%). The thermal shock properties of this material have been explained through micro-crack network. The microstructure of Ca-PSZ was studied by Green et al[53], where analysis was carried out for different heating cycles. There was little SiO_2 phase present as evidenced by the presence of liquid in microstructure. Nicholson et al[54] studied thermal shock characteristics of Ca-PSZ. They found that a fast cooled material had much lower monoclinic content than the slower one. Green et.al[55] studied the fracture toughness of Ca-PSZ and discussed the different techniques of measuring the same. Garvie et al[56] studied the microstructure and thermo-mechanical properties of Ca-PSZ; and microcracking responsible for higher thermal shock resistance. Garvie et al[57] considered the aged PSZ and CSZ materials and studied their fracture toughness. The observed tensile strength increased initially with ageing time but decreased subsequently. Gulati et.al[58] studied MgPSZ and (MgY)-PSZ for the study of fatigue characteristics. They[59] also studied the same material for their suitability as hot extrusion dye, where the intergranular as well as intragranular monoclinic precipitate showed the best thermal shock resistance. High percentage of monoclinic phase also helped in the same. Porter et al[60] heated up Mg-PSZ to cubic phase field and subsequently annealed at different temperatures from 850 to 1500^0C. Optimum mechanical properties were reported where materials were aged at above 1400^0C resulting in formation of coherent metastable tetragonal particles. Hannink[61] tried to determine the lattice parameters within the range of metastability for Mg-PSZ, Y-PSZ and Ca-PSZ. He claimed the parameters did not change significantly. Garvie et al[62] studied Ca-PSZ and Mg-PSZ material for dies and found that the Modulus of Rupture (MOR) strength dips to a minimum after 3 hours of ageing and then picks up. Gupta[63] studied Y-PSZ system and found that the sample with high percentage of retained tetragonal phases had grain sizes less than 0.3μm. During grinding the tetragonal samples were converted to monoclinic. Porter et al[2] used Mg-PSZ solution annealed at 1850^0C and then quenched to room temperature. The samples were aged at different temperatures,

where K_{Ic} value of 6 MPa.m$^{1/2}$ was the highest value after ageing at 1500^{0}C for one hour. Chen et al[64] tried to obtain Y-PSZ through different chemical routes. Pujari et al[65] used a sintering process which was a hybrid between hot pressing and hot isostatic pressing. Pressure was applied uniaxially through a transmitting medium like molten glass to form PSZ (3.5 mole%Y_2O_3). Heuer et al[66] studied the thermal shock resistance of Mg-PSZ, where thermal shock resistance was evaluated by their retained strength. TEM showed that the original sample had intergranular and transgranular fracture. With different level of Y_2O_3 doping, the maximum $K_{Ic} \approx$ 9.2MPa.m$^{1/2}$ value could be observed for monoclinic ZrO_2. Matsumoto[67] discussed the strength recovery in Y-TZP (100% tetragonal) material. At 230^{0}C, water vapor degraded the material but on subsequent heating the material recovered the strength. Hannink et al[68] studied Mg-PSZ material as wear resistant material for extrusion dyes. Lanteri et al[69] developed Y-PSZ with non- transformable tetragonal zirconia. Tsukuma[70] studied the mechanical and thermal properties of Y-PSZ from 2 to 6 mol% Y_2O_3 and observed that the grains more than 1μm were transformed from tetragonal to monoclinic during ageing. The grain size lower than 0.5μm remained unaffected even after 1500hrs. Another group of researchers[36] observed the microstructural evolution and ordering in commercial Mg-PSZ, heating them to different temperatures and soaking periods and also calculated the lattice parameters. Hannink et al[71] studied the Ca-PSZ (8.4 mole %), which was isothermally aged at 1300^{0}C for different time periods. Coarsening of the precipitate tetragonal phase initially improved the mechanical properties. Precipitates above a critical size had monoclinic structure. Ruhle et al[72] studied Y-TZP of eleven different varieties, where Y_2O_3 varied from 3-6 wt%. They reported that all eleven materials had an amorphous grain boundary phase. In the as-fired specimens, small microcracks were found near the grain boundaries. Matsushita et al[73] studied the strength of Y_2O_3 stabilized zirconia. Y-TZP had a maximum flexural strength which was more than twice that of Y-PSZ. Flexural strength reached a peak around 3 mol % Y_2O_3 and then reduced. Tsukuma et al[74] fabricated dense Y-TZP by pressureless sintering as well as hot isostatic pressing. Strength of Y-TZP was increased significantly by HIP. Green et al[53] fired 3.4wt% CaO in the cubic phase field and cooled at different time schedules. Slower cooling rates led to larger grains and higher monoclinic content. They also studied the fracture toughness of Ca-PSZ (3.4 wt %) by notching the samples with different depths. They reported that work of fracture had been sensitive to strain rate. Garvie et al[56,75] subjected 3.5wt % Ca-PSZ to quenching by air blast from a temperature of 700 to 1300^{0}C and MOR values were measured. Measurements show that the MOR progressively went down with the increase in

temperature difference. The measured values were compared with mullite and Ca-PSZ was found to be superior. Ca-PSZ was subjected to 1 min flame blast (1050^{o}C) and 1 min air blast cycle. After every cycle, modulus of elasticity was measured and found to remain constant after the first cycle. Hannink et al[76] studied the nucleation and growth of tetragonal phase in Mg, Ca and Y-PSZ. They found that the precipitation was completed during initial fast cooling and subsequent ageing only coarsened the precipitates. Garvie et al[75] fired Ca-PSZ in the cubic phase field temperature and fast cooled to 1300^{0}C. Subsequent ageing of the samples were done at 1300 to 1500^{0}C. Nucleation and precipitation of the tetragonal phase were complete during cooling. Subsequent ageing increased precipitate size. Bhathena et al[77] suggested that tetragonal particles nucleate homogeneously and they were clustered into planar arrays by autocatalytic nucleation above a certain temperature. Individual particles in the arrays were closely spaced and it was suggested that their transformation to the monoclinic phase was by strong interaction effects whereby the group behaved as a single particle. Hannink et al[76] aged Mg-PSZ and found that thermal shock, which was also measured by retained strength, could only be improved by optimal ageing. Materials were aged in the sub and super-eutectoid range above and below tetragonal solidus line in the phase diagram. Sub-eutectoid ageing gave better initial and retained strength. Heat treatment at lower temperature transformed tetragonal precipitates to monoclinic by a process other than precipitate coarsening. Schmauder et al[78] studied the degradation of Y-TZP in the presence of moisture at 250^{0}C. The degraded surface layer consisted of totally and partially transformed zirconia grains. Microcracks opened migration paths for water to penetrate into deeper subsurface areas. Masaki[79,80] studied Y-TZP from 1.5 to 5mol % Y_2O_3. Samples were prepared by cold isostatic pressing, hot pressing, and hot isostatic pressing (HIP). Strength reached to a maximum at around 2.7mol% Y_2O_3. HIP had the smallest grain size. Ashizuka et al[81] subjected Y-PSZ to a thermal shock of 300 to 400^{0}C and observed that the retained strength reduced sharply beyond 300^{0}C. Gross et al[82] studied both hot isostatically pressed and air sintered samples. Drennan et al[83] added SrO to Mg-PSZ and found improved mechanical properties. Samples were aged upto 16hrs at 1100^{0}C and it was found that the strength reached a maximum at around 2 hour and then decreased. The sample containing SrO always had a higher strength. Hughan et al[84] identified three types of precipitates in MgPSZ: (1) Primary (2) Large random (3) Tertiary. At around 1300^{0}C the most rapid growth transformable ‘t’ particles occurred. MOR values were measured after ageing at different temperatures. Around 1350^{0}C, maximum strength and fracture toughness values were

observed at around 1350^{0}C. Swain[85] studied the effect of grain size on toughness and transformability of Y-TZP. As the grain size increased, the transformability and toughness also increased. Lange et al[86] studied the low temperature degradation of transformation toughened Y_2O_3-ZrO_2. The tetragonal to monoclinic transformation of Y-PSZ was accelerated within the temperature range of 150 to 400^{0}C in water vapor aging. It was postulated that water vapor draws out sufficient amount of Y_2O_3 from a small volume element on the surface of the grain. This results in Y_2O_3 deficient volume element that transformed to the monoclinic structure. As the monoclinic volume element grew by further diffusion of Y_2O_3, it achieved a critical size where it could spontaneously grow without diffusion. If above the critical size, transformed grain produced microcracks, thereby opening up subsurface grains to react with water vapor. Masaki et al[87] studied the Y-PSZ sintered, hot pressed, and hot isostatically pressed- samples aged in air at 200 to 500^{0}C for 500 to 1000 hrs. There was no change when the grain size was less than 0.5μm and density was greater than 6.0gm/cc. Sato et al[88] annealed the specimen in a humid atmosphere at 80 to 600^{0}C to produce tetragonal to monoclinic transformation. They suggested the following measures to reduce degradation (1) Reduce grain size (2) Disperse a second phase (3) Dope with CeO_2. Whalen et al[89] suggested that the low temperature degradation of Y-TZP in the presence of water vapor could be prevented if after sintering the surface was ground and annealed. Fine tetragonal particles were recrystallized from the surface damaged by grinding. Lapisto et al[90] studied TZP ceramics in the presence of water vapor at 150^{0}C. It was concluded that the grain size and Y_2O_3 content were not sufficient to explain the change in the structure and mechanical properties. Druschitz et al[91] used hot isostatically pressed Yttria-Zirconia and suggested that when the presintered bodies had open pores they could not be densified by HIP. Lu et al[92] added MgO in small quantities to Y-TZP. Densification was enhanced through liquid phase sintering and large grains were grown through solution-diffusion-reprecipitation. Ruiz et al[93] sintered Y-TZP and heat treated those to different temperatures-maximum being 1850^{0}C. The grain size was increased from 0.3 to 10μm at 1850^{0}C. Hwang et al[94] found that mobility of grain boundaries were prevented by divalent and trivalent cations but remained unchanged by tetra and pentavalent cations in case of YTZP and Ce-TZP. Wang et al[95] concluded that the surface toughness of YTZP decreased because of low temperature ageing and postulated that microcrack linking led to reduction in surface toughness. Pan et al[96] investigated the critical phase transformation stress of tetragonal zirconia polycrystalline ceramics. Tetragonal to monoclinic phase transformation was found to be close to its rupture strength. Four stages of

deformation for TZP were suggested; a) anelastic behavior b) t → m transformation c) microcracking d) catastrophic failure. Ishitsuka et al[97] found that toughness mechanism did not function well against thermal stress in Y-TZP. Heuer et al[98] observed that hardness decreasd with increasing temperature in Y-TZP, Mg-PSZ and Ce-TZP. Hannink et al[71] found that principal structural change was associated with particle coarsening during isothermal ageing of Ca-PSZ at 1300^0C. Gao et. al[99] studied the influence of particle size on transformable tetragonal zirconia in hot pressed Y-TZP. There was an optimum particle size range at which the tetragonal as well as transformable tetragonal fractions were the highest. Among several conventional and non-conventional processes, recently sol-gel process has also received a greater attention. Robert L. Jones et al[100] identified that the Sc_2O_3-(10-20%)Y_2O_3 zirconia processed through sol-gel method gave less monoclinic formation, and evidenced better high temperature phase stability than the 100% Y_2O_3-stabilized zirconia during aging at 1400^0C for 140 hours. Recently, A. Mehner et al[101] thoroughly studied the sol-gel derived zirconia coating on steel substrate, where zirconia was first crystallized as metastable, cubic or tetragonal phase. They also observed that above 600^oC annealing temperature monoclinic zirconia transformation occurred rapidly. Simultaneously, a formation of high compressive stresses up to 750MPa was observed due to the volume increase of about 4% that accompanied the t → m transformation. The crystallite sizes of the metastable ZrO_2-films determined in the range of 13 to 20nm. After a couple of years, G. Hare'l et al[102] also reported that the nanocrystalline yttria-tetragonal zirconia polycrystal Y-TZP powders could be prepared by chemical precipitation technique, where the finest particle size was of 3.9nm. This powder was consolidated at 700MPa. X. Bokhimi et al[103] reported that the structure of the zirconia produced by the sol-gel technique was amorphous when the samples were heated below 300^oC. However, it could be noticed that the local order in the amorphous structure was similar to the local order in the tetragonal phase. E.A.A. Mustafa[104] revealed that the precipitated tetragonal phase of 10mol% Ca-PSZ could be partially transformed to monoclinic phase under stresses developed through nucleation and growth when the particle size went above the critical grain size. J.A. Wang. et al[105] studied both the precipitation and sol–gel techniques, where both the tetragonal and monoclinic nanophases coexisted. The tetragonal phase, however, was irreversibly transformed into monoclinic zirconia when the samples were annealed at temperatures higher than 400°C. The inhomogeneity of the precipitated sample gave rise to quasi-amorphous tetragonal zirconia at 400°C. This phase retained a lot of hydroxyls in its structure due to many cationic defects. Yunxia Chen[106] prepared CSZ

uniform, compact and crack free films by the sol-gel method. These films exhibited low coefficient of friction (0.15–0.19) against Si_3N_4. Hui Xu[107] developed highly ordered zirconia nanowire arrays within the pores of anodic alumina oxide (AAO) template membrane. XRD and XPS analyses of the sol-gel synthesis indicate that the nanowires closely resembled and had the cubic zirconia phase. C.R. Rambo[108] manufactured highly porous, biomorphic YSZ (yttria-stabilized zirconia) ceramics, where grain growth and densification after sintering at 1550°C resulted in a porosity between 75 - 82% with a final ZrO_2 grain size of about 3–4 μm.

2.8. Synthesis and Properties of Zirconia in Alumina Matrix

Alumina has been popular as a matrix material along with ZrO_2 because of its high modulus of elasticity. Heuer et al[109] hot pressed the sol-gel derived Al_2O_3-ZrO_2 powder at 1500^0C for 30minutes to observe that the intergranular particles were less resistant to transformation than intragranular ones. Tsukuma et al[110,111] prepared Y-PSZ material by conventional sintering and hot isostatic pressing. Addition of alumina increased the strength from room temperature to 1000^0C. Mazerolle [112] studied the mechanical properties of Al_2O_3-YPSZ material with around 62-65% of Al_2O_3 . Hori et al[113] added ZrO_2 to Al_2O_3. Even small quantities inhibited grain growth thereby increasing strength but reducing fracture toughness. Rytkonen et al[114] compared hot pressed and sintered materials in the Al_2O_3-ZrO_2 system. Fine dispersion of the phases was possible without the presence of agglomerates. Rajendran et al[115] added Al_2O_3 through the co-precipitation route to YPSZ. Addition of Al_2O_3 helped in the achievement of higher bulk density. There was no degradation of the material after autoclaving at 175^0C for 24hours. Alexander et al[116] studied the Al_2O_3-ZrO_2 composites where zirconia was the minority phase. They concluded that M_s temperature increases with increasing zirconia grain size. Claussen et al[117] obtained mullite alongwith zirconia through in-situ reaction starting from zircon and alumina. They suggested a separation of sintering/densification at around 1400^0C and completion of reaction at higher temperatures to form mullite. Heuer et al[109] studied alumina-zirconia composites to find out the stability of tetragonal particles wherein ZrO_2 was varied upto 16vol %. They found that intergranular grains were less resistant to transformation than intragranular ones. White et al[118] prepared green bodies of ZrO_2-Al_2O_3 and Al_2O_3 from concentrated slurries. ZrO_2 -Al_2O_3 samples had about 30% higher room temperature strength. Grathwhol et al[119] subjected ZrO_2-Al_2O_3 to a narrow range of stresses near ultimate strength and observed that the specimens had higher residual strength. Park et al[120] sintered YTZP-Al_2O_3 by microwave heating resulting in

smaller grain size. Garvie et al[1] prepared zirconia-alumina samples with volume fraction of 4 to 15% of the dispersed phase. It was found that at any temperature, critical grain size (d_c) for transformation was dependent on interparticle spacing. Reciprocal critical size had an inverse linear relationship with temperature in the range of 800 to 1125^{0}C. Srikrishna et al[121] formed mullite/Zirconia by reaction sintering of zircon and alumina. Addition of TiO_2 within certain limits could improve the mechanical properties. Tsubakino et al[122] improved the mechanical properties of YPSZ with addition of alumina. Formation of amorphous phase located at the grain boundary was identified to be the cause for the improvement. Kibbel et al[123] studied 15 and 10 vol % ZrO_2 in the Al_2O_3-ZrO_2 system for ripening of grains at 1600^{0}C. In the former composition, tetragonal to monoclinic ratio was 4 and tetragonal particles were intergranular. In the lattice t : m ratio was 19 and most of the particles were inetrgranular. Intergranular particles coarsened by coalescence whereas intragranular particles coarsened at a much slower rate by interfacial diffusion kinetics. Oh et al[124] applied low pressure (2MPa) during presintering to avoid differential densification which led to the creation of voids. Wallace et al[125] developed dense mullite-Zirconia by insitu reaction in a two step sintering cycle; first to densify at 1400^{0}C and then to complete the reaction to form mullite at 1575^{0}C. ZrO_2 particles were rounded evidently due to their growth in a nanocrystalline mullite matrix. Porter et al[126] obtained mullite by reacting Al_2O_3 and SiO_2; and mixed it with different varieties of zirconia. The improvement of strength was noticed by the addition of ZrO_2 if the original matrix had higher porosity (more than 20%). It was suggested that besides stress induced transformations other mechanisms like grain boundary strengthening and crack-deflection could be operative as the fracture toughness variations was small. Rincon et al[127] developed mullite/zirconia composites by in situ reaction sintering with TiO_2 additions. TiO_2 increased the solid solution of ZrO_2 in mullite and itself formed a solid solution with mullite. At low temperature, ZrO_2 was absent in the glassy phase but substantial amount was present at high temperature. W.F. Klading[128] investigated the influence of the type of ZrO_2, stabilized or unstabilized, in variation from 5 to 40wt% in Al_2O_3 matrix. Tetragonal Y_2O_3 contained in ZrO_2 (TZP) helped to promote a considerable growth in strength in the temperature range of 1600 to 1640^{o}C with a maximum of around 600MPa when a 30wt% concentration of 5wt% Y_2O_3 - ZrO_2 in $A1_2O_3$ was used. They also noticed unstabilized m-ZrO_2 did not show any toughening effect; it even led to a remarkable loss of strength if the particle size used was overcritical. The smaller particles of unstabilized zirconia induced good bending strength of around 400MPa, whereas

those composites containing 0.7 μm particles lost their strength remarkably below that of the matrix material (alumina), with higher zirconia concentration.

A thorough investigation was carried out by G. Orange et al[129], they prepared Al_2O_3-ZrO_2 composites through conventional routes (commercial raw powders, mechanical mixing, pressureless sintering or hot pressing). Optimum mechanical properties were observed for 5vol% ZrO_2 addition in pressureless-sintered materials and 10vol% ZrO2 for hot-pressed materials. The σ_f and K_{IC} were considerably enhanced with increase of 3Y-TZP. Microcrack toughening is a less energy-dissipative mechanism but it is quite temperature-independent in these cases. A. Leriche et. al[130] prepared ZTA materials containing zirconia (5-45vol.%) and yttria (0-3mol% zirconia) from commercial ceramic powders by different techniques of homogenization, shaping and sintering. Hot pressed ZTA specimen exhibits finer microstructure with compare to isostatic pressing or slip casting, followed by pressureless sintering, when zirconia content is less than 20vol%. Laser ablation technique had been adopted to synthesize the ultrafine zirconia and magnesia powder[131], where tetragonal phase in pure ZrO_2 powder was transformed continuously (between approximately 400 and 1000°C) to the monoclinic phase. On addition of 5vol. % MgO, the transformation temperature could be increased by about 400^0C and grain growth suppressed. The isostatically pressed 90vol.% Al_2O_3 + 10 vol.% ZrO2 (with 5 vol.% MgO) specimens were sintered in the temperature range 1400-1600°C. The specimens achieved high density (98%), microhardness (17.8GPa) and toughness (7.2MPa.$m^{1/2}$). C. C. Chen et al.[132] observed the presence of intra or intergranular zirconia particles in alumina matrix and it was dependent on the aging time in case of coprecipitated process. Here, the ZrO_2 grain size and t-ZrO_2 content could be controlled by aging treatment, which produced higher than 99% relative density at 1550^0C for 4 hours at sintering (with precursors calcined at 900^0C for 1h. under the condition of 900^oC for 1 hour calcination and 1550^oC/4 hour sintering. V. Srdie[133] showed that zirconia particle changed the route of the transitional alumina phase transformations, shifting the stability of the γ-alumina, and consequently the stable α-alumina formation, toward higher temperatures than in the pure alumina system (for up to 150°C). M. Balasubramanian et al. [134] synthesized 12.5wt% zirconia containing ZTA material, where spray dried powder were spherical in nature. The spray-dried powder was sintered well due to its lower particle size and sphericity. The mechanical properties of the sintered specimens were better than those of the irregular samples because of the higher amount of t-ZrO_2, and their higher density. Another group of researchers[135] investigated that hot pressing reduced the residual stresses, which result from

the mismatch in thermal expansion coefficients, of alumina/zirconia (3Y-TZP) composites. They also postulated that mixing zirconia with alumina might substantially reduce the densification rate, but it would only change the modulus in proportion to the amount of zirconia in the mixture (rule of mixtures). D. Jayaseelan[136] prepared alumina–zirconia (pure zirconia, 12 mol % ceria stabilized zirconia and 3 mol% yttria stabilized zirconia) composites containing 5, 10, 15, 20 and 25vol.% zirconia by sol-gel technique. Around 98% theoretical density could be achieved under the condition of 950°C for 3hour calcination and pressureless sintering at 1530°C for 3 hour, which exhibited better mechanical properties. They also reported that the sol-gel derived more than 99% dense ZTA have intergranular zirconia particles along the alumina grains, although few grains were also found to be of intragranular type. The intergranular grain was pinned down the motion of the alumina grains[137]. R. N. Viswanath[138] also synthesized (Y-TZP) alumina nanocomposite by sol-gel route. These crystallization temperatures increased with Al_2O_3 concentrations, where the grain and grain boundary regions were crystallized independently at 750^{o}C and 950^{o}C respectively. H. Ferkel[139] established that short ball-milling procedure decreased the amount of strong agglomerates in nanopowders. Green bodies pressed from this modified powders exhibit up to 15% higher densities than bodies prepared from the unmodified material. The materials having around 99% of the theoretical density and grain size less than 500 nm could be manufactured under simplified processing conditions. B. Kerkwijk[140] established the tribological behavior of colloidal process derived Y-TZP and ZTA, where the coefficient of friction of Y-TZP as high as 0.8 and as low as 0.45 respectively against alumina balls. The wear rate was the highest for Y-TZP, $10^{-6}mm^3/Nm$ and the lowest for ZTA, $10^{-9}mm^3/Nm$. N. Enomoto[141] prepared Al_2O_3-ZrO_2 composite through wet-chemical process. The crystalline bayerite formation was controlled through dilution of ammonia solution or with an ammonia gas flow at high temperature. By optimizing the precipitation process and the calcination temperature (1100°C), they prepared the uniform microstructure in which t-ZrO_2 particles of ~30nm were finely dispersed within the alumina grains. In the same era, ZTA ceramics were also conventionally prepared by mixing Al_2O_3, Y–TZP and sintering aids in water for 2hours, followed by isostatic pressing at 200MPa and sintering at 1450^{o}C for 2 hour in air[142]. They observed 93% of the t-ZrO_2 fraction was retained for the unaged material when 3mol% Y_2O_3 was added. At 2000 hours ageing time the fracture toughness went up to 7.2MPa.$m^{1/2}$. However, strength increased to 680MPa for short ageing time, then dropped gradually as ageing time increased to 2000h. A.H. De Aza[49] developed alumina–zirconia nanocomposite,

which can be used as ceramic joint prosthesis because of high resistance to crack propagation. Low zirconia (10vol%) content ZTA exhibited almost similar hardness with compared to alumina and were also not susceptible to the hydrothermal instability. He also[143] synthesized different ZTA composites, using either unstabilized or yttria-stabilized zirconia. The materials were prepared in the range 0–15-vol% ZrO_2, using two processing methods: powder mixing and a modified colloidal route. Al_2O_3-10vol%ZrO_2 composite exhibited best slow-crack growth behavior under double torsion method. However, this trend was inverted when volume fractions beyond 10vol%. X.W. Huang[144] prepared a range of ZTA ceramics with addition of 1 wt% TiO_2–1 wt.% MnO_2 and 2wt.% CaO–Al_2O_3–SiO_2 (CAS) as sintering aids. At 1400^{o}C, fully dense specimen exhibited equiaxied grains and their size decrease with addition of zirconia content and mechanical properties improved with ZrO_2 content. When 50vol.% was added, strength and toughness of composite reached 619±36MPa and 7.02±0.06MPa.m$^{1/2}$, respectively. Simultaneously, D. Casellas[145] observed that microstructure coarsening in ZTA followed the correlation (quadratic power law) described on the basis of systems formed by second phase, which increased the fracture toughness and decreased the hardness of the synthesized material. A. P. Quintina[146] revealed that the sol-gel based process of ZTA allowed a better control of final microstructure than the powder based process and it was shown that materials with good mechanical properties could be improved with a better control of porosity. The same composites were also prepared from viscous non-polar suspensions of alumina and zirconia powders by A. Dakskobler[147]. The flexural strength and K_{IC} for the final composite could be noticed 710MPa and 7.1MPa.m$^{1/2}$ respectively. The flexural strength increased due to the strengthening effect of the zirconia phase for layer-microstructure refinement. This strengthening effect was much larger than what had been typically observed in conventional zirconia-toughened alumina composites containing a comparable amount of dispersed zirconia particles. S.T. Aruna[148] et al. synthesized (less than 10nm) ZTA particle through solution combustion synthesis, which was controlled by the proper fuel ratio and the energetic of the combustion reaction.

The above discussion reveals that several compositions and procedures have been developed for the processing and characterization of composites but the exclusive and systematic report on the synthesis and thermo-mechanical properties of ZTA composite have not dealt with. However the addition of uncalcined precursor with the calcined one to achieve physico-chemical properties has not been reported yet elsewhere. This combination of uncalcined precursor and calcined powder may have impact on the primary nucleation,

distribution of particles and densification characteristics and thermo-mechanical properties of the sintered specimens. On this background, this research project is highlighted as a glance view of the development of thermo-mechanical properties of zirconia toughened alumina processed from the mixture of uncalcined and calcined precursor derived by sol-gel route.

2.9. Physical Properties of Alumina, Zirconia and ZTA

Typical mechanical and thermal properties data of Al_2O_3, PSZ, TZP and ZTA (for e.g. $85Al_2O_3$-$15ZrO_2$ (wt %)) obtained through powder mixing route by earlier researchers are summarized in Table 2.1.

Table 2.1. Typical physical properties of Al_2O_3, PSZ, TZP and ZTA

Physical Properties	Al_2O_3	ZrO_2		ZTA
		Mg-PSZ	3Y-TZP	
Density, (gm/cc)	3.96	5.6	6.05	4.1
Mechanical				
Hardness, (Vickers)	2085	1120	1400	1750
Modulus of Elasticity, (GPa)	370	350	205	310
Flexural Strength (RT), (MPa)	400	545	800	760
Compressive Yield Strength, (MPa)	3000	1700	2000	2900
Poissons Ratio	0.22	0.31	0.30	0.23
Fracture Toughness, ($MPa.m^{½}$)	4	8-15	9.5	6-9
Thermal				
CTE, 25-1000°C, ($x10^{-6}$/°C)	8.2	10	10	8.3
Specific Heat Capacity, (J/kgK)	850	400	400	885
Thermal Conductivity, (W/mK)	30	2.2	2	23
Thermal Shock Resistance (ΔT_c)	< 300	375	250	300
Maximum Service Temperature, Air, (°C)	1750	1000	1000	1600

2.10. Structural Applications of Zirconia Bearing Composites

Products made of new composite ceramics and refractories containing ZrO_2 particles as a dispersed phase outperform those made of conventional materials by several hundred percent. Mg-PSZ (magnesia partially stabilized ZrO_2) materials strengthened by transformation-toughening and surface compressive stresses have been tested successfully in such hard-wearing applications as tappet facing materials, powder compaction dyes and dry bearings. Suitable heat treatments induce thermal shock resistance in these ceramics for application as hot extrusion dyes and components for vehicular engines. Al_2O_3-ZrO_2 materials have enhanced toughness, strength and wear resistance due to a combination of microcracking and surface strengthening mechanisms. Consequently, the efficiency of industrial grinding

wheels and metal cutting tool bits, made of these materials compared to those using Al_2O_3 alone, has increased 8 and 3 fold, respectively. A different type of microcracking toughening mechanism is utilized in $ZrSiO_4$-ZrO_2 materials, which are strong, dense and thermal shock-resistant. This new class of "refractories" has been tested successfully as low-cost, high-performance tundish nozzles for the continuous casting of steel. It may be concluded that ZrO_2-based materials compromise an authentic revolution in the development of brittle materials.

2.10.1. Applications of PSZ materials

The preferred alloying oxide for the PSZ ceramics is MgO, because it allows more opportunity for microstructural engineering than CaO or Y_2O_3. In this regard, PSZ ceramics are leading candidate materials because of their exceptional strength, toughness, low coefficient of friction and thermal expansions compared to steel. This material has enormous applicability in structural applications. The economic advantage of using PSZ dyes is their very long, maintenance-free 4-fold life compared to that of the competing high-alloy metal dyes, such as stelite. Further advantages of ceramic dyes are the superior surface finish and dimensional control of the extruded product. A potential application of enormous technological and economic impact is the use of ceramics in vehicular engines. The adiabatic diesel engine with no cooling system is an attractive and promising concept. The engine runs hot and is, therefore fuel-efficient; the savings in fuel and increase in power, to be expected from this design are 22% and 37%, respectively. In recent years, alumina has been used successfully as an alternative prosthetic material. However, PSZ materials are superior to commercial alumina ceramics in all the important mechanical and wear properties. For example, PSZ possesses a higher Weibull modulus, superior wear resistance and lower susceptibility to stress corrosion than alumina. Mg-PSZ also shows great resistance to wear and is a potential material for applications involving abrasive slurries, such as linings for hydrocyclones used to fractionate aqueous slurries of minerals in the mining industry and also as components and linings for pumps.

2.10.2. Applications of Al_2O_3-ZrO_2 materials

Historically, toughened abrasive grain for industrial graining wheels was the first application of alumina-zirconia alloy material. Material scientists are already familiar with alumina–zirconia composites. Since both materials are biocompatible, this could prove to be a

new approach to implants. Two kinds of composites can be prepared in this system: a phase-stabilized zirconia matrix reinforced with alumina particles, alumina toughened zirconia (ATZ) or an alumina matrix reinforced with zirconia particles, zirconia toughened alumina (ZTA). With both the materials, higher toughness values than with the monophase ceramics can be reached but higher values are expected for ZTA composites. ZTA is a high purity combination of the low cost of alumina and high strength of zirconia. ZTA is a ceramic–ceramic composite with good mechanical properties. The enhanced strength and toughness have made the ZTAs more widely applicable and productive than conventional ceramics and cermets in machining steels and cast irons. ZTA ceramics are attractive materials due to the combination of both ZrO_2 and Al_2O_3 properties. ZTA exhibits a considerable improvement in strength and more importantly toughness. It is three to four times more abrasion resistant than high purity alumina. ZTA exhibits a fracture toughness of 7MPa.$m^{1/2}$, hardness of 15GPa and flexural strength of 910MPa. As a result, these ceramics can be used in areas of extreme mechanical abrasion and thermal shock. It is used in cutting tools and nozzles for spraying of abrasives. ZTA ceramics must also be considered as bio-implants. The presently used materials, stainless steel and high density polyethylene (HDPE), have deficiencies in that the metal suffers fatigue and corrosion while the HDPE creeps and has an unacceptably high rate of wear in knee prostheses. Recent in vivo tests of six months duration showed that PSZ ceramics were biocompatible and did not suffer degradation of properties.

2.10.3. Refractory Application of Zirconia Composite Materials

Traditional refractories have a useful degree of thermal shock resistance at the expense of their inherent strength. These materials work only because the microstructure is porous, with many coarse grains. Such materials do not store significant amounts of elastic energy during thermal shock. However, they are susceptible to enhance slag attack and erosion by flowing molten metal. This situation is improved dramatically by dispersing m-ZrO_2 particles of the appropriate size and amount in a suitable matrix phase. It is now possible to design refractories that are dense, strong and thermal-shock resistant.

Approach of the thesis

After consideration of different synthesis processes, properties and applications, the approach used to study the formation of alumina-zirconia composite precursor following the sol-gel route focuses on the structure, property and close control of the process parameters on

every stages of the reaction. An overview of reaction path and some of the more fundamental questions concerning the thermo-mechanical properties have been discussed.

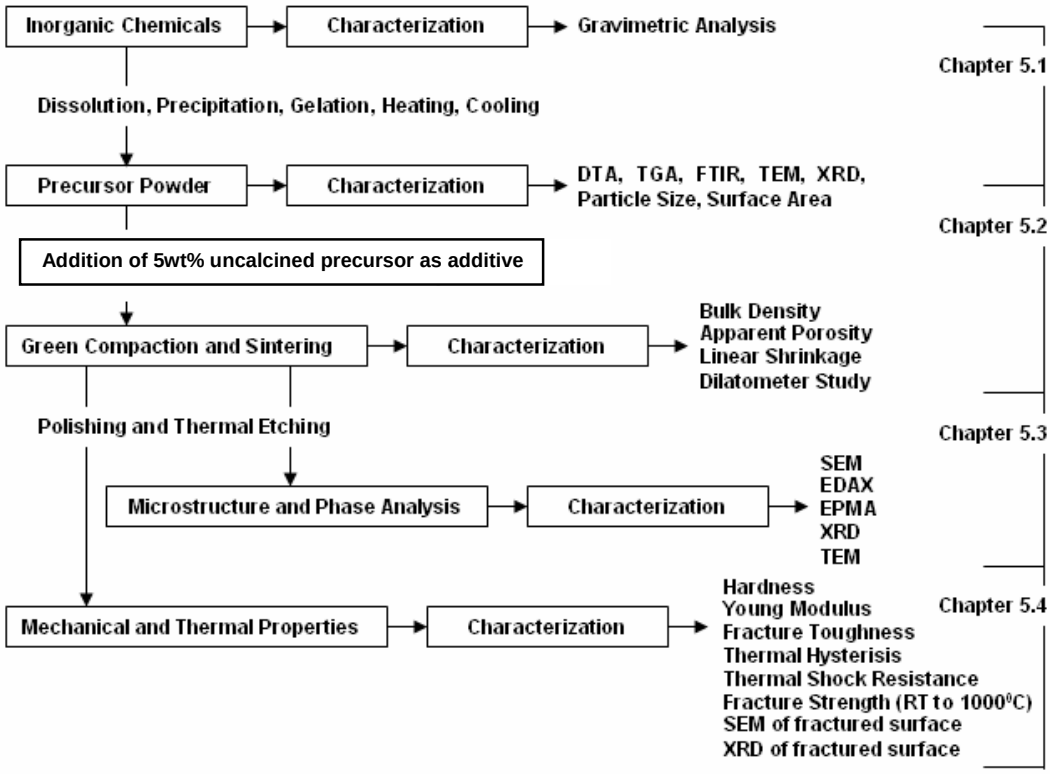

Fig.2.9. Aim and approach of the present research work

The results and relevant discussion are systematically discussed in Chapter 5, along with its various advantages and disadvantages with respect to other routes. A brief flow chart, showing stages studied in the thesis, is displayed in Fig. 2.9. Chapters 5.1 through 5.4 follow the analysis from the precursor powder synthesis to evolution of the microstructure and thermo-mechanical properties of a series of Al_2O_3-ZrO_2 composite materials. Each chapter of this thesis examines a particular stage of the route to prepare an overall picture of the route.

CHAPTER 3

3.0 OBJECTIVE

The extensive literature survey reveals that the synthesis of alumina-zirconia composite precursor through chemical route has been attempted by number of researchers. Simultaneously, the thermo-mechanical properties of zirconia toughened alumina (ZTA) following solid-state route as well as precursor powder derived from chemical route are also discussed by different schools in content with zirconia toughening phenomenon. However, the thermo-mechanical properties of 5-15mol% zirconia dispersed alumina synthesized through chemical route has not yet been reported according to best my knowledge. Moreover, the concept of addition of uncalcined powder as additive is also attempted. Hence, objectives of the present investigation can be summarized as follows:

1. To obtain the series of zirconia (5-15mol %) dispersed alumina precursor powders from multiphase hydrogel systems of Al- and Zr-hydroxides.
2. To analyze the thermal behavior of precursors with respect to zirconia content.
3. To evaluate the bonding mechanism of precursors at elevated temperature with respect to zirconia addition.
4. To study the morphology of the particles and crystallization behavior with respect to temperature and zirconia addition.
5. To study the densification behavior of Al_2O_3-ZrO_2 system without addition of any external additive or organic binder.
6. To analyze the phase content and its distribution through microscopic analysis as well as average grain size after sintering.
7. To study different mechanical properties like: hardness, fracture toughness, elastic modulus and correlate with microstructure
8. To obtain the high temperature fracture strength and estimated the change in critical temperature with respect to zirconia addition.
9. To obtain and analyze the thermal shock behavior with respect to zirconia addition.
10. To obtain the coefficient of thermal expansion and variation of martensitic temperature with respect to zirconia addition in alumina matrix.

CHAPTER 4

4.0. EXPERIMENTAL WORK

4.1. Characterization of Chemicals

Aqueous solutions of Aluminum Nitrate ($Al(NO_3)_3.9H_2O$) (E-Mark, India) and Zirconium Oxychloride ($ZrOCl_2.8H_2O$) (E-Mark, India) were used as the starting materials. Prior to addition of ammonia, chemical analysis was carried out for both the solutions to assess the percent yield.

Determination of Al_2O_3 and ZrO_2 Content

187.5gm $Al(NO_3)_3.9H_2O$ and 161.13gm $ZrOCl_2.8H_2O$ was weighed accurately and were dissolved separately in 1 litre water to prepare 0.5(M) solution. Both of the solutions were stirred vigorously until solutions became clear. The chemical analysis of both the solutions was carried out by gravimetric method. 5ml 0.5(M) solution was taken in 250ml volumetric flask and make up the volume with deionized water. 25ml aliquot was taken in a 500ml beaker and 50ml deionized water was added to it, 2-3 drops methyl red indicator was added to the solution and color of the solution became light red. The ammonium hydroxide/ammonium chloride buffer solution was added drop wise with continuous stirring till complete the reaction (at pH 10 and color of the solution changed from red to pale yellow). The suspension was warmed and filtered through Whatman 41 filter paper. The residue was washed thoroughly with 1% ammoniacal NH_4NO_3 solution. The precipitate along with the filter paper was collected in a preweighed crucible and ignited in a muffle furnace at optimized temperature for 1h. The difference in weight was reported as respective oxides. The relevant chemical reactions during the precipitation and ignition can be summarized as equation (4.1) and (4.2):

$$Al(NO_3)_3.9H_2O + 3NH_4OH \xrightarrow{pH=10} Al(OH)_3\downarrow + 3NH_4NO_3 + 9H_2O$$

$$2Al(OH)_3 \xrightarrow{Heating} Al_2O_3 + 3H_2O\uparrow \quad \ldots\ldots\ldots\ldots\ldots\ldots (4.1)$$

$$ZrOCl_2.8H_2O + 2NH_3 \xrightarrow{pH=10} Zr(OH)_4\downarrow + 2NH_4Cl + 5H_2O$$

$$Zr(OH)_4 \xrightarrow{Heating} ZrO_2 + 2H_2O\uparrow \quad \ldots\ldots\ldots\ldots\ldots\ldots (4.2)$$

Following above reactions, 1liter of 0.5M $Al(NO_3)_3.9H_2O$ and 0.5M $ZrOCl_2.8H_2O$ solutions produced 21.3 gm and 56.8 gm Al_2O_3 and ZrO_2, respectively.

4.2. Powder Synthesis

A calculated amount of precursor powders was prepared through sol-gel route. The 0.5M aqueous solutions of $Al(NO_3)_3.9H_20$ (E-Mark, India) and $ZrOCl_2.8H_2O$ (E-Mark, India) were used as the source of Al_2O_3 and ZrO_2.

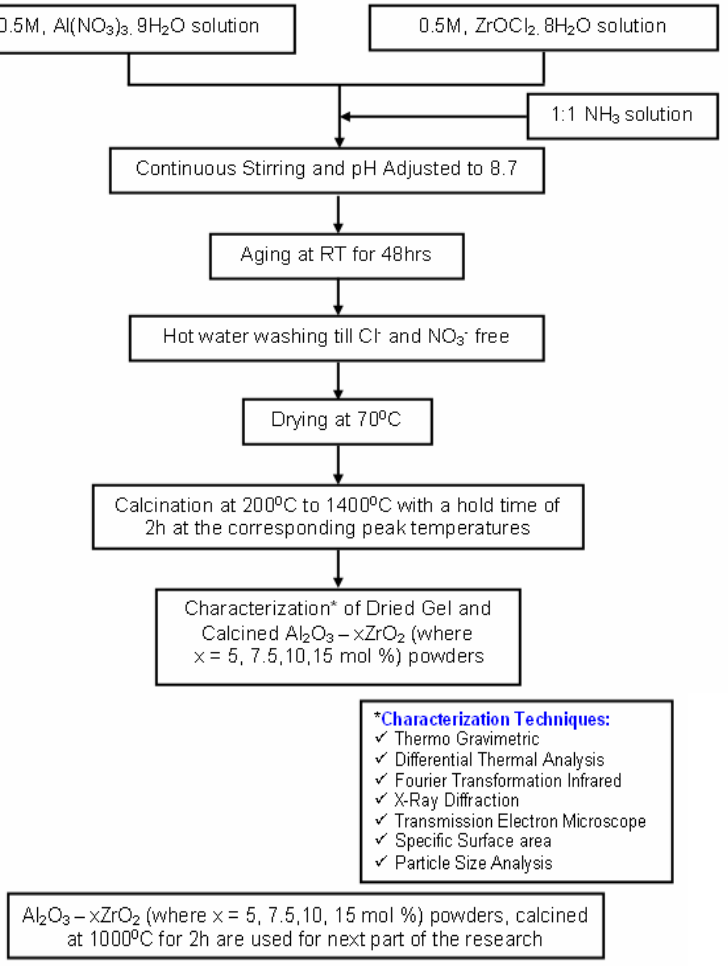

Fig.4.1. Synthesis and Characterization of ZrO_2 dispersed Al_2O_3 precursors.

Initially, the requisite amount of aluminium nitrate and zirconia oxychloride solutions were mixed to achieve different Al_2O_3-$xZrO_2$ (where x = 5, 7.5, 10 and 15 mol %) batches. The individual batch composition is mentioned in section 4.3. The mixed hydrogel was achieved by adding 1:1 NH_3 solution into the mixed aqueous solutions maintained at 25°C with continuous stirring by a magnetic stirrer. Fig. 4.1 represents the process methodology. The

viscosity of the batch gradually increased and finally set to an enblock gel at pH ~ 9. The gel was then aged at room temperature for 48 hours. Subsequently, the gel of each composition was washed repeatedly with boiling distilled water to remove chloride and nitrate ions and filtered. The dried gels were calcined in air in a muffle furnace at different temperatures varying from 200^0C to1400^0C with 2 hours soaking at peak temperatures. The composition of each batch has been listed in Table 4.1.

Table 4.1. Identification of Al_2O_3-ZrO_2 powder precursors

Batch No.	Identification	Al_2O_3 (mol%)	ZrO_2 (mol%)
1	A1Z	95	5
2	A2Z	92.5	7.5
3	A3Z	90	10
4	A4Z	85	15

4.3. Dried Gel and/or Powder Characterization

The decomposition behavior of hydro-gel was evaluated through thermal analysis. The phase content, crystallite size, particle size distribution, surface area, particle morphology, and bond behavior of calcined powder as well as dried gel were investigated systematically.

4.3.1. Thermal Analysis (TGA & DTA)

The thermal analysis technique is an excellent device for determining the presence and quantity of hydrated water, which also aids to determine the oxygen content. Additionally, it can give an idea about decomposition behavior, phase transitions, formation of products etc. from precursor powders synthesized through different chemical routes.

Thermo Gravimetric (TG) and Differential Thermal Analysis (DTA) analyses were carried out in (STA 409C) system in air with the heating rate of 10^oC per minute with Al_2O_3–ZrO_2 dried gel. Samples were ground to make fine powders. For TGA, sample was loaded onto an accurate balance and heated at a controlled rate, to record the weight loss at different temperatures. When a material undergoes physical or chemical change it absorbs or releases thermal energy which is a characteristic of the range. The temperature difference of a sample

with respect to a reference inert material (α-Al_2O_3) during heating or cooling is shown in a DTA as the deviation from zero base line. Exothermic or endothermic changes are shown in opposite directions of the baseline.

4.3.2. Fourier Transformed Infrared (FTIR) Analysis

Fourier transformation is a mathematical operation used to translate a complex curve into its component curves. In a Fourier Transformation Infrared instrument, the complex curve is an interferogram, or the sum of the constructive and destructive interferences generated by overlapping light waves, and the component curves are the infrared spectrum. An interferogram is generated because of the unique optics of an FTIR instrument. The key components are a moveable mirror and a beam splitter. The moveable mirror is responsible for the quality of the interferogram, and it is very important to rotate the mirror at constant speed. For this reason, the moveable mirror is often the most expensive component of an FTIR spectrometer. A beam splitter is just a piece of semi-reflective material, usually mylar film sandwiched between two pieces of IR-transparent material. The beam splitter splits the IR beam 50/50 to the fixed and moveable mirrors, and then recombines the beams after being reflected at each mirror. The standard infrared spectrum is then calculated from the Fourier-transformed interferogram, giving a spectrum in percent transmittance (%T) vs. light frequency (cm^{-1}). Fourier transformation infrared analysis of dried gel and calcined powders were done at a resolution of 4 cm^{-1}. Chemical groups on the surface of calcined powders were analyzed by Diffuse Reflectance Infrared Fourier Transformation (Magna IR560, Nicolet) in the wave number range 400 to 4000 cm^{-1}. A small amount of sample (0.2gm) was thoroughly mixed with ground KBr in an agate mortar and a disc was prepared in vacuum maintaining a pressure of 33 kg/cm^2. The spectrogram of the sample is observed on a video monitor and a graphic representation of the spectra was taken.

4.3.3. Powder Morphology (TEM) and Element analysis (EDAX)

Transmission Electron Microscopy (TEM) analysis technique has a distinct advantage from SEM because the electrons are highly energised, and because imaging is the result of electrons having passed through the specimen, either to fluoresce on an imaging plate or to an exposed photographic film. The technique generally takes advantage of the very short wave-length of high energy electrons and their capability to extract information from very short distances, e.g., inner-atomic distances. This electron probe technique especially provides more

accurate results for ultra thin specimens (in the order of nanometers, only several inner-molecular distances).

The diffraction pattern and image are formed at the back focus plane and image plane of the objective lens. If back focus plane is taken as the objective plane of the intermediate lens and projector lens, the diffraction pattern will be observed on the screen. The TEM works in diffraction mode. If the image plane of the objective lens is considered as the objective plane of the intermediate lens and projector lens, image will be formed on the screen. This is called image mode.

EDX Analysis stands for Energy Dispersive X-ray analysis. It is sometimes referred to also as EDS or EDAX analysis. It is a technique used for identifying the elemental composition of the specimen, or an area of interest thereof. The EDX analysis system works as an integrated feature of an electron microscope, and can not operate on its own without the latter. During EDX Analysis, the specimen is bombarded with an electron beam inside the electron microscope. The bombarding electrons collide with the electrons of the specimen atoms', knocking some of them off in the process. A position vacated by an ejected inner shell electron is eventually occupied by a higher-energy electron from an outer shell. To be able to do so, however, the transferring outer electron must give up some of its energy by emitting an X-ray. The amount of energy released by the transferring electron depends on which shell it is transferring from, as well as which shell it is transferring to. Furthermore, the atoms of every element release X-rays with unique amounts of energy during the transferring process. Thus, by measuring the amounts of energy present in the X-rays being released by a specimen during electron beam bombardment, the identity of the atom from which the X-ray is emitted can be established.

The output of an EDX analysis is an EDX spectrum. The EDX spectrum is just a plot of how frequently an X-ray is received for each energy level. An EDX spectrum normally displays peaks corresponding to the energy levels for which the most X-rays had been received. Each of these peaks is unique to an atom, and therefore corresponds to an individual element. The concentration of the element is in the specimen is indicated by the high intensity peak in a spectrum.

The particle size and element content of as-synthesized Al_2O_3-ZrO_2 powders were characterized by TEM (JEM 4000 FX) with an EDX attachment. Transmission Electron Microscopy (TEM) was used to estimate the particle size of the powders and to observe the morphology and the state of agglomeration of the powder. TEM observations were performed

in an instrument equipped with a tungsten filament operating at 120 kV (Model JEM-1200EX II, JEOL, Japan) and a point-to-point resolution of 5Å. Powders were dispersed in ethanol using an ultrasonic treatment. A drop of the resulting suspension was placed on carbon-coated copper grids, and then the particle dimensions were measured from micrographs taken with the TEM. Simultaneously, element detection was carried out through EDAX technique.

4.3.4. Phase Analysis by X-Ray Diffractometer

In the powder, thousands of grains have random orientations. With random orientations, it is expected that most of the different atomic planes lie parallel to the surface in some of the grains. Thus, by scanning through an angle θ of incident X-ray beams from 0 to 90^o, diffraction has occurred in a particular angle, and each of these angles would be associated with a different atomic spacing. The instrument used to do this is an X-ray powder diffractometer. A powdered mineral sample is packed on a sample stage so that it can be irradiated by the X-ray tube. To detect the diffracted X-rays, an electronic detector is placed on the other side of the sample from the X-ray tube, and allowed rotate the sample to produce angles from 0 to 90^o. The instrument used to rotate both the X-ray tube and the detector is called a goniometer. The goniometer keeps track of the angle θ, and the detector records the rate of X-rays coming out of the other side of the sample (in units of counts/sec) and sends this information to the computer. The identification of different phases is carried out by powder X-ray diffraction study. For the phase analysis of dried gel and calcined powder, X-ray data were collected using a fully automated Philips X-pert system (PHILIPS PW1830) with Cu-K_α radiation. The voltage and current were set at 35 kV and 30mA respectively with the copper target, with a step size of 0.02^0 (2θ) and a count time of 1s per step. After scan of the sample, the X-ray intensity (counts/sec) was plotted against the angle theta (θ). The angle (2θ) for each diffraction peaks were then converted to d-spacing, using the Bragg equation. The crystal structure and associate each of the diffraction peaks with a different atomic plane in terms of the Miller Index for that plane (hkl) was determined through standard APD software. The tetragonal zirconia fraction X_t was determined by as follows[32,149].

$$X_m = \frac{I_m(111) + I_m(11\bar{1})}{I_m(111) + I_m(11\bar{1}) + I_t(111)} \qquad (4.3)$$

where, I = Area of the specific peak, m = Monoclinic Zirconia, t = Tetragonal Zirconia

4.3.5. Crystallite Size Determination by XRD

The crystallite sizes of the dried gel and calcined powders were determined from X-ray line broadening using the Sherrer's equation as follows[149]:

$$D = \frac{0.9\,\lambda}{\beta \cos\theta} \quad \ldots\ldots\ldots\ldots\ldots\ldots\ldots\ldots\ldots\ldots\ldots\ldots(4.4)$$

where D is the crystallite size, λ is the wavelength of the radiation, θ is the Bragg's angle and β is the full width at half maximum.

Line broadening due to the equipment was subtracted from the peak width before calculating the crystallite size using the following formula:

$$B^2 = B^2_{meas} - B^2_{Equip} \quad \ldots\ldots\ldots\ldots\ldots\ldots\ldots\ldots\ldots\ldots\ldots\ldots(4.5)$$

Where, B_{meas} = measured full width at half maximum from peak values, B_{Inst} = Instrumental broadening. The peak position of X-ray data of Al_2O_3-xZrO_2 (x =5, 7.5, 10 and 15mol %) was determined by the FWHM (full width of half-maximum) middle point method.

4.3.6. Particle Size Distribution

A laser diffraction method with a multiple scattering technique was used to determine the particle size distribution of the dried gel and calcined powder. To measure the particle size through laser scattering method, the instrument correlates between the intensity and the angle of light scattered from the particle, and the particle size is calculated based on the Mie-scattering theory. In order to capture scattered light signals over this range of angles, the equipment utilizes a number of high-angle and back-scatter detectors, together with a short wavelength blue LED laser. As the particle size becomes smaller, the scattered light signal shifts to the side and rear with respect to the light source. Shorter wavelength detects the smaller particle size. The scattered light can be measured by a series of photo detectors placed on the opposite side of source at different angles. This is known as the diffraction pattern for the sample. As the instrument measures clouds of particles rather than individual ones, it is known as an "ensemble" technique, with the advantage that at smaller sizes (e.g. 1 micron), the system measure literally millions of particles which gives some statistical significance to the measured results. The particles size distribution (volume percent) of the suspension was carried out in computer-controlled particle size analyzer (Malvern, Mastersizer 2000, UK) via a software program. The powders must not be agglomerated and completely dispersed in the liquid so that they are separated into discrete unattached particles. A well-dispersed and

agglomerate-free suspension was obtained using Ultrasonic treatment (Sidilu Ultrasonics, India). Powdered samples were used to be well dispersed in a liquid medium of known density and viscosity.

4.3.7. Surface Area

Specific surface area of ultrafine submicron ceramic powder is an important objective to predict the green compaction and sintering characteristics. This can be measured by a common BET method. The BET method (Brunauer, Emmet and Teller after the developers of the basic calculations) involves adsorbing a monolayer of liquid nitrogen onto the surface of particles, then measuring the amount of nitrogen that is released when that monolayer is vaporized. Based on this nitrogen quantity, the surface area of the sample can be calculated from the BET equation[150]:

$$\frac{1}{V}\left(\frac{x}{1-x}\right)=\frac{c-1}{cVm}x+\frac{1}{cVm} \quad \text{.....(4.6)}$$

V = volume of gas adsorbed, V_m = volume of gas adsorbed at monolayer coverage, X = P/Po, P = Ambient Pressure, P_o = total pressure, C, a constant that is related to the heat of adsorption. A plot of (1/V)(x/(1-x)) versus x gives a straight line with slope = m= (c-1)/(cV_m), Intercept = b= 1/cV_m, The value of V_m and c are worked out, V_m = 1/(slope + intercept). This is normalized by the mass of particles tested to give a specific surface area (m^2/gm)

Specific surface area of zirconia dispersed alumina powders was determined by the surface area Coulter SA 3100 BET. Surface area was determined as per BET method. About 2-3 gm of sample was taken in the sample cell and degassed at 110^{o}C in vacuum up to a maximum of 3mbar. The sample holder mouth was closed by a stopper. Sample was cooled and the cell was placed in liquid nitrogen bath. The equipment measured the amount of gas adsorbed on the surface of the sample and calculated the specific surface area.

4.4. Preparation of Sintered Specimen

Calcined (1000^{o}C/2h) powders were used as source material and corresponding 5 weight percent uncalcined dried gel of each batch was used as primary binder. The powders were pressed without any external binder. The green $A1_2O_3$-xZrO_2 (x = 5, 7.5, 10, 15 mol%) samples were sintered with different sintering profile and soaking time as and when an

experiment was conducted. The green samples were used to determine the shrinkage behavior, whereas the sintered samples were used to characterize the densification behavior, and thermal and mechanical properties.

4.4.1. Fabrication of Green Discs/ Billets

The nano-powder synthesis methodology and their characterization have been analyzed and explained in section 4.1. The synthesized powder of each batch was thoroughly mixed with its corresponding dried gel and was processed as per the flow sheet (Fig 4.2). The typical batch identification and composition are listed in the Table 4.2.

Table 4.2. Batch Composition of green specimens

Batch Number	Identification	Calcined Powder (1000^0C/2h)	Uncalcined Dried Gel (Binder)
1	A1ZB	95 wt% of A1Z	5 wt% of A1Z
2	A2ZB	95 wt% of A2Z	5 wt% of A2Z
3	A3ZB	95 wt% of A3Z	5 wt% of A3Z
4	A4ZB	95 wt% of A4Z	5 wt% of A4Z

Initially, all the powders and binders were wet milled in acetone media for 24h in high-density polythene bottle for 24 hours using high purity zirconia balls. The mixed powder was dried at 50^0C for 8 hours. Then, the mixed powders were consolidated by uniaxial pressing in high carbon steel mould in a hydraulic press with a capacity of 50 tons. Seventy five pellets (∅12 mm, ~3 mm thick) and seventy billets (5mm x 4mm x 40mm) of each batch were uniaxially pressed at a pressure of 250 MPa for 2 minutes.

Subsequently, uniaxially pressed samples were placed in rubber moulds, followed by vacuum suction to remove air. Sealed rubber moulds were placed inside the cylindrical chamber of isostatic press (laboratory model) in a fluid bath consisting of oil-water mixture. All samples were isoststically pressed at 300 MPa for 2 minutes. Green densities were measured through weight/volume data. Weight was measured from electronic balance, whereas volume was calculated from the dimension of the specimens.

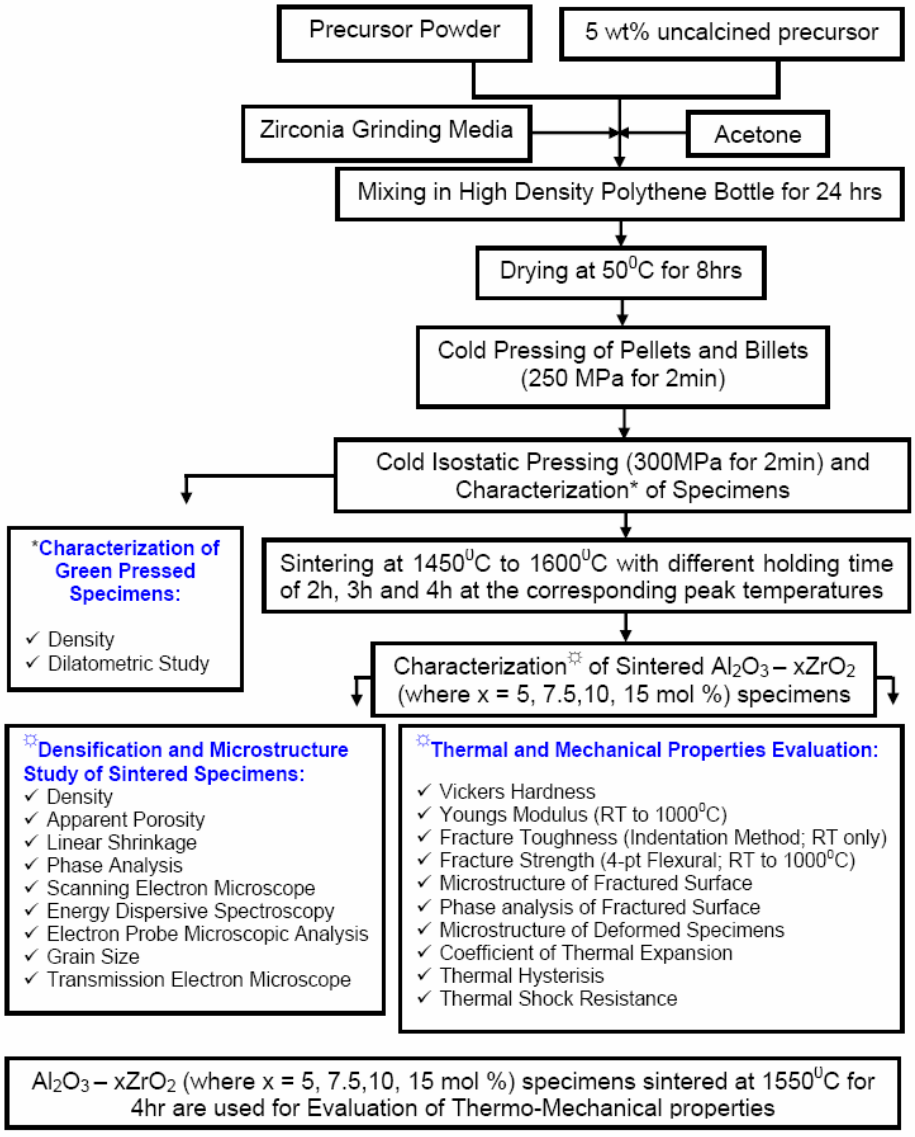

Fig.4.2. A flow chart of densification and characterization techniques

4.4.2. Sintering

The pressed samples were sintered in an electrical furnace with super kanthal ($MoSi_2$) heating elements and alumina insulation boards as chamber walls (size of the chamber 250x150x150mm). The thermal regime of the furnace was controlled through a programmer-cum-controller of 'Eurotherm' within 2^0C. The sintering temperature was varied from 1450^{0}C to 1600^{0}C with an interval of 50^{0}C at different soaking times at the peak temperatures.

The typical sintering profile at 1450^{0}C for 2 hours holding has been illustrated in the Fig 4.3, where heating rate of 10^{o}C/min was maintained up to 1000^{o}C and 5^{o}C/min up to the final temperature. Similar profiles had also been followed to reach the peak temperature with different holding schedule.

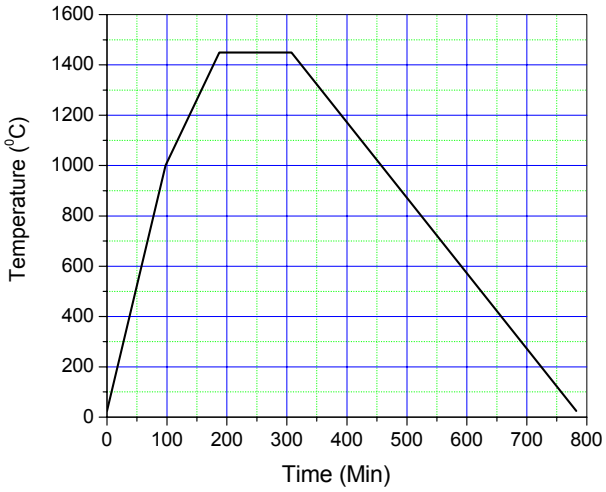

Fig.4.3. A typical sintering profile of green specimens

4.5. Characterization of Sintered Compacts

Sintered discs were used to determine the physical properties, such as densification behavior and phase analysis. The sintered billets were used to determine the thermal and mechanical properties.

4.5.1. Apparent Porosity and Bulk Density

Apparent porosity and bulk density of the sintered specimens were determined by Archimedes' Principle. Sintered samples were weighed in dry state. Samples were immersed in kerosene and kept under a vacuum of 4mm of mercury for two hours to ensure that kerosene filled up the open pores completely. Then, soaked (in kerosene) and suspended weights were measured. From these values we can calculate the apparent porosity and bulk density. All weights were taken in electronic balance (accurate upto 4 place of decimal)

Dry weight of the samples = W_d

Soaked weight of the samples = W_s

Suspended weight of the samples =W_a

$$\% \text{ Apparent Porosity} = \frac{Ws - Wd}{Ws - Wa} \text{ X } 100 \quad \text{.....(4.7)}$$

$$\text{Bulk Density} = W_d / W_s - W_a \quad \text{.....(4.8)}$$

The bulk densities and apparent porosities of sintered pellets are described in section 5.2; however, densities of the billets are also cross checked as above. The relative densities of billets were within variation of ± 2%.

4.5.2. Relative Density

Relative density of different sintered specimens was calculated from the bulk density and theoretical density (obtained from X-ray method). The macroscopic density of a particular specimen, determined from the weight and volume of the specimen, is usually less than, and cannot exceed, the X-ray density, because the macroscopic specimen will usually contain minute cracks and pores. Therefore it is important to determine X-Ray density. By comparing X-ray density with the macroscopic density of the sintered compacts (A1ZB, A2ZB, A3ZB and A4ZB), the percent porosity can be calculated and compared with the measured data. X-ray density is sometimes also called "theoretical density". However, it is not theoretical because it is determined experimentally. Normally, the density of a solid is found by measuring the volume, usually of the order of a few cubic centimeters, and the weight of a particular specimen. But, X-ray diffraction allows us to determine the lattice parameters of a crystal's unit cell, and therefore its volume, together with number of atoms in the cell. So, the base for the density determination should be a single unit cell instead of a few cubic centimeters, by defining[149] the X-ray density = weight of atoms in unit cell / volume of unit cell; $\rho = \sum A/NV$, where, ρ = density (gm/cc), $\sum A$ = sum of the atomic weights of all the atoms in the unit cell, N =Avogadro's number, and V = volume of unit cell (cc). Inserting the value of N, we have,

Table 4.3. Crystal structure and theoretical density of α-Al_2O_3, t-ZrO_2 and m-ZrO_2

Phase	Crystal Structure	a / α	b / β	c / γ	No. of Atoms in unit cell	Σ A	Unit Cell Volume(Å^3)	TD
α-Al_2O_3	Hexagonal	4.759 90	4.759 90	12.991 120	Al = 12 O = 18	611.77	254.8	3.987
t-ZrO_2	Tetragonal	3.6067 90	3.6067 90	5.1758 90	Zr = 2 O = 4	246.45	67.33	6.078
m-ZrO_2	Monoclinic	5.1501 90	5.2077 99.224	5.3171 90	Zr = 4 O = 8	492.89	140.76	5.814

$$\rho = \sum A/NV = \sum A/(6.02257 \times 10^{23})(V \times 10^{-24}) = 1.66042 \sum A/V \quad \ldots\ldots\ldots\ldots\ldots (4.9)$$

where ρ is in gm/cc and V is the unit cell volume in Å^3. The volume of different crystal structure are different for e.g. tetragonal $V=a^2c$, monoclinic $V=abc\sin\beta$, hexagonal $V = 0.866a^2c$

4.5.3. Shrinkage Characteristics

The green samples (A1ZB, A2ZB, A3ZB and A4ZB) were sintered using dilatometer at 1450^{o}C without any isothermal treatment. The temperature was raised at a rate of 10^{o}C /min from the ambient to 1000^{o}C. Thereafter, the temperature was raised at 5^{o}C /min from 1000^{o}C to the maximum sintering temperature. The percentage linear shrinkage has been plotted against corresponding sintering temperatures.

4.6. Microstructure and Phase Analysis

4.6.1. Scanning Electron Microscope (SEM)

Phase assemblage of the materials was analyzed through a Scanning Electron Microscope (SEM). An SEM was used to study the microstructural feature of samples as it had a much higher resolution power compared to an optical microscope. In SEM, a hot tungsten filament electron gun under vacuum emits electrons which pass through a series of electromagnetic lenses. The sample is then bombarded with a fine beam of electrons having acceleration potentials range from 1-30 KV. A part of the beam is reflected as back scattered electrons (BSE) along with low energy secondary electron emission (SE), cathode

luminescence, x-ray excitation beam and electron transmission also take place. Images formed from the (SE) beam were studied in the extrinsic mode of SEM. While the images appeared very real as if they are photographed by ordinary means, the apparent illumination was a function of particle emission rather than radiation. The emitted secondary electrons are detected and displayed on a scanning TV display. A bright image will be the result of high secondary electron emission, while the primary influence on high emission is the surface structure of the specimen. The end result is therefore brightness associated with surface characteristics and an image which looks very much like a normally illuminated subject.

4.6.1.A. Sample Preparation for SEM

Sample surfaces were ground with the help of a series of diamond grinding pad from 1200μm to 15 μm on a polishing machine. The samples were polished with 8 μm diamond paste on a rotating disk. Final polishing was done with 6, 2 and 1 μm diamond pastes to create a mirror finish on a lapping machine. Polished surfaces were analyzed in the scanning electron microscope. Prior to microscopic analysis, the samples were thermally etched at 50^{o}C less than the respective sintering temperature. Thermal etched samples were heated up at the rate of 10^{o}C/min whereas the rate of cooling was 10^{o}C/min initially upto 1000^{o}C/min and subsequently at 5^{o}C/min up to room temperature. The thermally etched samples were mounted on a metal stub with carbon paint. The samples were thin coated with palladium-gold under vacuum of 0.01 torr to make the surface conducting for viewing through SEM. The mounted specimens were studied by SEM (JEOL-JSM840) with an EDAX and EPMA attachments.

4.6.1.B. Energy Dispersive X-ray Analysis

The EDAX analysis was carried out to detect the Al and Zr distribution in sintered specimen (A3ZB, 1550^{o}C for 4h). The basic principle of EDAX method has been illustrated in Section 4.3.5.B.

4.6.1.C. Electron Probe Microscope Analysis

Electron probe micro-analyzers are designed from the ground up for the analysis of x-rays that are emitted from the specimen when probed with an electron beam. The design considerations primarily accommodate three to six wave dispersive X-ray spectrometers

which are inherently large. Specimens prepared for X-ray micro-analysis are generally flat, and the microprobe analyzer is designed to allow only a considerable amount of X and Y translation rather than the specimen manipulation which is typical of the SEM (for example, full rotation and tilt). The heart of EPMA is the wave dispersive technology (WDX) for detecting and counting x-rays. These spectrometers are much more sensitive to low elemental concentrations, however, EDX detector is usually associated with SEM. Concentrations in the range of 500-1000ppm can generally be measured, and for some elements within some types of materials, the detection limit can be as low as 20ppm. The distribution of Al and Zr element in the specimen was detected by this technique.

4.6.2. Grain Size Determination

The grain size was determined using a rectangular intercept procedure, following the ASTM E112-88 standard. The average grain size G was calculated using following mathematical expression:

$$G = \sqrt{\frac{4A}{3.14(ni + no/2)}} \quad \ldots\ldots\ldots\ldots (4.10)$$

where, A is the area of rectangular, n_i and n_0 are the grain numbers in the rectangular and on the rectangular boundary, respectively.

4.6.3. Phase Analysis by X-Ray Diffraction

Monoclinic and tetragonal zirconia fraction was estimated from the as-fired surface of the sintered body by XRD technique. The fundamentals and experimental method have been discussed in section 4.3.4.

4.6.4. Transmission Electron Microscope (TEM) Analysis

Scanning Electron Microscope has a resolution power of 100Å, whereas Transmission Electron Microscope (TEM) can resolve upto 5Å. Hence, a TEM was chosen to perform the analysis of the sintered specimen. Initially, 5 x 5 mm square specimen was cut away from the sintered A4ZB specimen for TEM analysis. The thickness was maintained at ~2mm. The specimen was ground and polished down to 0.7-0.8 mm using diamond as abrasive followed by a 3mm circular disc that was prepared by ultrasonic cutter using SiC powder. Subsequently, dimple grinding was carried out to remove around 60μm from that the

specimen, to develop a ~10μm thin dimple. It was found that a tiny hole was generated at the middle portion of the specimen during dimpling. After 1h, the dimple sample was detached from the hot plate and used for ion beam thinning unit IBT-200 with dual gun. A gun voltage of 5KV and a current of 1 milliamp were maintained. The foil was examined in a TEM-JEOL, JEM-200 CX. Camera length was 55cm. Bright field image was seen at an accelerating voltage ranging from 120 to 160KV.

4.7. Mechanical and Thermal Properties

4.7.1. Sample Preparation for Hardness and Toughness Measurement

Samples were mounted in thermosetting resin by an automatic hydraulic mounting press. Mounted samples were ground on a series of diamond pads in the order (from 180 to 20 μm) using the automatic polishing machine. The samples were subsequently polished with cloth-coated wheel using diamond pastes (having particle sizes 15, 8, 2 and 1 μm). The polished flawless samples were cleaned ultrasonically for the removal of any extraneous particles sticking to the polished surface. These samples were indented by a Vickers' indenter with 49N load and 15 seconds dwell time.

4.7.1.A. Hardness Measurement

The hardness of the materials was calculated from the size of the impression produced under load by a pyramid-shaped diamond indenter. The indenter employed in the Vickers test is a square-based pyramid whose opposite sides met at the apex at an angle of 136°. The diamond is pressed into the surface of the material at loads ranging up to approximately 49N. The size of the impression (usually no more than 0.5 mm) was measured with the aid of a calibrated microscope. The Vickers number (H_V) was calculated using the following formula[151]:

$$H_V = 1.854(F/D^2) \quad \text{……(4.11)}$$

with F being the applied load (measured in Kgf) and D^2 the area of the indentation (measured in mm^2).

4.7.1.B. Fracture Toughness

K_{Ic} was measured by the indentation method, where the length of cracks emanating from the Vickers indentation corners. K_{Ic} was calculated using the expression proposed by Anstis et al.[152] :

$$K_{IC} = 0.016 \left[\frac{E}{H}\right]^{1/2} \frac{P}{C^{3/2}} \quad \text{……(4.12)}$$

Where *E* is the Young's modulus and C is the crack length.

4.7.2. Modulus of Elasticity

The basic material property Elastic Modulus, which is of interest in structural applications, can be determined quickly and easily through computations based on sound velocities. Sound velocity can be easily measured using ultrasonic pulse-echo techniques. The standard 12.5mm smooth parallel bars, which permit clean pulse-echo measurement of sound transit time, were sliced off from sintered bar (35mm) specimens. A V109 5MHz broadband longitudinal wave transducer and a V154 2.25MHz normal incidence shear wave transducer of Panametrics, NDT, USA were used to measure the velocities of the sintered samples using ultrasonic pulse receiver. The round trip transit time was recorded through an area of known thickness with longitudinal and shears wave transducers, and computed. Each reported value was the average of data obtained from five indentation tests.

4.7.3. Flexural Strength

4.7.3.A. Fracture Strength at Ambient Temperature

The determination of the flexural strength is frequently necessary as part of the design of structural ceramics to check compliance with established specifications or to provide information necessary to design an engineering structure. It is the ability of a bar or slab to resist failure in bending. The flexural strength is expressed as "Modulus of Rupture" (MR) in MPa. Generally Flexural Strength is about 10 to 20% of the compressive strength. However, the best correlation for specific materials is obtained by laboratory tests.

Five samples are taken to determine the flexural strength at each test and the average values have been reported here. The flexural strength was determined by the standard 4-pt bending method in an instrument (Instron Universal Testing Machine Model No. 1185) fixture with an outer span and inner span of 30mm and 10mm respectively with cross head speed of 0.5mm/min. The rectangular bars of 35 x 3 x 4 mm were ground on diamond discs (180 and 20μm) of the polishing machine, Planopol 3, Struers, Denmark. The bars were finally polished with diamond pastes of 15, 8 and 1 μm. The tensile edges were chamfered. The flexural strength was calculated from the following equation;

$$\text{Modulus of rupture or Flexural Strength} = \frac{3W(L-l)}{2bd^2} \quad \ldots\ldots\ldots\ldots\ldots\ldots (4.13)$$

where, W = Fracture load; L = Outer Span length and l = Inner span of the bar between the two supporting edges; b = Width and d = Depth of the sample at the fracture plane**.**

4.7.3.B. Fracture Strength at Elevated Temperature

Similarly, high temperature fracture strength was measured (after diamond machining and polishing) by the four point bending arrangements. All tests were performed at different temperatures, in air (up to 1000^0C). The temperature of the furnace (within which the whole assembly was placed) was raised at a rate of 5^oC/minute. Samples were kept at the maximum temperature for 30 minutes. Loading rate was 50kg/minute. The load was transmitted through the load cell transducer and recorded by digital transducer. Flexural strength was calculated as per the equation 4.13.

4.7.4. Analysis of Fractured Surface

The sintered specimens were broken into almost two equal halves after performing the flexural strength at room temperature. The fractographs of fractured surface were studied by SEM (JEOL-JSM840). The stress induced phase transformation was estimated through X-ray diffraction technique. The differences of phase formation are tabulated in Table 5. 4.2.

4.7.5. Thermal Shock Resistance

Rapid fluctuations of temperature generate stresses within a material. Resistance to initiation or propagation of crack under stresses generated due to thermal fluctuations is known as thermal shock resistance. Thermal shock resistance is measured as resistance to weakening or fracture under stresses generated due to temperature fluctuations. Thermal shock resistance is usually evaluated by heating samples to various temperatures (T_{max}). The samples are rapidly cooled by quenching from T_{max} into medium, ambient temperature water (is commonly used for this purpose). The post quench retained strengths are measured and plotted versus the severity of the quench, or $\Delta T = T_{max} - T_{ambient}$. The salient feature is the occurrence of a rapid decrease in retained strength around a critical temperature difference ΔT_c below which the original strength is retained. As the quench temperature is further

increased, the strength decreases but more gradually. For $\Delta T > \Delta T_c$, the cracks will grow and consume the strain energy of the system. Conversely, for $\Delta T \leq \Delta T_c$, the strain energy that develops in the system is insufficient to extend the cracks, which in turn implies that the strength should remain unchanged, as observed experimentally.

Billets (40 x 4 x 3mm) were heated in an electric furnace from 400 to 1200^{o}C with an interval of 200^{o}C and soaked for 30 minutes. Subsequently, heated bars were quenched in water at room temperature, kept for 10 minutes followed by sudden reheating at corresponding tested temperatures for 10 minutes. This cycle was repeated twice and the retained flexural strength was measured by Instron 4465. The span was maintained at 40 mm and the crosshead speed at 0.5 mm/min. Three samples were taken to determine the retained flexural strength at each test and the average values had been reported here.

4.7.6. Thermal Expansion Coefficient

High temperature characteristics of the sintered specimens approximately ~40nm in length were measured by Dilatometer (Netzsch DIL 402C). Thermal expansion coefficient and hysteresis characteristics were estimated through in-built software.

The linear change in dimension of the sample was evaluated as follows;

$$\% \text{ shrinkage / expansion} = \Delta L/L_0 \times 100$$

where ΔL = Shrinkage or expansion of the sample, L_0 = Initial length of the sample. In the dilatometer the specimen is kept in a specimen holder in the centre of the furnace. The linear dimensional change i.e. shrinkage or expansion of the specimen is transmitted through the push rod (pressed against the sample inside the furnace) to the measuring head. The inductive displacement transducer details the change in length and produces an analogue signal of 1 mm = 1V through a measuring amplifier. The digitally displayed signal is in analogue form on a recorder. Thermal expansion measurements were conducted in the temperature range from room temperature to 1450^{o}C at heating and cooling rate of 5^{o}C min^{-1} using high-grade quartz as reference.

CHAPTER 5

5.0 RESULTS AND DISCUSSION

5.1. Powder Synthesis:

Table 4.1 represents the typical composition of Al_2O_3-ZrO_2 gel precursors used in the present investigation. Al_2O_3-xZrO_2 (where x = 5, 7.5, 10, 15mol %) gel precursor powders were prepared by wet chemical route. The methodology was illustrated in Fig 4.1.1. The washed gel containing hydroxide of aluminum and zirconium were characterized through DTA/TGA, XRD and IR spectroscopy. Additionally, the high temperature phase transformation was characterized and analyzed through XRD and FTIR techniques. Finally, the particle characteristics of the synthesized powders were estimated through BET surface area analyzer, particle size analyzer and transmission electron microscopy. The TEM–EDS technique was used to determine the element analysis of synthesized powder.

5.1.1. Thermal Characteristics of Hydrogel

The Differential Thermal Analysis (DTA) results reveal that the crystallization temperature of mixture of aluminum and zirconium hydroxide varies with respect to zirconia content. The DTA – TGA (Thermo-Gravimetric Analysis) plot (Fig 5.1.1) of high zirconia content (A4Z) hydrogel shows a broad endothermic peak at 110^{o}C, a sharp exothermic peak at about 225^{o}C and another endothermic peak at 280^{o}C. At higher temperature, the DTA curve shows a small sharp exothermic peak at about 420^{o}C and also shows a sharp but small endothermic peak at about 480^{o}C. Finally, the DTA curve shows a small exothermic peak at about 1160^{0}C. The TGA curve of the gel shows a gradual weight loss of about 15% in the temperature range 25-210^{o}C and a sharp weight loss of about 18% in the temperature range 210-315^{o}C show a further weight loss of about 17% which takes place in three stages. The first stage of this weight loss is about 5% in the temperature range 315-320^{o}C, the second stage about 10% in the temperature range 320 – 455^{o}C and the final stage of weight loss is about 2.0% in the temperature range 455 – 545^{o}C.

The thermal behavior of the A4Z gel powder could be explained as follows: The gel powder contains disordered pseudoboehmite at room temperature having more than 15% excess water in its lattice[153]. The theoretical weight loss due to dehydroxylation of pseudoboehmite is about 13% for A4Z sample which matches well with the observed weight

loss. Thus the first endothermic peak and the associated weight loss correspond to the dehydroxylation of pseudoboehmite.

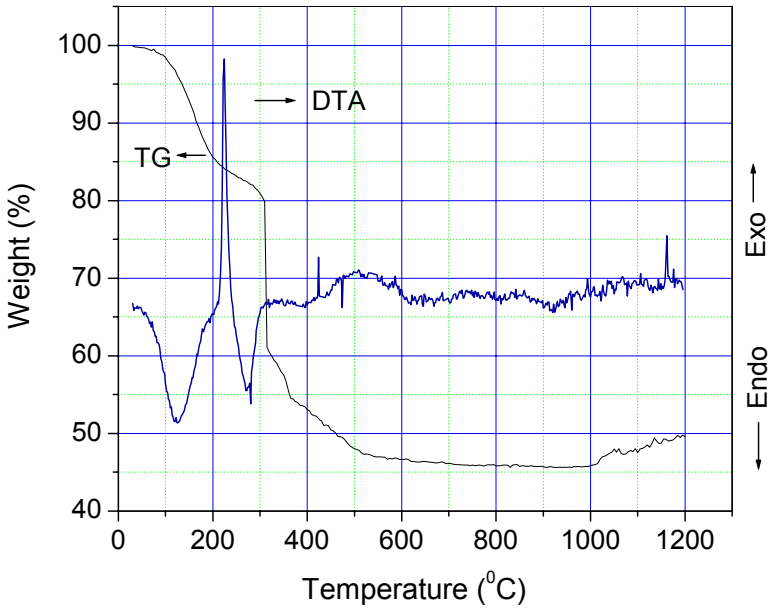

Fig.5.1.1. TG/DTA plot for Al_2O_3-15ZrO_2 precursor powder in air

The dehydroxylation of pseudoboehmite is associated with the crystallization of bayerite (β-Al_2O_3. 3H_2O). Thus the exothermic peak could be related to the crystallization of bayerite. The bayerite thus formed undergoes further dehydroxylation to boehmite (α-AlOOH) in the temperature range 280—308°C. The theoretical weight loss for this reaction is 19.61%. The observed weight loss 19% agrees well with this transformation. Subsequently, boehmite changes to γ-Al_2O_3 according to the reaction:

$$2AlO(OH) = Al_2O_3 + H_2O \text{……...(5.1.1)}$$

The theoretical weight loss is 15% whereas observed weight loss for A4Z is 12.75%. The weight loss is associated with one exothermic and one endothermic peak. The presence of these peaks could be explained as follows: AlO(OH) does not transform to γ–Al_2O_3 directly. It first transforms to an amorphous alumina on dehydroxylation which subsequently crystallizes to γ-Al_2O_3[24]. Thus the exothermic and endothermic peak in the temperature range 415-480°C corresponds to the conversion of dehydroxylated boehmite to γ-Al_2O_3 via the intermediate formation of amorphous alumina. Finally, the exothermic peak at 1160°C corresponds to crystallization of α-Al_2O_3. However, X-ray diffractograms of powders calcined for 2h at 1000°C show the presence of α-Al_2O_3. While X-ray pattern was recorded on samples that

were held for 2h at 1000°C, the DTA was done without any isothermal hold. Thus the isothermal hold at 1000°C has accelerated the transformation to α-Al_2O_3 at lower temperature. A similar change in the crystallization temperature of α-Al_2O_3 was also observed by the earlier researchers[154].

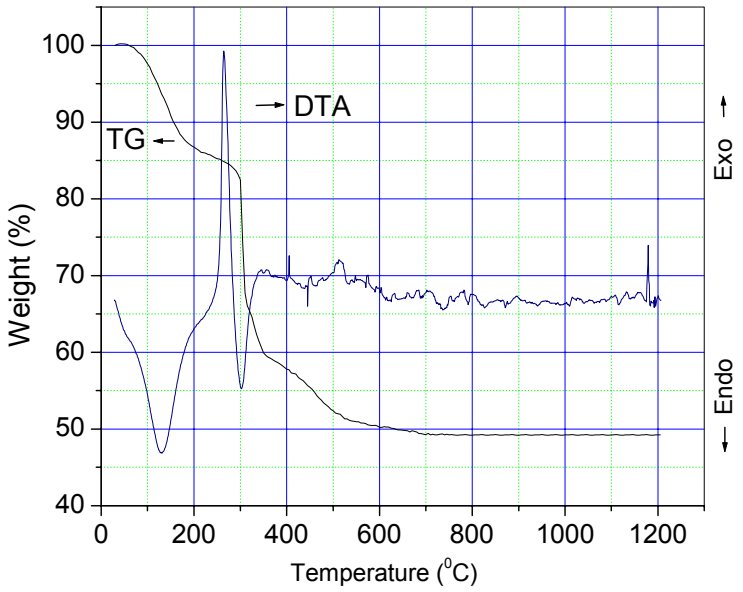

Fig.5.1.2. TG/DTA plot for the Al_2O_3-$5ZrO_2$ precursor powder in air

On the other hand, the transformation of $Zr(OH)_4$ to ZrO_2 follows the reaction:

$$Zr(OH)_4 = ZrO_{1.5}(OH) + 1.5H_2O \text{……..(5.1.2)}$$

$$ZrO_{1.5}(OH) = ZrO_2 + 0.5H_2O \text{…….(5.1.3)}$$

The theoretical weight loss for the dehydroxylation of $Zr(OH)_4$ and its crystallization to ZrO_2 following the above reaction sequence as equation 5.1.2 and 5.1.3 should be about 4%. The observed weight loss matches well with the theoretical value.

A similar trend of the DTA-TGA curve of the dried A1Z gel powder is also shown in Fig. 5.1.2. The weight loss associated with the dehydroxylation of pseudoboehmite of A1Z, A2Z, A3Z and A4Z precursors vary from 15 – 17%, however, 33-35% weight loss could be estimated for the formation of oxides of Al and Zr.

The small exothermic and endothermic peaks of A1Z precursor powder are shifted to 407°C and 455°C respectively, which are lower than A4Z precursor powder. The crystallization temperature of α – Al_2O_3 is also lower (1152°C) in comparison with A4Z (1160°C). From DTA analysis, it is clear that the formation of α - Al_2O_3 takes place through γ-Al_2O_3 formation from the transitional aluminas (Table 5.1.3). From the above DTA-TGA analysis it could be emphasized that the crystallization of alumina affected due to zirconia

content. This statement can be discussed as follows: Generally, the hydroxides of aluminum and its derivatives are dehydrated to form transitional aluminas with changes in pore structure to accommodate crystallization[155]. This transformation is possible since the transitional aluminas differ from each other only in the degree of ordering of the oxygen lattice. The formation of α - Al_2O_3 from transitional aluminas involves the rearrangement of the oxygen lattice from a more or less distorted cubic array to a hexagonal close packed structure. During this transformation process the cations progressively occupy the octahedral sites and there is an increasing ordering of the cation vacancies. As α - Al_2O_3 forms by a nucleation and growth process, spherical colonies of α - Al_2O_3 nucleate in a porous matrix of transitional aluminas and grow gradually via the coarsening process. Hence, the transitional alumina can accommodate more cation compared to α-Al_2O_3. Higher amounts of zirconia can be dissolved in transitional aluminas than in α-Al_2O_3 because of the cubic spinel structure with a considerable number of defects and disorder[156]. During the transformation of α - Al_2O_3, the zirconia comes out of the cubic lattice sites and enters the interstitial and vacant lattice sites causing expansion of the lattice along the a-axis. These zirconium ions selectively exert dragging force on the diffusion of aluminum ions and hence the transformation to α - Al_2O_3 occurs at higher temperatures in the presence of higher content of zirconia.

5.1.2. FTIR Analysis

The major peaks appearing in the FTIR spectra of alumina-zirconia hydroxide system could be related to the following[157]:

1) – OH stretching vibration of the surface bonded or adsorbed water
2) – OH bending vibration of the surface bonded or adsorbed water
3) – OH stretching vibration of structural water, corresponding to M-OH bonding
4) – OH bending vibration of structural water, corresponding to M-OH bonding
5) Al-O stretching vibration
6) Zr-O stretching vibration

The IR spectral frequency of uncalcined hydrogels and calcined powders of all the compositions are presented in Table 5.1.1 and the detail IR spectra of the precursor powders calcined at different temperatures have been shown in Fig. 5.1.4 to 5.1.7.

All gels and calcined samples exhibited -OH stretching vibration in the frequency range of 3136 to 3857cm^{-1}. The reduced reflectance and bond depth of the gel powder could be ascribed to the non-crystalline nature of the material[158]. The number of peaks for -OH

stretching vibration in the Al_2O_3-ZrO_2 powder increases with an increase in the ZrO_2 content. The increased IR interaction probably reflects a gradual change in the composition and heterogeneity in the bond as well as a switch over from a homogenous single phase structure to a homogenous two phase structure. The characteristic vibration depends on the attachment of –OH group. Recently, Chen et. al has observed that the predominant monomer cluster (pH range 7-10.5) is $[Zr(OH)_6]^{2-}$ (Fig. 5.1.3a), which preferentially produces tetragonal (t) precursor structure with slow alkali addition (Fig. 5.1.3b)[159]. Therefore, the bonding mechanisms of Zr-OH and its final phase content depends on bridging hydroxyl groups, monomer structure, polymerization kinetics and pH of the precursor solution.

The frequency of different vibrational modes of Al-OH and/or Zr-OH including the bending and stretching modes are altered due to change in the charge distribution among species. This altered frequency of vibration in turn causes a change in the electrical dipole moment of the original species.

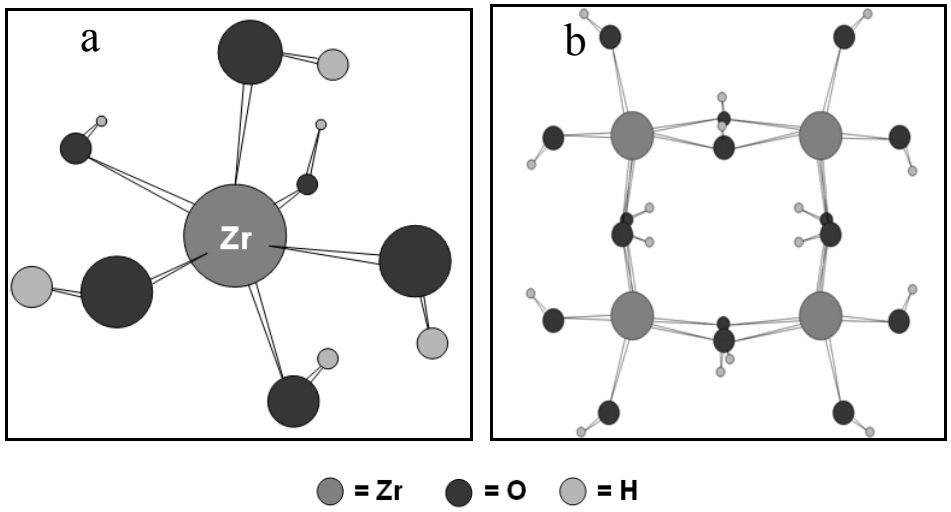

Fig.5.1.3. Cluster structure of $[Zr(OH)_6]^{2-}$ (a), ordered structure of polymerization precursor (b)

The charge distribution around each Al-OH and/or Zr-OH and associated vibration is influenced by the charge on its neighboring species. Hence, the continuum vibration of the matrix is responsible for the change in dipole moment and establishment of an electric field of the composite precursor powder. The increased cationic charge in the alumina-zirconia composite powder due to the introduction of Zr^{4+}, strongly interacts with the polar inner hydroxyl groups. This interaction probably results in the reduction of vibrational dipole moment in bending, thereby creating a greater force of attraction (antisymmetric coupling) on the stretching vibration.

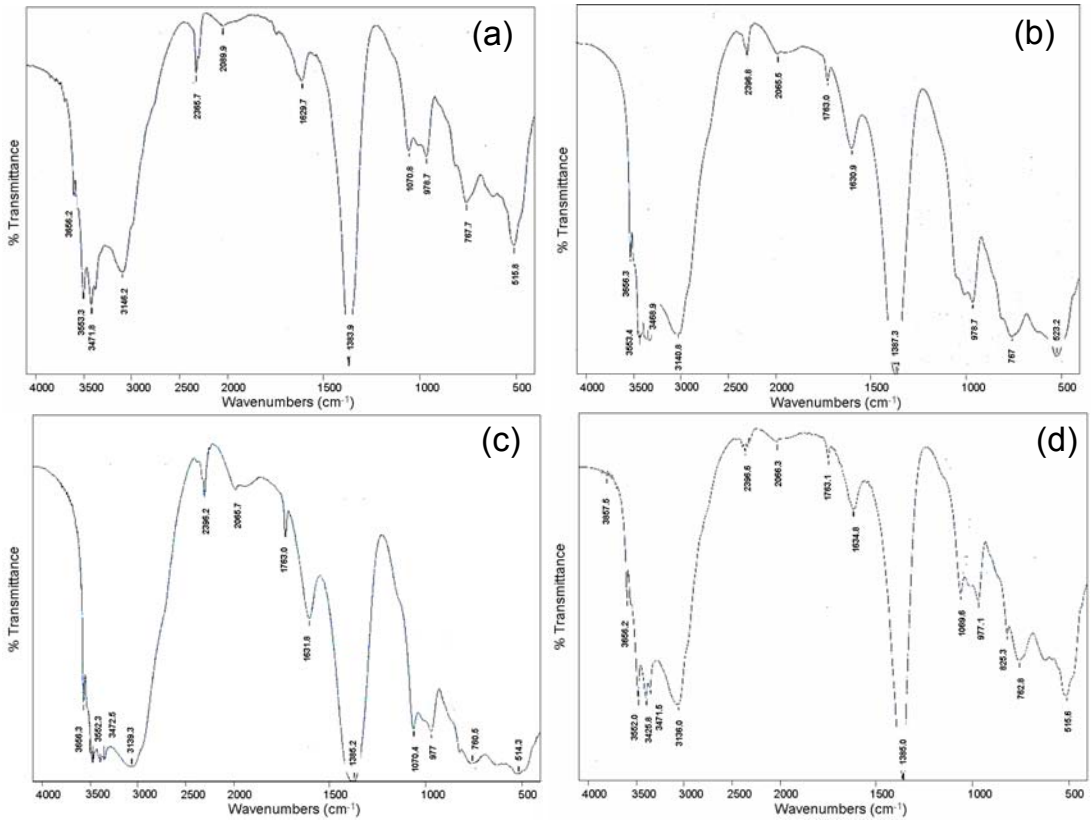

Fig.5.1.4. FTIR Analysis of different dried gel, where (a) Al_2O_3-5ZrO_2 (b) Al_2O_3-7.5ZrO_2 (c) Al_2O_3-10ZrO_2 and (d) Al_2O_3-15ZrO_2.

The stretching vibration for structural –OH and adsorbed water appear at wave number greater than 3000 cm^{-1} for all the alumina-zirconia (AZ) compositions. Four peaks are observed in the wave number range 3656, 3553, 3471 and 3146 cm^{-1} which account for –OH stretching. A careful observation of stretching frequencies reveal that an increase in ZrO_2 content in the batch causes a significant change in the –OH stretching pattern. In the A4Z sample two more additional peaks appear at 3857 and 3425 cm^{-1} (Fig 5.1.4d), which indicate the presence of more –OH in this batch. These two additional vibrations are probably due to -OH groups attached to the Zr^{+4}.

For all AZ samples the vibrations appearing in the range 2396 and 2065 cm^{-1} could be assigned to the coupling effect of stretching and bending vibrations of –OH groups. Although these two vibrations appear nearly at the same wave number in all the compositions, a slight shift in the peak position is noted for A1Z samples. Aluminum hydroxide is more hygroscopic compare to zirconium hydroxide, which assist to the formation of more –OH and attachment as $Al(OH)_x$ species and changes the vibration characteristics. The peaks that appear at 1764, 1634 and 1385 cm^{-1} are due to the bending vibration of Zr –OH groups. The peak positions

are more or less the same in all the samples. The peaks between 1070 and 760 cm^{-1} correspond to *Al-O* vibration[160].

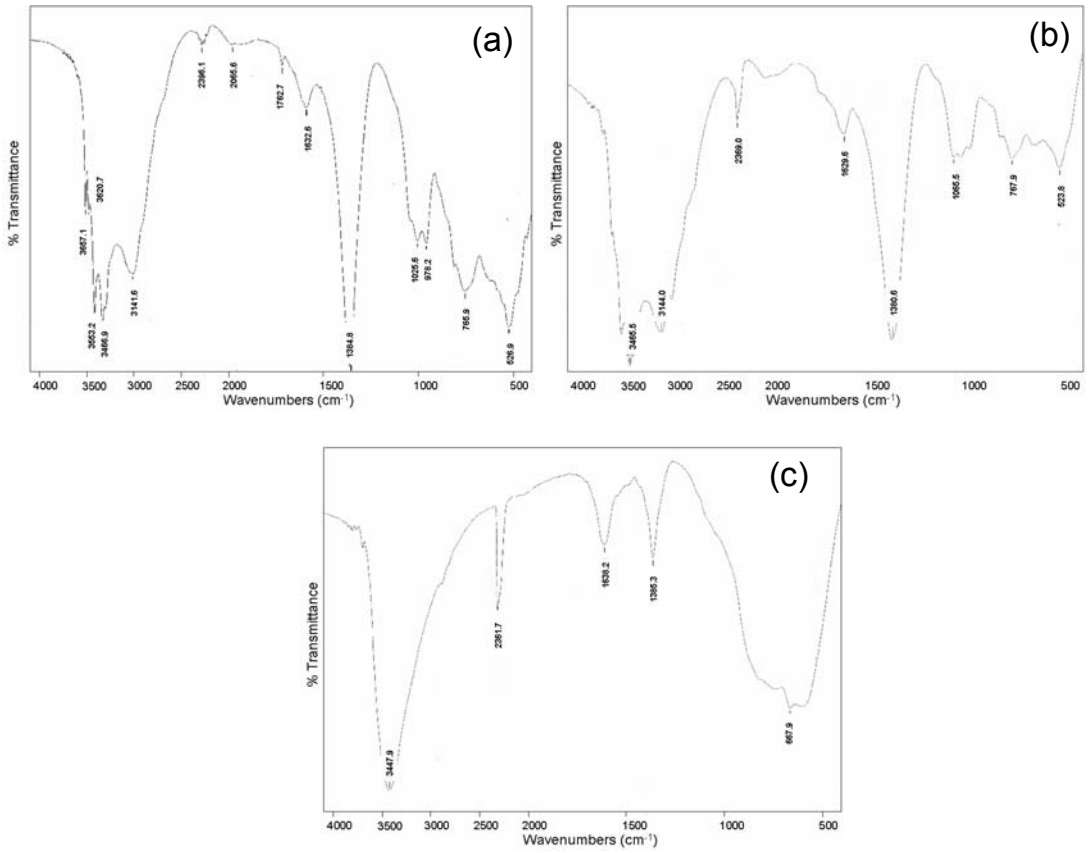

Fig.5.1.5. FTIR analysis of different powders calcined at 200^{0}C for 2hr, where (a) Al_2O_3-5ZrO_2 (b) Al_2O_3-10ZrO_2 and (c) Al_2O_3-15ZrO_2.

The strong absorption band of the latter one may be attributed to six-coordinated Al^{3+} ions. These O-H and Al-O vibrations are characteristics of pseudoboehmite. The absorption band at 1070cm^{-1} is due to the presence of alumina gel. The above results conclude that alumina in this particular alumina-zirconia system is present as an intermediate bayerite. Both the constituents of the hydrogels exhibit the -OH stretching and bending vibrations. The absorption bands at 514 to 523 cm^{-1} correspond to Zr-O vibrations.

A1Z samples calcined at 200^{o}C shows an additional peak at 3620.7cm^{-1} (Table 5.1.1). This is related to the activation of the structure by heating and consequent adsorption of water to the active surface. The bending vibration at 1762.7cm^{-1} shows an additional peak due to adsorbed water. The IR analysis of A3Z and A4Z samples shows the disappearance of peaks at 3656cm^{-1} (due to the stretching vibration of physically adsorbed –OH with Al^{+3}) and 3552

cm^{-1} (due to the stretching vibration of physically adsorbed –OH with Zr^{+4}) after calcination at 200°C. The disappearance of peaks corresponding to adsorbed water in A4Z sample could be related to the reduction in surface positive charge density of Al_2O_3-ZrO_2 system with the increase in ZrO_2 content. The –OH group bonded with Al^{+3} shows a peak at 3447.9 cm^{-1} with the corresponding bending vibrations at 1638.2 and 1385.3cm^{-1} (Fig. 5.1.5). Bending vibration and/or coupled vibration of –OH group attached with Zr^{+4} disappeared at this temperature.

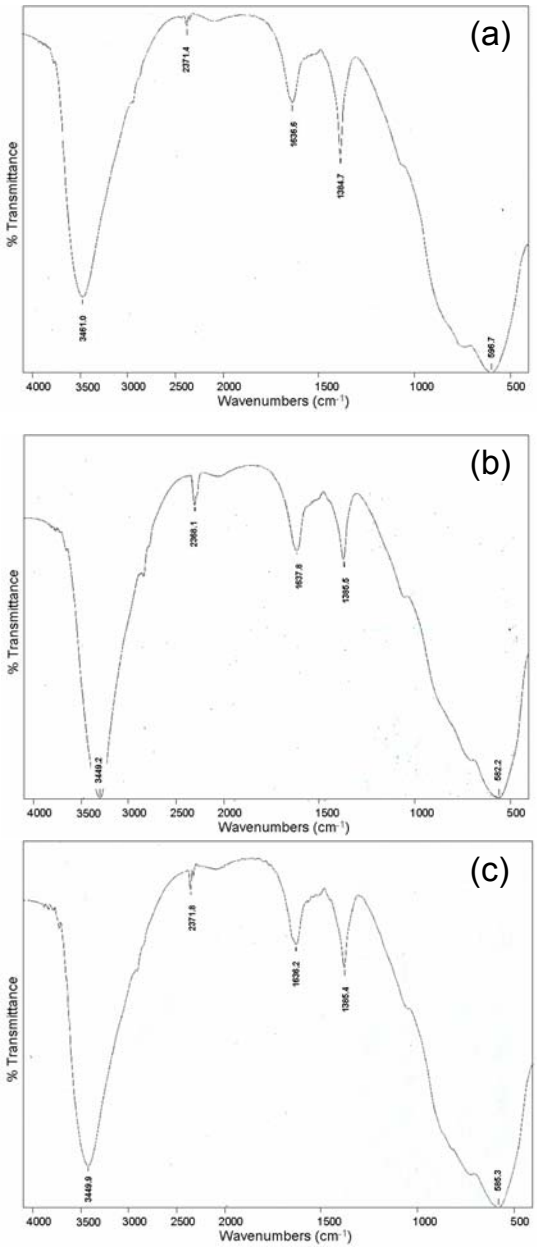

Fig.5.1.6. FTIR analysis of different powders calcined at 400°C for 2hr, where (a) Al_2O_3-$5ZrO_2$ (b) Al_2O_3-$7.5ZrO_2$ and (c) Al_2O_3-$10ZrO_2$.

Table 5.1.1. IR spectral frequency (cm^{-1}) of Al_2O_3-ZrO_2 systems with respect to temperature

Material	Dried Gel	200°C	400°C	1000°C
A1Z	3656.2	3657.1	3461	3484.3
	3553.3	3620.7		
	3471.8	3553.2		
	3146.2	3466.9		
		3141.6		
	2365.7	2396.1	2371.4	
	2089.9	2065.6		1643.7
	1762.0	1762.7	1636.6	1395.9
	1629.7	1632.6	1384.7	
	1383.9	1384.8		
	1070.8	1025.6		
	978.7	978.2		839.8
	767.7	765.9	596.7	537.4
	515.8	526.9		
A2Z	3656.3		3449.2	3484.3
	3553.3			
	3468.9			
	3140.8			
	2396.8		2368.1	
	2065.5			
	1763.0		1637.8	1642.3
	1630.9		1385.5	1425.3
	1387.3			
	978.7			846.2
	767.0		582.2	542.3
	523.2			
A3Z	3656.5	3465.5		3484.3
	3552.3	3144.0		
	3472.5			
	3139.3			
	2396.2	2369.0		
	2065.7			
	1763.0	1629.6		1641.2
	1631.8	1380.6		
	1385.2			
	1070.4	1065.5		832.8
	977.0			
	760.5	767.9		568.0
	514.3	523.8		
A4Z	3857.5	3447.9	3449.9	3450.8
	3656.4			
	3552.0			
	3471.5			
	3425.8			
	3136.0			
	2396.6	2361.7	2371.8	
	2066.3			
	1763.1	1638.2	1636.2	1629.5
	1634.8	1385.3	1385.4	
	1385.0			
	1069.6	667.9		828.0
	977.1			
	825.3			
	762.8		585.3	525.6
	515.6			

After calcination at 400^{0}C (Fig 5.1.6), for A1Z batch, all the peaks related to stretching vibration of free and bonded water disappear. Only one peak at 3461cm^{-1} still exists, which is related to the stretching vibration of -OH group attached with Al^{+3}. Bending vibration and/or coupled vibration of Al-OH group can only be observed in the spectrogram. On the lower frequency side a peak at 596.7cm^{-1} is observed which could be related to the Al-O vibration. Heating at 400^{o}C causes broadening of peaks in the lower frequency range (500-1000cm^{-1}) due to overlapping of Al-O and Zr-O infrared vibrations of transition alumina and zirconia phases. Thus individual peaks corresponding to Zr-O could not be detected in the temperature range 200- 400^{o}C. However, at higher temperature (1000^{o}C), peaks corresponding to Al-O and Zr-O could be clearly observed. Similar trend is also followed in A2Z, A3Z and A4Z samples.

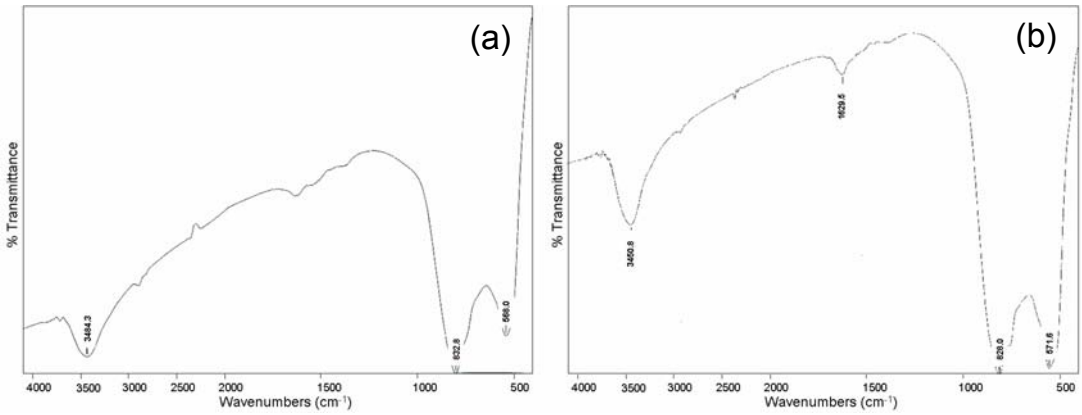

Fig.5.1.7. FTIR Analysis of different powders calcined at 1000^{0}C for 2hr, where (a) Al_2O_3-10ZrO_2 and (b) Al_2O_3-15ZrO_2.

IR spectra shows that a trace amount of –OH group still remains in the structure of ZrO_2 dispersed Al_2O_3 powder even after heating at 1000^{o}C (Fig 5.1.7). The reduced intensity of –OH absorption band could be due to the moisture absorption during testing. A3Z powder calcined at 1000^{o}C shows a peak at 3484.3 cm^{-1} corresponding to Al-OH stretching vibration. The stretching of crystalline Al–O and Zr–O bonds show absorption bands at lower frequencies of 828.0cm^{-1} and 525.6cm^{-1} respectively for A4Z samples [161].

5.1.3. TEM Analysis

The particle size and morphology of synthesized precursor powder could be directly determined from a transmission electron micrograph. However, the determination of particle size from TEM micrographs has few limitations. The accuracy of the average particle size determined from TEM image is limited by other images collected, the number of particle

observed in each image, and whether the small section examined is representative of the whole sample. However, a number of micrographs were taken for different dried gels and calcined powders. For a number of samples bright-field and dark-field images were compared, and the average 'particle size' identified in each images was approximately same. All micrographs shown here are 'bright-field' images.

TEM micrograph of the A1Z dried-gel is shown in Fig 5.1.8a. It reveals that the light gray shaded particles are less dense, which is presumably amorphous in nature. The comparative denser particle ranges between 22 and 68nm, with an average size of approximately 42nm, and no clear facets are observed. The volume fraction of the amorphous component could possibly exceed 50%, although it is difficult to estimate the mass fraction from the micrographs. Many 'low-density' features, approximately 5 to 10nm in size, are also observed.

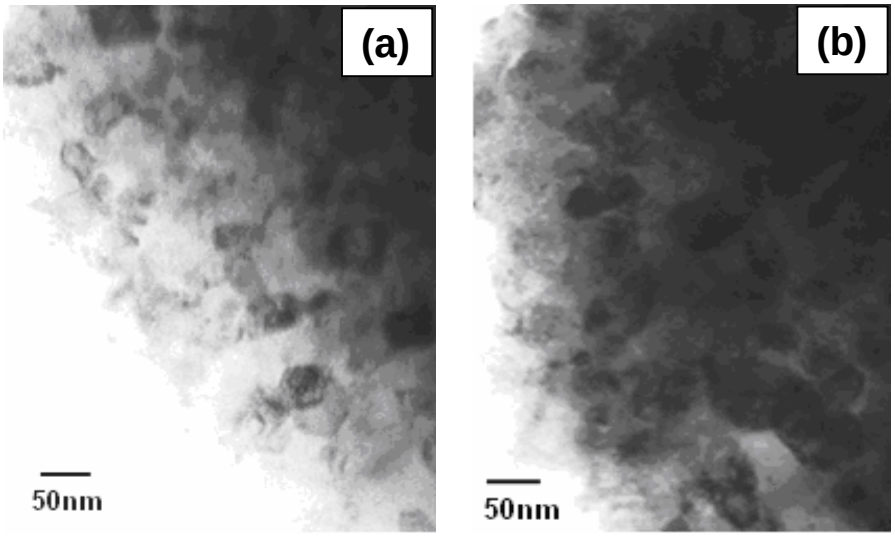

Fig.5.1.8. TEM image of dried gel (a) Al_2O_3-5ZrO_2 and (b) Al_2O_3-15ZrO_2.

The presence of the amorphous component does not greatly affect the diffraction pattern with variation of ZrO_2 content; however, it does affect the FTIR significantly, as discussed in section 5.1.2. Fig 5.1.8b represents the average particle size of A4Z slightly larger than A1Z dried gel, which is approximately 45nm. These micrographs indicate the formation of amorphous material before the crystallization of gel. Discrete tiny pores also can be observed within the amorphous matrix and denser particles. In practice, there is no definite shape and size for the as–formed amorphous gels or pores. Initially pores are most likely formed through entrapment of excess ammonia in the form of bubbles (pH = 8.7) in the gel.

The size, number, shape and location of the pores change with the thermal history of the precursor material[162]. Hence, the pore size would be expected to decrease with heating, as they would create vacancies into the surrounding crystal and eventually disappear altogether. Simultaneously, the particles heat-treated at different temperatures show different morphology; and smooth, distinct and faceted particles are observed at higher calcination temperatures.

Fig. 5.1.9 to Fig 5.1.10 show different morphology as the calcination temperature is increased and continuously changes up to 1000^{o}C. The fraction of amorphous material decreases for both of the A1Z and A4Z precursors, and the sample heated to 400^{o}C appears to be nearly crystalline comparison with dried-gel (Fig. 5.1.9).

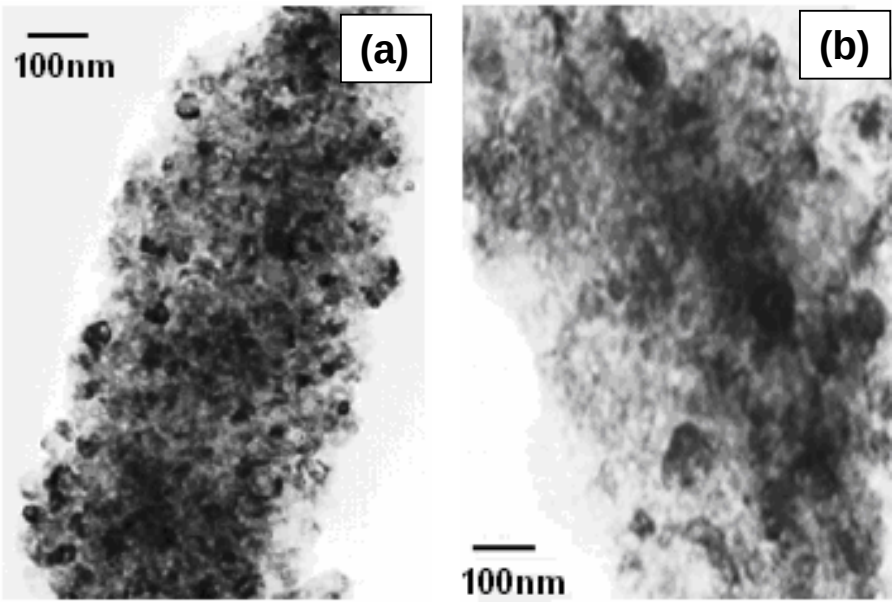

Fig.5.1.9. TEM image of powders calcined at 400^{0}C for 2hr, where (a) Al_2O_3-5ZrO_2 and (b) Al_2O_3-15ZrO_2.

The angularity and faceting of the crystal also increases as diffusion within each allows low-index planes to predominate on the surface. However, the observed average particle size does not change significantly, remaining close to 45nm. TEM indicates that over 65% of the synthesized particles have distinctiveness. Micrographs indicate that particles are frequently overlapping on the image, giving some particles a 'sponge-like' appearance. It is difficult to predict whether particles touch each other or overlap on surfaces. No pores are observed for the samples calcined at 400^{o}C and faceting other particles begins. Most of the crystal facets and crystal growth occurs once the calcination temperature reaches 800^{o}C and

particle size increases ~100nm. The micrograph of a sample (Fig. 5.1.10) at 1000°C heated for 2h shows the moderate particle growth with meso-pore and nearly all particles are spherical in nature. The TEM micrographs A1Z powder calcined at 1000^{0}C for 2h exhibit fine sized particles (light shade) within the range of 18-185nm. The micrograph of powder calcined at 1000°C for 2h exhibits a number of dark patches (>200nm), which may indicate the partial agglomerated particles cluster, probably resulted due to sample preparation. The average particle size of A1Z and A4Z in the precursor is about 90 and 120nm respectively. The specific surface area of the A4Z powder is determined by the BET surface area analysis and is calculated about ~130m^2/gm.

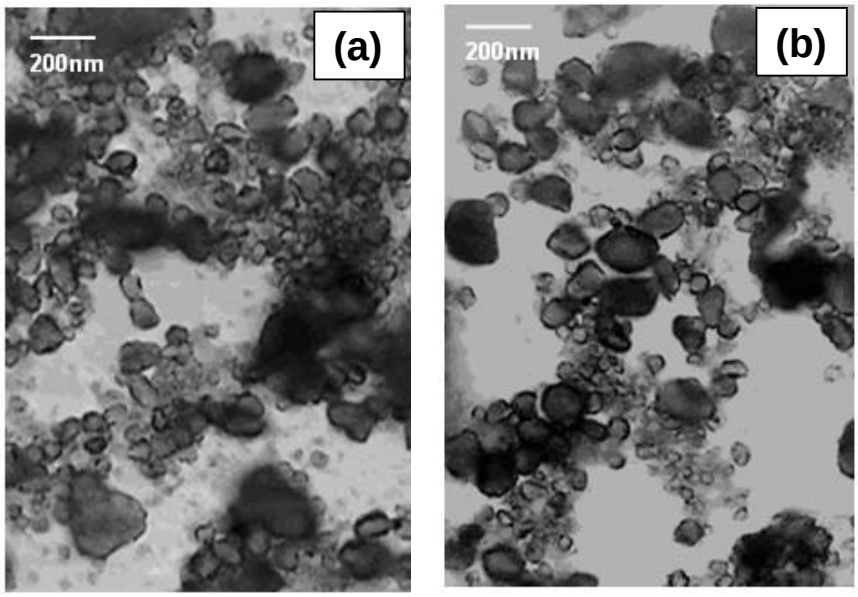

Fig.5.1.10. TEM image of powders calcined at 1000^{0}C for 2hr, where (a) Al_2O_3-5ZrO_2 and (b) Al_2O_3-15ZrO_2

The average range of particle sizes and morphology observations for typical A4Z precursor are summarized in Table 5.1.2. At 1000°C, the monoclinc phase can be observed with a substantial amount of tetragonal phase (Fig. 5.1.14). Generally, these studies have been dealing with the hypothesis that an increase in crystal size leads to the tetragonal-to-monoclinic transformation, that the free energy released by the t→m transformation promotes crystal growth. There are some suggestions that metastable-to-stable transformation strongly promotes crystal growth[163]. However, recent works claim that there is little evidence for such transformation having any effect on microstructural development[164]. It is also reported that the structure changes due to the heat treatment is associated with the activation of mass-transport mechanisms above 900°C.

Table 5.1.2. Average particle sizes and morphology of Al_2O_3-15ZrO_2 precursor as a function of temperature

Treatment Temperature (^{0}C)	Particle Size range (nm)	Average Particle Size (nm)	Morphology comments
Dried Gel	12-68	42	Crystals in an amorphous matrix
200^{0}C	15-85	51	Increased crystallinity
400^{0}C	10-98	58	Increased crystallinity & faceting
600^{0}C	15-106	64	Increased crystallinity & faceting
800^{0}C	10-140	76	Fully crystalline, faceted crystals
1000^{0}C	15-216	121	Fully crystalline, faceted crystals

The TEM-EDS analysis was carried out for A3Z precursor powder calcined at 1000^{o}C for 2h (Fig. 5.1.11). The morphology of alumina-zirconia powder reveals that particles are mostly round shaped with dimensions in the range of 26-192nm with a few irregular particles. Most of the particles are free from agglomeration, which is a well indication of flowablility.

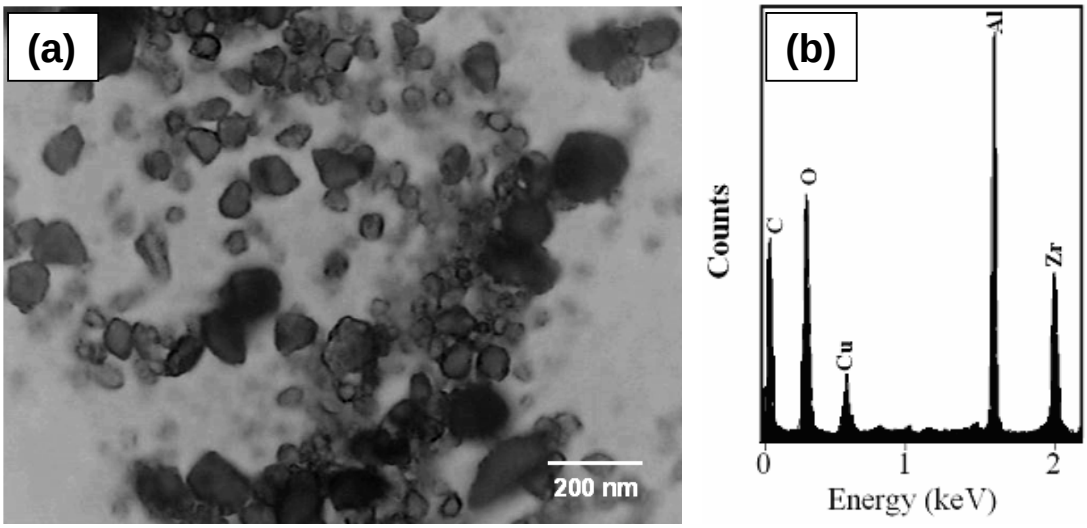

Fig.5.1.11. TEM image of Al_2O_3-10ZrO_2 powder calcined at 1000^{o}C for 2hr (a) and TEM-EDS analysis of the same particles (b)

The smallest particle size of the calcined powders is ~30nm as determined by TEM study. TEM-EDS trace from one of the small clusters of particles is shown in Fig 5.1.11b. This trace shows strong peaks for Al, Zr and O, which confirm the composition of Al_2O_3-ZrO_2 powder. The peaks for Cu and C arise from scattering of X-rays from the copper grid and the carbon film, respectively.

5.1.4. XRD Analysis

In all the systems where chemical reactions or crystallization operate through the solid phase, mass transport takes place through apparently regular crystal lattices. The particular mineral phases and degree of crystallinity of the solid phases are important controlling parameters in most solid state mechanisms. X-ray diffraction analysis was carried out in order to ascertain the crystalline nature of synthesized gels and calcined zirconia dispersed alumina precursor powders. A detail XRD analysis of higher zirconia content (A4Z) precursor powder are reported and analyzed with respect to different temperatures.

Table 5.1.3. Phase analysis of Al_2O_3-15ZrO_2 at different temperature

Drying/Calcination Temperature of Gel	Phase Content
70^0C	SB
200^0C	BH, B
400^0C	GA
600^0C	GA
800^0C	TZ, GA
900^0C	TZ, DA, TA, AA
1000^0C	MZ, TZ, DA, TA, AA
1100^0C	MZ, TZ, DA, TA, AA
1200^0C	MZ, TZ, DA, TA, AA
1300^0C	MZ, TZ, AA
1400^0C	MZ, TZ, AA

AA = α-Al_2O_3, B = Bayerite, BH = Bohemite, DA = δ-Al_2O_3, GA = γ-Al_2O_3 , MZ = Monoclinic Zirconia, SB = Pseudo Bohemite, TA = θ-Al_2O_3, TZ = Tetragonal Zirconia

A sequence calcination upto 1400^{o}C for 2h and systematic XRD analysis of zirconia dispersed alumina hydrogel (Al_2O_3-xZrO_2, where x = 5, 7.5, 10 and 15 mol%) were carried out. A series of XRD phase investigation of the high zirconia content (A4Z) dried gel and calcined powders are listed in Table 5.1.3. The careful observation from the Table 5.1.3 emphasizes that phase transformation from pseudoboehmite to α-Al_2O_3 and zirconium hydroxide to zirconia formation takes place as reported by earlier researchers[156,165]. However, the variation of sequence of transformation of aluminum hydroxide and transformation temperature in the present study can be observed because of the presence of the zirconia content as foreign material and crystallite particle size.

Fig 5.1.12 reveals the XRD pattern of the as-dried gel, which exhibits the sharp peak of bayerite and amorphous ZrO_2 only. The broad peak of bayerite indicates the presence of fine crystallites (crystallite size 5-20nm). The FTIR studies of hydrogel are also supporting the presence of intermediate boehmite as well as the presence of Zr–O bond of non crystalline zirconia (Fig. 5.1.4d). The XRD of hydrogel calcined at 200°C for 2h shows the presence of both bayerite ($Al(OH)_3$) and boehmite (Al(O)OH) (Fig.5.1.13). The boehmite crystallizes from bayerite on heating according to the following reaction;

$$Al(OH)_3 = Al(O)OH + H_2O \text{…….(5.1.4)}$$

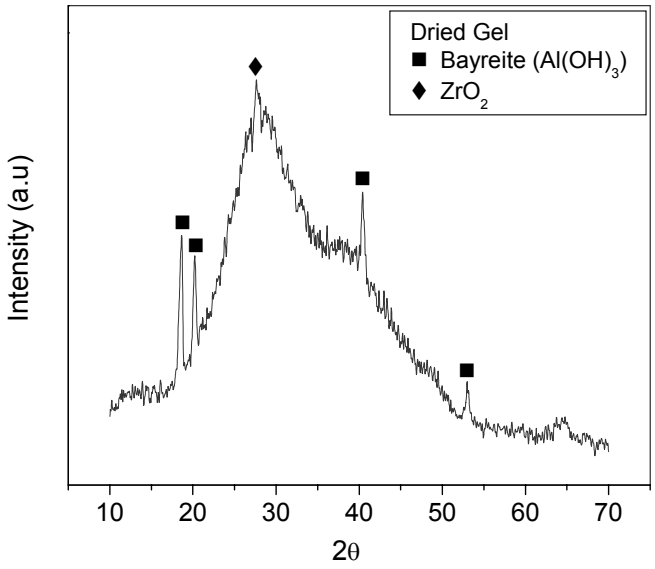

Fig.5.1.12. Phase analysis of Al_2O_3-15ZrO_2 dried gel by XRD

The IR analysis reports that the excess amount of water molecule has been removed at 400°C and produce Al-O-OH base compound. However, there is no evidence of Zr-O bond. As shown in Table 5.1.3, calcination temperature above 600°C, the tetragonal zirconia gradually crystallizes in very small crystallite size. The diffraction peak profile of the product heated to 600°C is very asymmetric, attributable to inadequate crystallization. As temperature increases, the peak became more symmetric and narrower. Crystallite size is estimated to be less than 10 nm, even for the sample heated to 900°C. Crystallite was improved significantly at this temperature, and monoclinic ZrO_2 appeared at 1000°C. Using the strongest diffraction line ($\bar{1}11$), the crystallite size was estimated to be 22nm according to Scherrer's equation, whereas, the crystallite size of the dried gel varies between 5 to 20nm.

Fig 5.1.14 reveals that the calcination at 1000°C induces further phase transformation as well as crystallization of zirconia from amorphous zirconium hydroxide. At 1000°C, the

m-ZrO_2, t-ZrO_2, δ-Al_2O_3, θ-Al_2O_3 and α-Al_2O_3 phases could be identified. The phase transformation of A4Z precursor from bayerite to α-Al_2O_3 is well agreed with earlier studies.

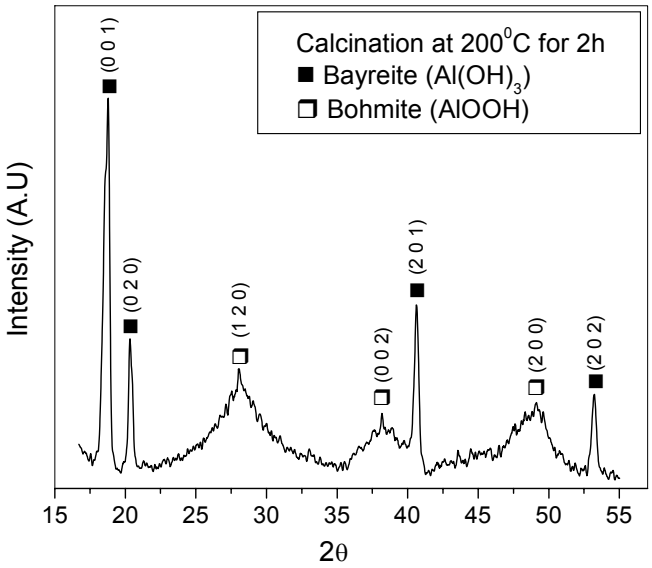

Fig 5.1.13. Phase analysis of Al_2O_3-15ZrO_2 powder calcined at 200^{0}C for 2h

Around 24% reduction of specific volume could be detected during the phase transformation of boehmite (0.332cc/gm) to α-Al_2O_3 (0.251cc/g), which also presumably affects the formation of intraparticle porosity in the precursor. The phase transformation temperature strictly depends on the particle size of the precursor, which may vary, with respect to different processing phenomenon.

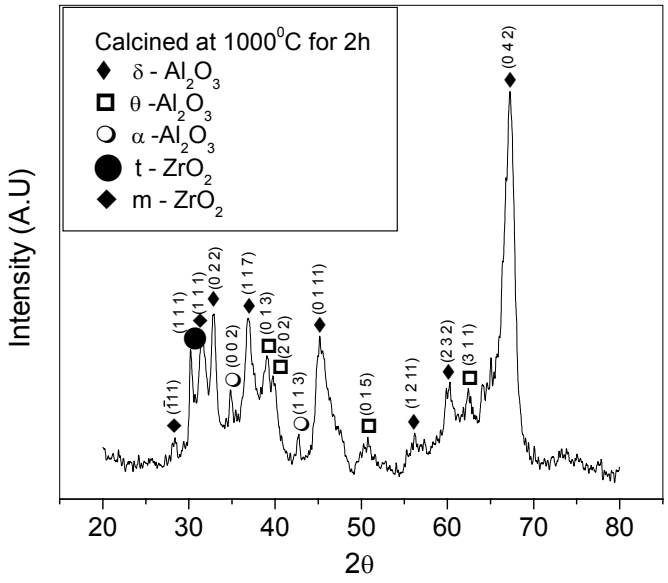

Fig 5.1.14. Phase analysis of Al_2O_3-15ZrO_2 powder calcined at 1000^{0}C for 2h

This small particle size or high specific surface area provokes the lower crystallization temperature. Smaller crystallite size could be detected from XRD analysis. The broadening of peaks in XRD patterns confirm that the average crystallite size is in nanometer range. However, TEM analysis indicates the particle size of the calcined powder at 1000^{o}C for 2h is in the range of 35-215nm.

The compacts were prepared from A1Z, A2Z, A3Z and A4Z powders calcined at 1000^{o}C for 2h. These precursor powders has common α-Al_2O_3 phase, however, the highest density cannot be achieved at 1550^{o}C for 3h even with 15mol% zirconia. Hence, the presence of α-Al_2O_3 in the compact does not have significant influence on the densification behavior. Nevertheless, the lower in sintered density above 1450^{o}C is due to the growth of grains with irregularly shaped porous structure. It is observed from Table 5.1.3 that the powder calcined at 1000^{o}C contains transitional phases of alumina. The development of microstructure with phase transformation is an important sintering step for the densification of transitional alumina-containing composites. This partial transformed precursor is assisting to monitoring the low temperature sintering with minimum coarsening, which is presumably due to high reactivity and shorter diffusion length with high surface curvature. In addition, the pore structure also plays a vital role during sintering.

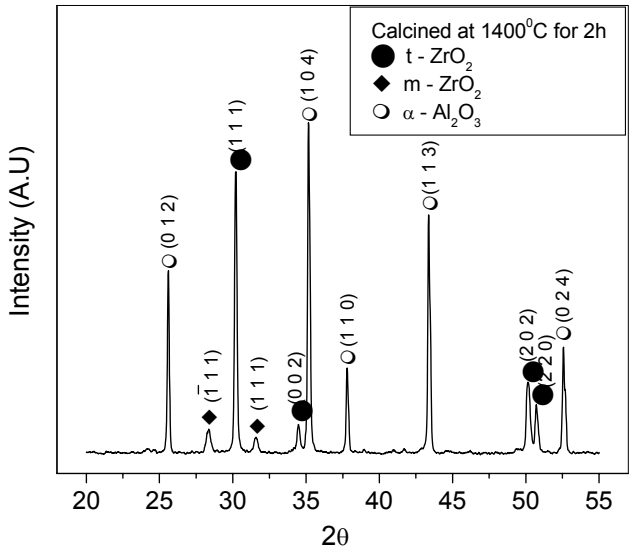

Fig 5.1.15. Phase analysis of Al_2O_3-15ZrO_2 powder calcined at 1400^{0}C for 2h.

To achieve the maximum post-sintering density of green compact, the alumina/zirconia hydrogel powder was calcined at 1000^{o}C for 2h. This optimum calcination temperature can also avoid the grain coarsening effect of sintered specimens. Hori et al.[16] also reported an optimal calcination temperature between 800 and 1000^{o}C. The ZTA specimen

prepared by them through the CVD method yielded very high density. Balasubramanian et al.[134] have reported that the precursors calcined at 950^{0}C for 3h show better densification behavior. However, only 90% of theoretical density has been obtained, when the powder compact has been sintered at 1630^{o}C for 3h.

Usually α–Al_2O_3 completely crystallizes around 1200^{o}C, however, in the present study the lower crystallization temperature of α–Al_2O_3 could be related to the fine crystallite size and higher specific surface area. Fig. 5.1.15 reveals the major phases of A4Z are t-ZrO_2 and α-Al_2O_3 present along with a small amount of m-ZrO_2 at 1400^{o}C, however, phase transformation was completed at 1300^{o}C. The increase in m-ZrO_2 content at 1400^{o}C results from an increase in the grain size of zirconia, which induces partial t-m transformation during cooling. Fig 5.1.16 presents the composite peak profiles of α–Al_2O_3 and m-ZrO_2 after the isothermal treatment (1400^{o}C/2h) for the four powders. The peak positions of precursor powder of Al_2O_3-xZrO_2 (x =5, 7.5, 10 and 15mol %) were determined by the FWHM (full width of half-maximum) middle point method [149]. Fig 5.16a reveals that the peak intensity has no change with respect to zirconia content. However, Fig 5.16b reveals considerable peak intensity of m-ZrO_2 reduction for lower content of zirconia, which indicates lower percentage of monoclinic phase formation.

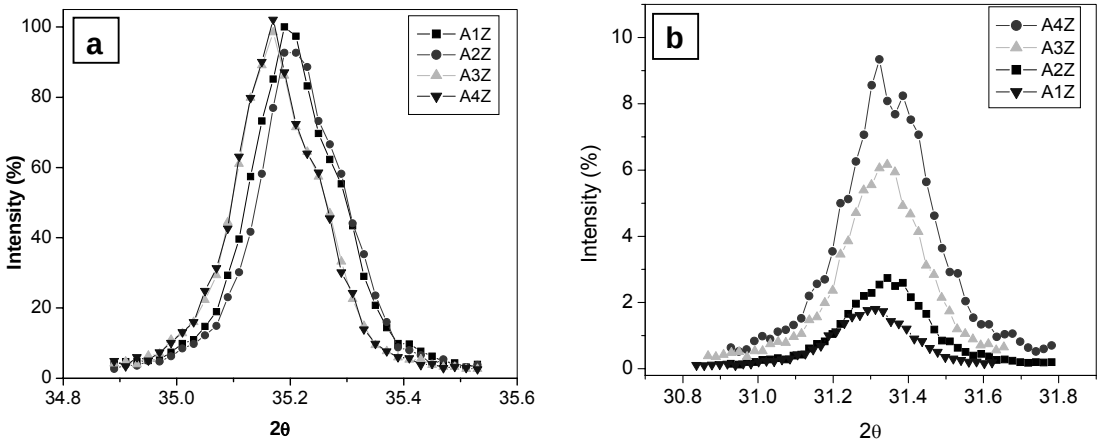

Fig.5.1.16. A composite plot of XRD spectra obtained from Al_2O_3-xZrO_2 powder (where x = 5, 7.5, 10 and 15 mol%) calcined at 1400^{0}C for 2h. Peak intensity of α–Al_2O_3 with respect to zirconia content (a) and Peak intensity of m–ZrO_2 (111) with respect to zirconia content (b).

From XRD analysis, the crystallite size of m-ZrO_2 of A3Z and A4Z specimens have been calculated using the strongest diffraction line (111), the crystallite size is estimated according to Scherrer's equation and plotted in Fig. 5.1.17. Up to 1400^{o}C, XRD analysis could not detect any m-ZrO_2 phase below 10mol% ZrO_2 addition. The crystallite size

gradually increases with increasing zirconia content as well as temperature. At 1000°C, the lowest crystallite size (20nm) was obtained for 10mol% zirconia content precursor powder and this was increased up to 27nm for A4Z. A similar trend can also be observed for 1200°C and 1400°C temperature.

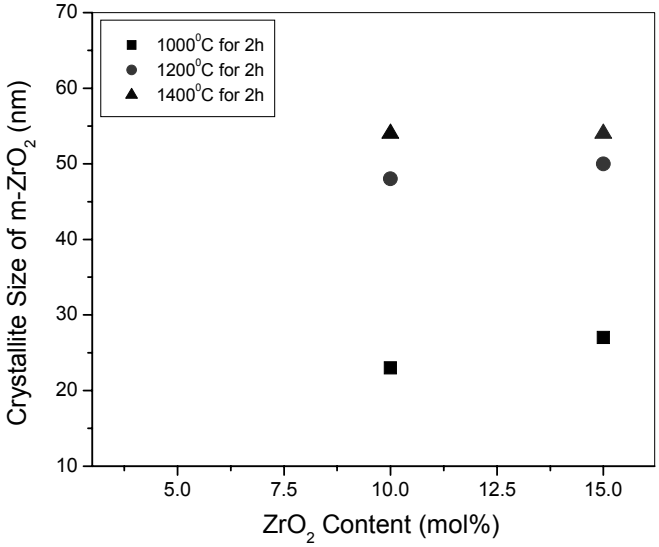

Fig 5.1.17. Average crystallite size of m-ZrO_2 obtained from Al_2O_3-xZrO_2 (where x = 10 and 15 mol%) at different temperature with 2h holding time.

5.1.5. Particle Size and Surface Area Analysis

Particle size distribution is a very critical and sensitive issue for green body formation through uniaxial cold pressing process. A mixture of different particle size is beneficial to achieve better densification, where sufficient fine particles are present to fill in the interstices to reach high green density compact.

Fig 5.1.18 reveals that the particle size of dried gel is smaller with comparison to calcined powder. The cumulative statistics of particle size distribution of calcined (1000°C for 2hr), as shown in Table 5.1.4 for as produced powders, are represented as D_{10}, D_{25}, D_{50}, D_{75} and D_{90} corresponding to the particle sizes below 10%, 25%, 50%, 75% and 90% of the total volume of particles analyzed, respectively. The ultra-fine powders could be synthesized, which is resembled with the TEM analysis.

The particle size analysis (Fig. 5.1.18) of the calcined powder also shows that the particles have a bimodal size distribution. The finer particle (≤20nm) represents the unagglomerated particles, while the larger size particle (~200nm) represents the agglomerate size. Table 5.1.5 represents the average particle size as determined in the present investigation and it increases gradually with increasing zirconia content. During solid state sintering,

surface energy is the main driving force for mass transport. Very fine precursor powders associated with high specific surface area provide activation energy for the sintering.

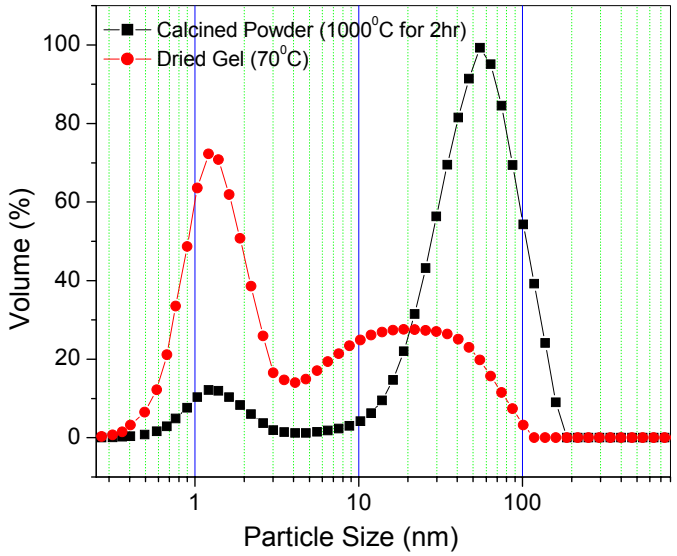

Fig 5.1.18. Particle size distribution of Al_2O_3 -15ZrO_2 dried gel and calcined powder

Table 5.1.4: Particle size analysis for sol-gel synthesized Al_2O_3-15ZrO_2 powders by laser diffraction method

%<		D_{10}	D_{25}	D_{50}	D_{75}	D_{90}	Mean
Volume statistics	Size (μm)	0.017	0.045	0.11	0.175	0.229	0.127

Table 5.1.5. Particle size and specific surface area of synthesized powders calcined at 1000°C for 2h powders

Identification	Average Particle Size (nm)	Surface Area (m^2/g)
A1Z	95	150
A2Z	105	144
A3Z	110	136
A4Z	125	130

From XRD analysis it is revealed that the monoclinic phase gradually increases with increasing zirconia content. The tetragonal-to-monoclinic transformation releases the free energy which promotes the crystal growth and increase the particle size. Simultaneously, the

surface area gradually reduces with increasing particles size. The surface area of A4Z data could be utilized to indirectly determine the particle size of the powder using the equation[166] :

$$D = 6/\rho S \text{……..} 5.1.5$$

where D is the particle size, ρ is the theoretical density of the powder and S is the specific area. Assuming the particles to be spherical in nature and the theoretical density of A4Z to be 4.28 gm/cc the calculated particle size was found to be ~11nm. Thus the calculated particle size agrees well with the particle size measured from TEM photograph.

5. 2. Densification

The powder synthesis methodology and their characterization have been analyzed and explained in section 5.1. The synthesized powders of each batch were thoroughly mixed with its corresponding uncalcined dried precursor (5wt%) as additive, and processed according to Fig 4.2. The batch composition of green specimens is summarized in Table 5.2.1. Note the batch identification of green specimens is different compared to powder identification.

Table 5.2.1. Batch composition of green specimens

Identification	Calcined Powder (1000^0C/2h)	Uncalcined Dried Gel (Additive)
A1ZB	95 % of A1Z	5% of A1Z
A2ZB	95% of A2Z	5% of A2Z
A3ZB	95% of A3Z	5% of A3Z
A4ZB	95% of A4Z	5% of A4Z

Prior to sintering, dilatometer measurements were made on pressed compacts prepared through uniaxial pressing followed by cold isostatic pressing. In this experiment, a low green density (1.63gm/cc) could be observed during uniaxial pressing (at 250MPa), which is because of meso-porosity and high specific surface area of synthesized powders. However, an average green density (1.85gm/cc) can be achieved after cold isostatic pressing (300MPa) of uniaxial pressed green compacts. Previous literature[131] results revealed that high surface area of powder hinders the high green density of uniaxial pressed specimens and it varies between 1.5-2 gm/cc., however, the addition of small amount of uncalcined powder (5wt%) have an influence during consolidation.

Sintering studies of the green compacts were carried out in both the muffle furnace as well as dilatometer in ambient condition. Dilatometric studies of A1ZB, A2ZB, A3ZB and A4ZB up to 1450^oC are shown in the Fig. 5.2.1. The sintering was carried out without any isothermal treatment with an initial heating rate of 10^0C/min up to 1000^oC and at the reduced rate of 5^0C/min there after. The small initial shrinkage curve up to 100^oC of the compacts during sintering is responsible for the expulsion of the residual water from the uncalcined

5wt% dried gel (added as additive). The densification starts at around 1000°C for A1ZB, whereas, this starting temperature was slightly higher for A4ZB. For the four tested compositions, shrinkage due to the monoclinic → tetragonal zirconia transformation was observed [167]. The final transformation temperature (A_f) is in the same range for the four materials, whereas the starting inverse transformation (t → m) temperature (M_s) decreases when the zirconia content decreases because of the grain size reduction[168]. Beyond 1200°C, the slope has been changed due to completion of α-Al_2O_3. Pores are also eliminated with an achievement of 65% of the theoretical density of that particular composition. However, the rate of shrinkage is the highest within the m-ZrO_2 to t-ZrO_2 transformation temperature i.e 970°C-1170°C. The behavior of shrinkage curve quite resembles with nanocrystalline ZrO_2 rather than coarse-grained ZrO_2[102]. The densification data obtained from the dilatometer experiment reveals that the achieved density is ~65% of theoretical density at 1450°C, which is independent of ZrO_2 content. However, the shrinkage and densities are almost identical at 1450°C for all the compositions. The present results exhibit the sintering without sintering additive and isothermal treatment is mainly attributed to high surface area of starting powders.

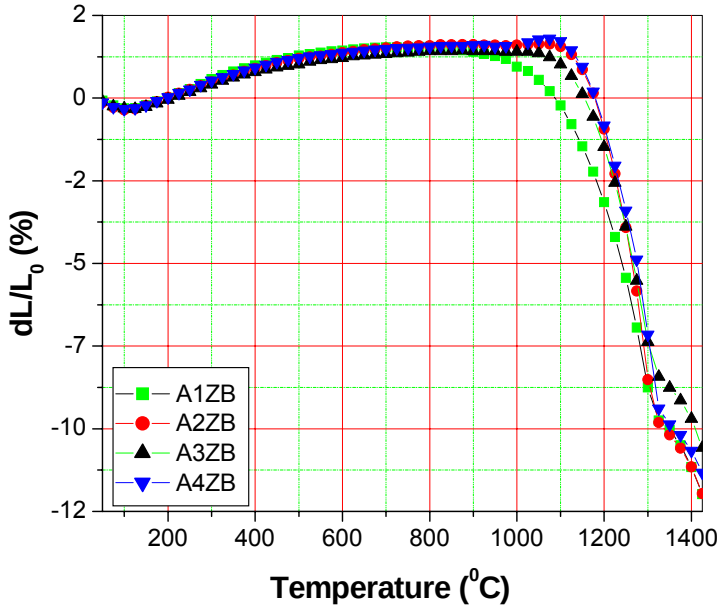

Fig. 5.2.1. Dilatometric study of ZTA composites at 1450°C

The powder compacts were sintered at 1450 to 1600°C with an interval of 50°C for different dwell time (2h, 3h and 4h). The bulk density was measured through Archemedis principle. The details of the bulk density and apparent porosity with 2h and 3h holding are represented in Fig 5.2.2 to Fig 5.2.3. As shown in Fig 5.2.2a and Fig 5.2.2b, the firing temperature at a

particular holding period had a considerable effect on the bulk density of A1ZB, A2ZB, A3ZB and A4ZB; however, it does not significantly changes with respect to zirconia content.

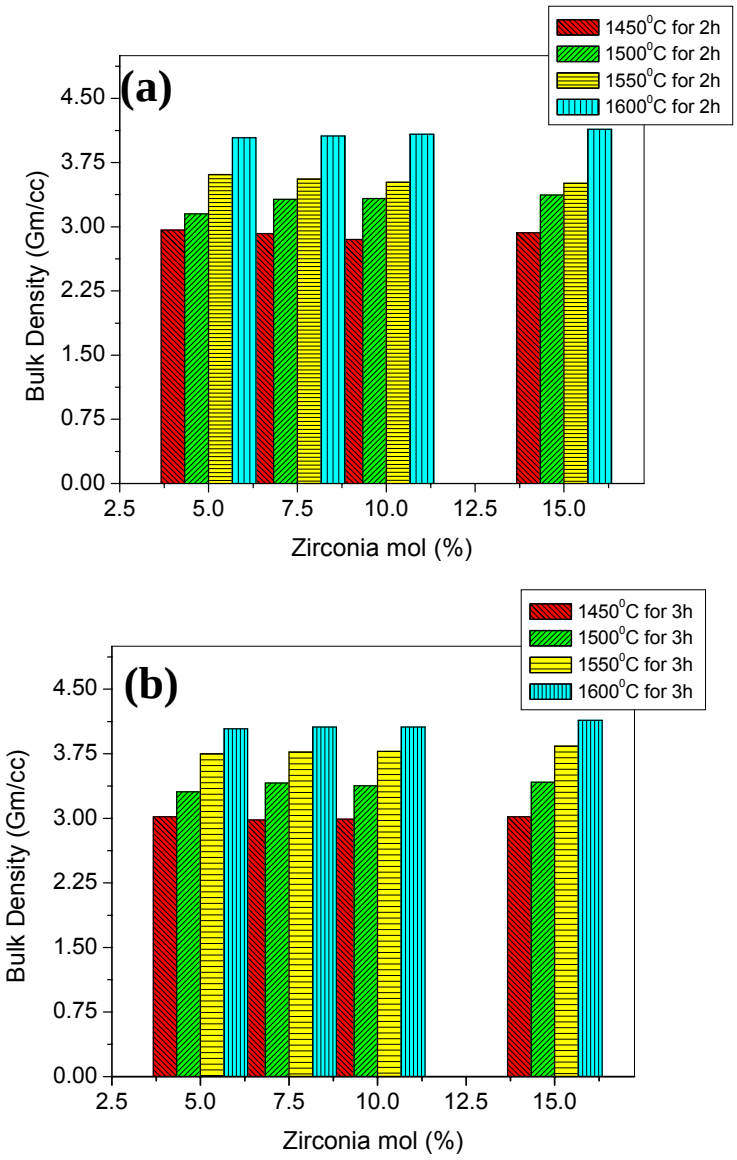

Fig 5.2.2. Bulk density of Al_2O_3-xZrO_2 (x = 5,7.5,10,15 mol%) with holding time (a) 2h and (b) 3h

At 1450^{o}C for 2h holding, the density of A1ZB, A2ZB, A3ZB and A4ZB composites are 2.96, 2.92, 2.85 and 2.93 gm/cc respectively. However, these densities are gradually increased with increasing temperature. A similar trend can also be followed for 3h holding period, where the lowest bulk densities vary 2.98 - 3.02 and 4.04 – 4.18 gm/cc at 1450^{o}C and 1600^{o}C respectively. The density result reveals that the elimination of pore, simultaneous grain growth with grain boundary diffusion and lattice diffusion are the predominant mechanism to compact the material at high temperature. Entrapped porosity of A4ZB specimens is nearly eliminated at 1550^{o}C and 1600^{o}C but density decreases from

4.18 to 4.13 gm/cc. Very fast grain grow rate has a detrimental effect on density in the later stage of sintering as many small pores remain because of exaggerated ZrO_2 coarsening and pore coalescence. The earlier study reveals that densification of zirconia dispersed alumina composite is mainly ascribed to the pore coalescence and grain growth of the particles.

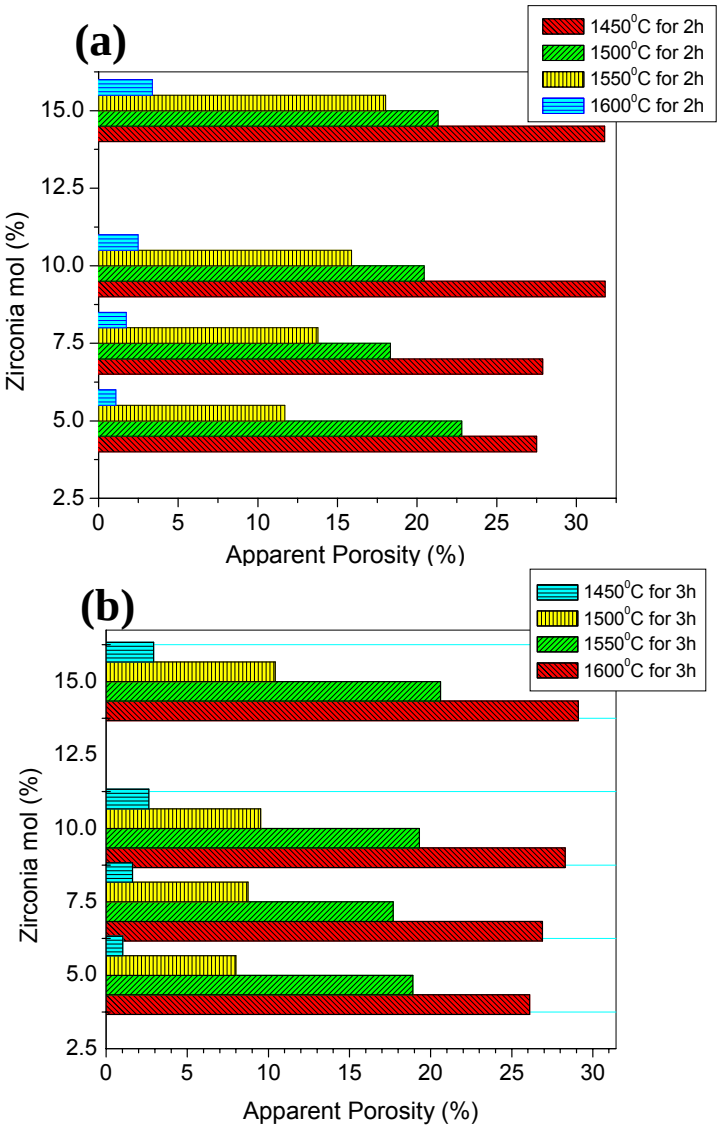

Fig 5.2.3. Apparent porosity of Al_2O_3-xZrO_2 (x = 5, 7.5,10,15 mol%) with holding time (a) 2h and (b) 3h

Fig 5.2.4 and Table 5.2.2 shows that the firing temperature and holding period have significant effect on the reduction of porosity. The apparent porosity of A1ZB, A2ZB, A3ZB and A4ZB gradually decreases with increasing temperature. At 1500°C, the porosity of A1ZB could be reduced up to ~22% and ~18% for 2h and 3h soaking respectively. However, low porosity (1.02 to 2.92%) could be noticed at 1600°C for 3h.

Table 5.2.2. Bulk density and apparent porosity of Al_2O_3-xZrO_2 (x = 5, 7.5,10,15 mol%)

Temperature (^{0}C)	Soaking Period (hr)	A1ZB		A2ZB		A3ZB		A4ZB	
		BD	AP	BD	AP	BD	AP	BD	AP
1450	2	2.96	27.5	2.92	27.9	2.85	31.8	2.93	31.77
	3	3.02	26.1	2.98	26.9	2.99	28.33	3.02	29.1
	4	3.09	24.11	3.04	25.77	3.06	26.88	3.12	27.2
1500	2	3.15	22.8	3.32	18.32	3.33	20.44	3.37	21.31
	3	3.31	18.9	3.41	17.69	3.38	19.31	3.42	20.61
	4	3.55	13.1	3.47	16.02	3.42	18.32	3.44	19.77
1550	2	3.61	11.7	3.56	13.77	3.52	15.89	3.51	18.02
	3	3.75	8.0	3.77	8.74	3.78	9.52	3.84	10.43
	4	4.03	1.2	4.06	1.94	4.07	2.58	4.18	3.38
1600	2	4.04	1.08	4.06	1.74	4.08	2.48	4.18	3.38
	3	4.04	1.02	4.06	1.62	4.08	2.62	4.14	2.92
	4	4.05	0.8	4.07	1.57	4.09	2.88	4.13	2.79

BD = (Bulk Density); AP = (Apparent Porosity).

An interesting observation can be perceived that the apparent porosity increases with increasing the zirconia content, although the average porosity decreases with increasing temperature. This porosity usually originates from entrapped pore during green compaction and the elimination of hydrated water from additive. These pores are very difficult to remove during the final stage of sintering at low temperature, which confers low sintered density. However, the density gradually increases since nanocrystalline material contains a very large fraction of species at the grain boundaries; the numerous interfaces provide a high density through short circuit diffusion paths. Consequently, they are expected to exhibit an enhanced diffusivity in comparison with single crystals or conventional coarse grained polycrystalline materials with same chemical composition.

Table 4.3 represents the typical theoretical density (TD) of α-Al_2O_3, t-ZrO_2 and m-ZrO_2. From XRD analysis the phase content (quantitatively) can be calculated, which was finally ascribed the TD of specimens (A1ZB, A2ZB, A3ZB and A4ZB).

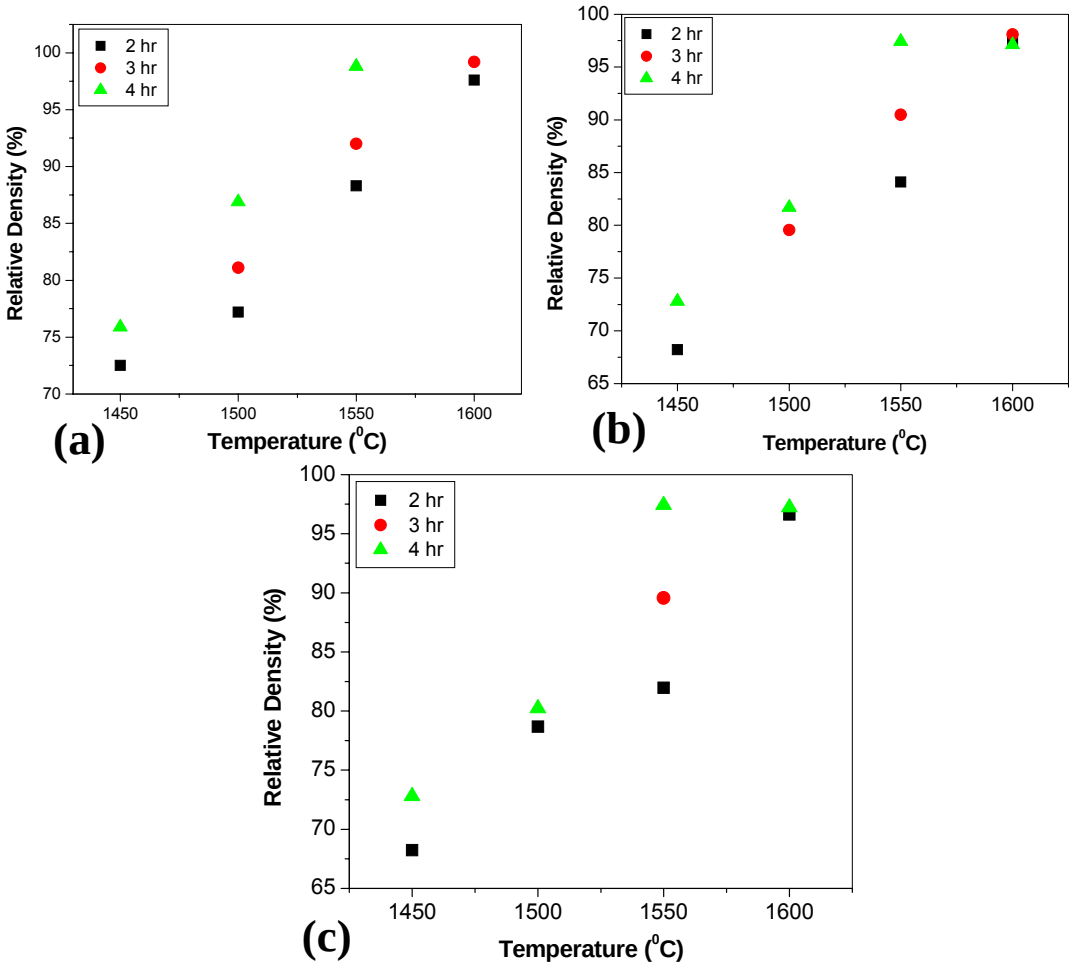

Fig 5.2.4. Relative density vs. sintering temperature of (a) Al_2O_3-5ZrO_2 (b) Al_2O_3-10ZrO_2 and (c) Al_2O_3-15ZrO_2

Table 5.2.3 listed the calculated TD of the specimens. The relative density was estimated from the experimental and calculated x-ray density. XRD analysis was carried out for as-sintered materials. The fraction of monoclinic ZrO_2 was calculated using the equation 4.3 and listed in Table 5.2.3:

Table 5.2.3. Determination of theoretical density of sintered composites by XRD technique

Identification	Composition	Zirconia content		Theoretical Density (gm/cc)
		Tetragonal ZrO_2 Content (%)	Monoclinic ZrO_2 Content (%)	
A1ZB	95 Al_2O_3 + 5ZrO_2	100	-	4.09
A2ZB	92.5 Al_2O_3 + 7.5ZrO_2	95	5	4.13
A3ZB	90 Al_2O_3 + 10ZrO_2	91	9	4.19
A4ZB	85 Al_2O_3 + 15ZrO_2	88	12	4.29

The X-ray density of all other specimens was worked out from the phase analysis. The relative density of the specimen were estimated and plotted from the TD and BD of the sintered samples. At 1450°C, a continuous 2h isothermal treatment can improve ~10–15 % relative density of the green compacts. However, at high temperature the relative density of Al_2O_3-xZrO_2 (x = 5, 7.5, 10 and 15mol %) is varying within 96-99%. The continuous decrease of the relative density is caused by the lowering of t-ZrO_2 phase at higher content of ZrO_2 in A4ZB. The decrease in t-ZrO_2 phase or simultaneous increase in m-ZrO_2 phase may be explained by a rapid increase in grain size of zirconia particles.

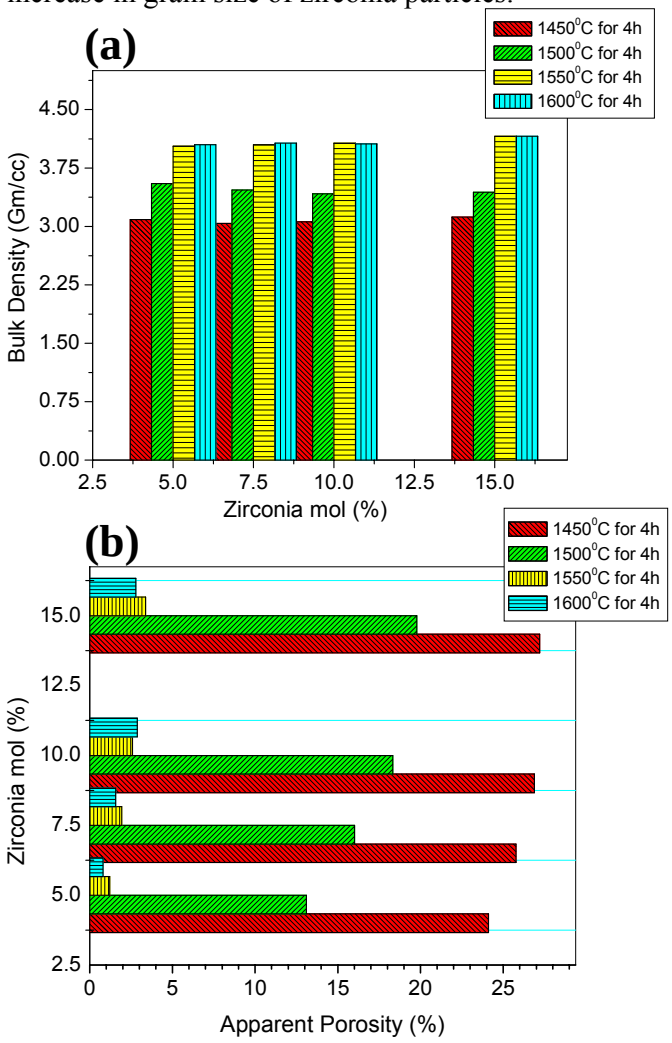

Fig 5.2.5. Bulk density (a) and apparent porosity (b) of Al_2O_3-xZrO_2 (x = 5, 7.5,10,15 mol%) with 4h holding time.

Fig 5.2.5 shows the sintered density and apparent porosity of the Al_2O_3-xZrO_2 (x = 5, 7.5,10,15 mol%) composites with respect to their different sintering temperature for 4h holding time. It is observed that the sintered density of the compact increases with increase in sintering temperature and reaches a maximum value at 1550°C. Although a similar range of

density could be observed for 1600°C for 3h sintered specimen. The density of the pellets sintered at 1500°C for 4h are lower than those of 1600°C for 3h, however, grain sizes of the former are smaller. With consideration of density and microstructure, the optimum sintering temperature is considered to be 1550°C for 4h and detail phase characteristics and thermo-mechanical properties of the sintered samples have been evaluated and correlated.

Earlier studies reveals that the fast grain growth rate has a detrimental effect on the density in final stage sintering even with higher content of zirconia, since pore coalescence in alumina matrix and segregation of zirconia particles takes place[147]. The true density of the sinter product depends on the microstructure and phase content. The characteristic bulk density and apparent porosity of the sintered specimens can be explained as follows: The densification of zirconia toughened alumina sintered samples is depending on two factors:

a) Relative content of monoclinic and tetragonal zirconia phase.
b) Porosity of the samples.

Again, the retention of the tetragonal phase depends on number of factors

a) Nature of the stabilizing oxide
b) Content of the stabilizing oxide
c) Constraining matrix

The more constraining the matrix, the more difficult it is for the tetragonal grain to convert back to monoclinic form. If the porosity levels are high the probability of relative content of tetragonal phase would be comparatively less. Phase analysis of the sintered samples (which is discussed in section 5.3) show that the percentage of tetragonal phase retention is more for lower content of zirconia in comparison with higher zirconia content.

At 1550°C for 4h, the maximum monoclinic content of A4ZB is around 10%. A1ZB sample contains 100% tetragonal zirconia polycrystals (TZP) without addition of sintering additives. The t-ZrO_2 is denser than m-ZrO_2. From XRD analysis of different specimens sintered at different temperatures, it is revealed that the monoclinic zirconia content in the sample increases presumably due to the increase in the sintering temperature. It is well known that there is a critical grain size for the tetragonal zirconia depending on the stabilizing oxide and constraining matrix[3]. Consequently, the possibility of formation of monoclinic zirconia increases with increasing sintering temperature, if the grain size of the sintered sample comes close to the critical grain size. Usually, formation of monoclinic zirconia would reduce the bulk density of the sintered samples. Table 5.2.2 clearly exhibits that the density of the sintered samples has increased order of tendency for a particular sintering profile. Hence, it

can be concluded that the reduction of porosity is the prime factor for the sintering as well as enhanced grain growth at high temperature has not significant contribution to increase in sintered density.

Relative densities of the sintered materials, plotted against zirconia content at different time and temperatures, are shown in Fig. 5.2.3. The reported values are the average of data obtained from five specimens. Fig. 5.2.3 and Table 5.2.4 show that the relative densities of the samples, at all sintering temperature, are lower for high ZrO_2 containing samples. Densification results for 1h soaking at different temperature experience very low relative densities compared to higher dwell time, which are not listed in this results. At 1450^oC, the relative density decreases from 75% to 72% with the addition of 5 to 15 mol% ZrO_2 and also exhibits low densification. The rate of densification increases beyond 1500^oC and good densification could be achieved at 1550^oC. The maximum density of ~98% ρ_{th} is observed with addition of 5mol% ZrO_2 at 1550^oC for 4h. However, for higher ZrO_2 content (15mol%), the relative density is reduced to ~97% ρ_{th} at the same sintering conditions, since m-ZrO_2 increases with temperature and zirconia content.

However, further increase of temperature up to 1600^oC reveals good densification with an exaggerated grain growth. The transformation of boehmite to α-Al_2O_3 is associated with 24 vol% porosity formations and it is extremely difficult to remove the residual pores trapped within α-alumina grains during the final stage of conventional sintering. This factor is even severe for the low bulk density for the powder calcined at lower temperatures. It can also be noticed that 97.6% densification was achieved at 1600^oC for 2hrs due to the higher sintering ability of these fine powder particles at high temperature. A significant grain growth is observed during sintering at 1600^oC for 3h using nanopowders, which is an inherent drawback of conventional sintering. Non-conventional heating like microwave sintering, spark plasma sintering etc may produce materials with near full densities [169].

The DTA analysis (Fig 5.1.1 and 5.1.2) reveals that the alumina phase transformation shifted from 1160 to 1152^oC with decreasing zirconia content. However, the phenomenon does not affect the densification behavior of the sintered composites. From Fig.5.2.6 it is observed that the relative density of the sintered composite contains unstabilized zirconia decreases with respect to zirconia content, unlike ceria and yttria stabilized zirconia containing composites. This is due to the decrease of t-phase with increase in the zirconia content for the unstabilized zirconia. This t→m phase transformation of zirconia causes volume expansion (~5%) leading to a decrease in the relative density of the composite[6]. The

XRD analysis of the as-sintered specimen shows that almost 100% of the t-phase is retained when zirconia content is 5mol%. The simultaneous sintering and phase transformations may provide a better opportunity for low temperature sintering of alumina-zirconia composite than the conventional approach on the basis of alumina.

Table 5.2.4. Variation of relative density at different temperature as function of time and ZrO_2 content

Temperature (°C)	Soaking Period (hr)	Relative Density (%)			
		A1ZB	A2ZB	A3ZB	A4ZB
1450	2	72.5	-	68.2	68.23
	3	-	-	-	-
	4	75.89	74.23	73.12	72.8
1500	2	77.2	-	79.56	78.69
	3	81.1	-	-	-
	4	86.9	83.98	81.68	80.23
1550	2	88.3	86.23	84.11	81.98
	3	92.0	91.26	90.48	89.57
	4	98.5	98.3	97.14	97.43
1600	2	98.92	98.3	97.52	97.32
	3	-	-	-	-
	4	99.2	98.43	97.12	98.81

Table 5.2.5. Linear shrinkage of ZTA composites at different temperature with 4h duration

Temperature (^{0}C)	Soaking Period (hr)	Linear Shrinkage (%)			
		A1ZB	A2ZB	A3ZB	A4ZB
1450	4	13.2	13.8	14.2	14.4
1500	4	20.56	21.93	21.7	22.54
1550	4	23.07	23.15	23.68	23.76
1600	4	26.95	26.19	25.3	24.5

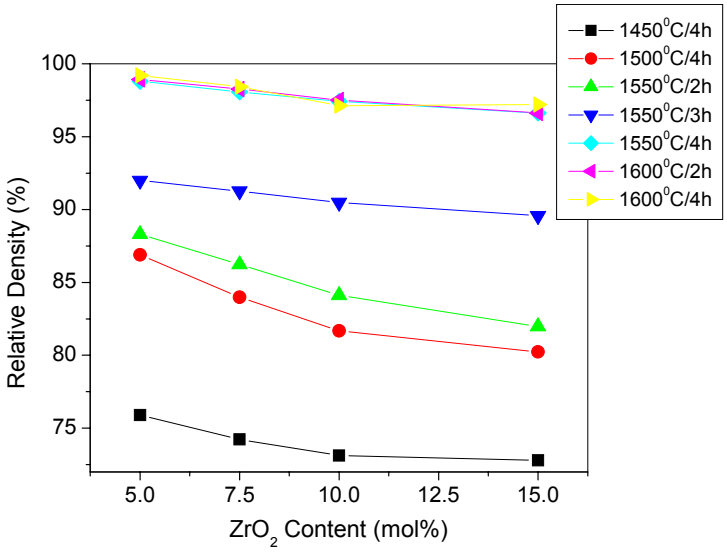

Fig 5.2.6: Relative density with respect to temperature, time and ZrO_2 content

The shrinkage data and characteristics behavior of sintered 1550°C/4h specimens are represented in Table 5.2.5 and Fig 5.2.7. Typically, 2% standard deviation around the average shrinkage data from five specimens is observed in our experiments. The elimination of pore and grain growth of the respective crystalline phases is responsible for the firing shrinkage within the temperature range 1450–1600°C. Initially a steep rise is observed up to 1500°C followed by relatively slower rate up to 1600°C.

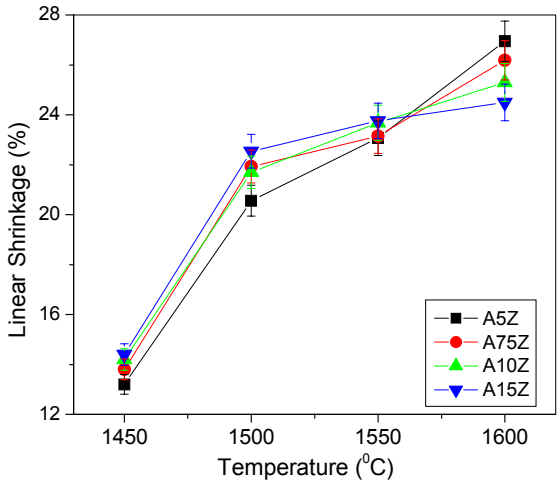

Fig 5.2.7: Linear shrinkage of Al_2O_3-ZrO_2 composites sintered for 4h.

In the later stage of sintering, grain boundary diffusion is operative declining the rate of material transport[23]. With the increase of the zirconia content, the extent of shrinkage decrease at high temperature as monoclinic phase increases. The nature of the shrinkage curves does not exhibit any variation with respect to zirconia content.

5.3 Microstructure and Phase Analysis

5.3.1. Scanning Electron Microscopic Analysis

Fig. 5.3.1 to Fig. 5.3.4 shows the scanning electron microscopic images of the sintered, polished and thermally etched Al_2O_3-xZrO_2 (x = 5, 7.5, 10 and 15 mol%) specimens, where precursor powders were calcined at 1000^oC for 2h, uniaxially pressed at 250MPa with addition of 5 weight percent uncalcined powder as additive, followed by cold isostatic press at 300MPa and sintered at 1550^oC for 4h. The micrograph exhibits the Al_2O_3 and ZrO_2 grains as dark and whitish color respectively, where zirconia grains are embedded around the alumina grain and/or within the grain. However, small fractions of intragranular zirconia grain are also being noticed.

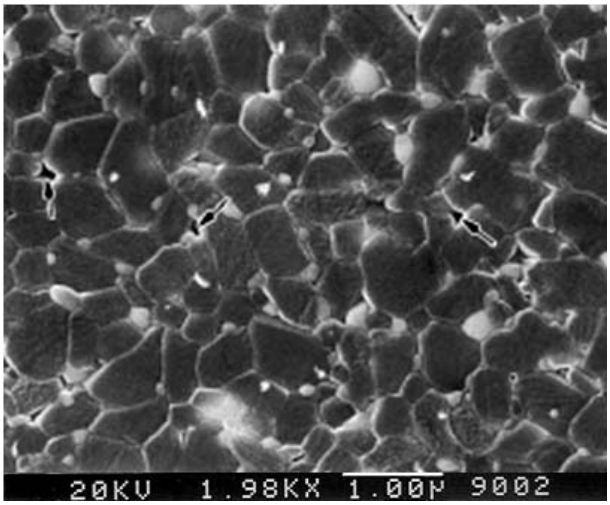

Fig 5.3.1. SEM image showing the microstructure of polished and thermal etched Al_2O_3-5ZrO_2 (sintered at 1550^{0}C/4h) specimen. The phases with darker and white and contrast indicate Al_2O_3 and ZrO_2 respectively. The arrow indicates the pore.

As shown in Fig 5.3.1, the zirconia particles are in range of 50-160 nm, whereas dimensions of alumina grains are up to 0.2 - 0.8µm. However, with increase in zirconia content, the grain size of zirconia increases with restriction of alumina grain size. The microstructure contains pores at isolated pockets. It can be seen that voids are nucleated mainly at grain boundary or at triple points and grow at around the matrix grain. The relative large void is attributed to the differential sintering of the alumina and zirconia phases and also due to the creation of pores, which has been initially originated from entrapped pore in the green compacts and uncalcined precursor as additive. Hence, the decrease in the sintered

density at low temperature could be due to the aggregate and cavity structure, which inhibits the sintering of ZTA compact[131]. Earlier studies demonstrated that the fine cavities do not grow readily to the large ones because cavity growth exceeding the current grain size is constrained by the surrounding matrix [170]. Based on this, it is thought that in addition to diffusion, zirconia grain in alumina grains acted to mitigate localized stress concentrations and suppress cavity generation. However, the overall behavior is governed by a combination of the behavior of the two-grain sizes and morphology.

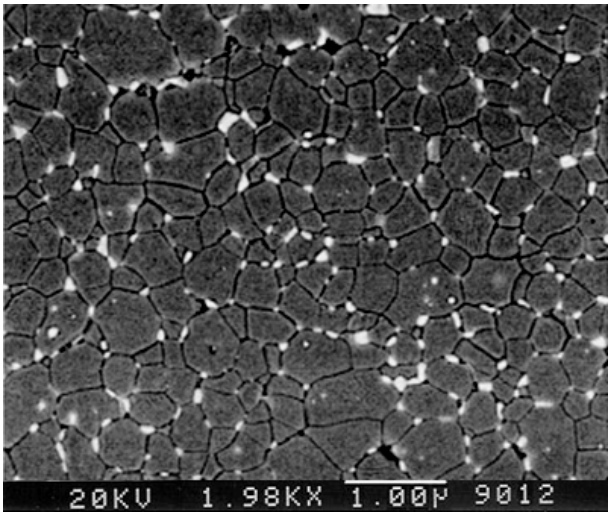

Fig 5.3.2. SEM image showing the microstructure of polished and thermal etched surface Al_2O_3-ZrO_2 (sintered at 1550^{0}C/4h) specimen. The phases with darker and white and contrast indicate Al_2O_3 and ZrO_2 respectively.

Fig. 5.3.2 shows the polished and thermally etched surfaces of as-sintered A2ZB specimens fired at 1550^{o}C for 4h. Microstructure reveals that the average alumina grain size decreases and varies within the range from 0.1 to 0.7µm, and is fairly homogeneous inside the composite.

Average ZrO_2 grain sizes were 30 – 210nm; zirconia particles are isolated at grain boundaries between bigger alumina grains. For a particular composition, the grain size for both alumina and zirconia particles increase with increasing temperature and time. From the X-ray diffraction analysis, the ZrO_2 particles are mainly of tetragonal phase for A1ZB specimen (see Fig. 5.3.6). Fig. 5.3.2 reveals that the biggest zirconia grains have similar sizes to the smallest alumina grains; the absence of zirconia agglomerates indicates a homogeneous relative distribution of both the phases. ZrO_2 particles at triple junctions with two Al_2O_3 grains showed a smaller dihedral angle than the Al_2O_3 grains, and ZrO_2 particles surrounded by Al_2O_3 grains tend to have concave interphase boundaries rather than flat ones, indicating a

higher grain boundary energy γ_{AA} between Al_2O_3 grains than between ZrO_2 grains (γ_{ZZ}) or than at the Al_2O_3–ZrO_2 interphases (γ_{AZ}) [171].

As shown in Fig. 5.3.3, the grain size distribution has no significant change, however, the average alumina and zirconia grain size could be detected 0.07 – 0.65 μm and 30-220 nm, respectively.

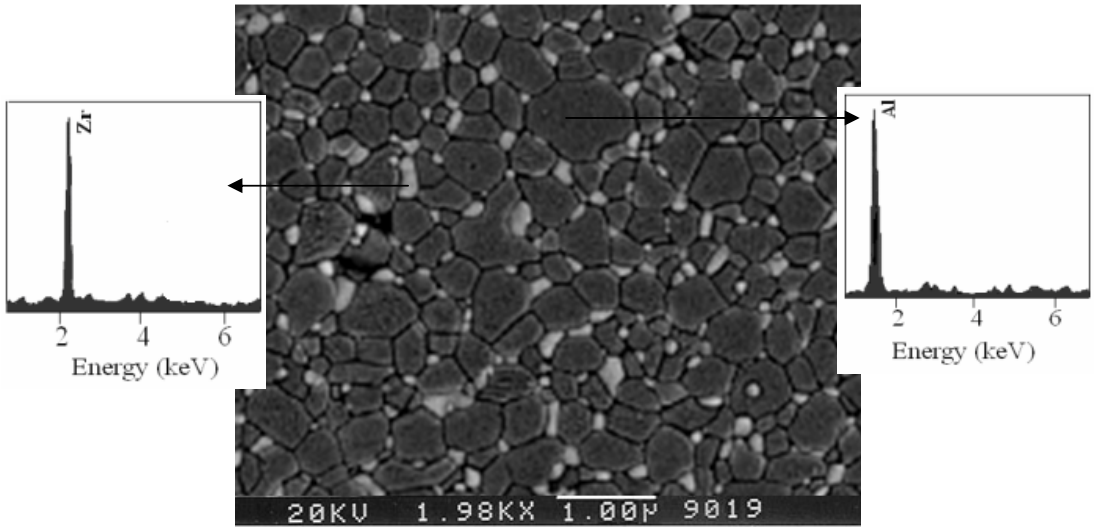

Fig 5.3.3. SEM image showing the microstructure of polished and thermal etched Al_2O_3-$10ZrO_2$ (sintered at 1550^0C/4h) specimen. EDX spectra acquired from the individual alumina and zirconia grain.

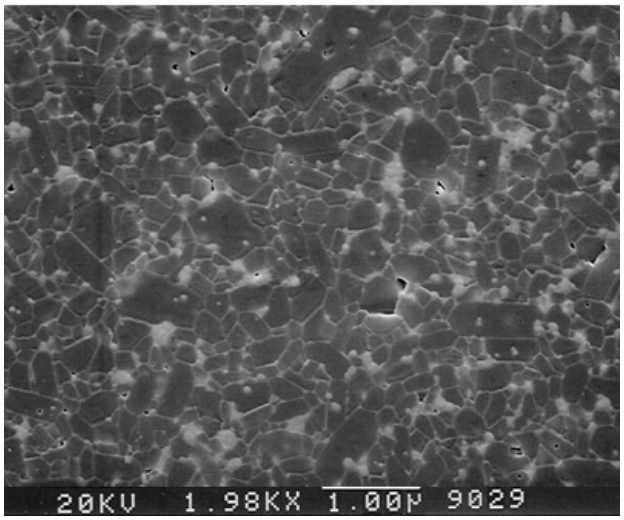

Fig 5.3.4. SEM image showing the microstructure of polished and thermal etched Al_2O_3-$15ZrO_2$ (sintered at 1550^0C/4h) specimen. The phases with darker and white and contrast indicate Al_2O_3 and ZrO_2 respectively.

The small zirconia grains are uniformly dispersed and located between large grains in the alumina matrix. EDX analysis is carried out to observe the distribution of different

elements within the matrix, which indicates the presence of Al within darker phase and that of Zr within whitish grain.

The A4ZB microstructure indicates that the zirconia grains are somewhere segregated within the alumina matrix (Fig. 5.3.4), as well as relatively more isolated voids can be observed in comparison with A3ZB specimen. The Al_2O_3 and ZrO_2 grain size could be detected 0.04 -0.6 μm and 30 -250 nm, respectively.

5.3.2. Grain Size Analysis

It is believed that the zirconia grains, which are primarily located at the triple junctions, must be due to the strong self-diffusion of zirconia although some small zirconia grains become relocated within the alumina grains and process near spherical geometry. This phenomenon can be suggested to occur by the growth of alumina grains, constrained by relatively few zirconia grains into a single large grain which then `swallowed up' surrounding alumina and zirconia grains. Lange and Hirlinger[172] also observed various drag/breakaway configurations including zirconia grains near the three-grain junctions and at two-grain boundaries. It is also observed (Fig. 5.3.1) that two kinds of zirconia grains exist in the ZTA composite, namely (i) faceted intergranular zirconia grains (mostly at the grain corners) and (ii) spherical intragranular zirconia grains. The large intergranular grains may be related to the faster coarsening rate.

During sintering, finely dispersed zirconia particles retard the motion of the alumina grain boundaries (inhibit grain growth). However, these zirconia particles, eventually come together with each other, are located at grain junctions (i.e. little effect on suppressing grain growth) and are responsible for a grain boundary pinning effect[173]. However, the addition of 15 mol% of zirconia still shows abnormal grains. The large grains found in the sample are still due to non-uniform distribution of zirconia grains, which are not sufficient to hinder the growth of every alumina grains. As most zirconia grains are located at triple junctions and at grain boundaries of alumina, coarsening of zirconia grains are controlled by the coalescence. It is also clear that the volume fraction of zirconia influences the spatial distribution of zirconia grains and high volume fraction of zirconia causes the zirconia to be more agglomerated continuous and interconnected.

Table 5.3.1 represents the grain sizes of both Al_2O_3 and ZrO_2 phases as revealed from SEM micrographs. The principal merit of the microstructure observed in the alumina–zirconia composites obtained by the sol-gel route are the adequate relative grain size ratio and phase

distribution between both phases, allowing zirconia particles to be present at most grain boundaries, without excess of second-phase particles that would create agglomerates and without the existence of areas with poor density of zirconia particles. Fig. 5.3.3 shows the variation of alumina and zirconia particle size with respect to zirconia content in composites.

Table 5.3.1. Grain size variation of Al_2O_3-xZrO_2 (where x = 5, 7.5, 10 and 15 mol%) composites sintered at 1550^0C for 4h.

Identification	Average Grain Size (nm)		% ZrO_2 phase Content	
	Al_2O_3	ZrO_2	t-ZrO_2	m-ZrO_2
A1ZB	500	110	100	-
A2ZB	400	120	95	5
A3ZB	360	125	91	9
A4ZB	320	140	88	12

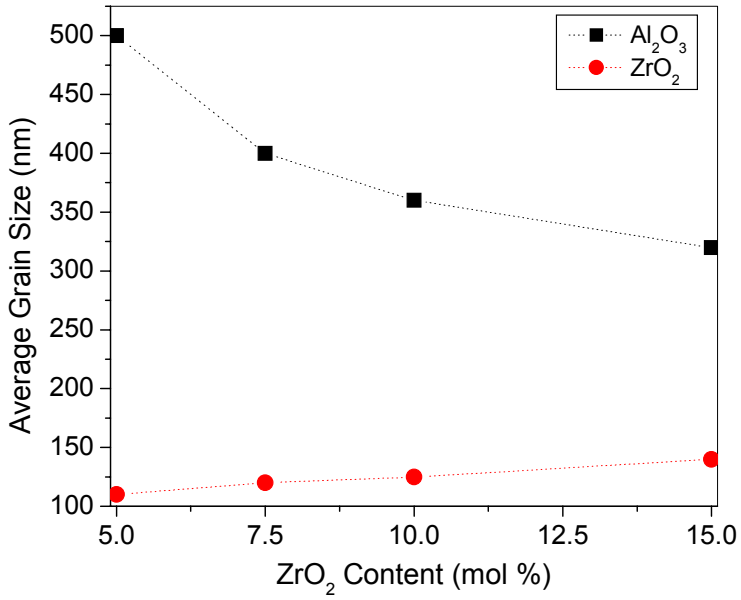

Fig 5.3.5. Average grain size of sintered composites as a function of ZrO_2.

The zirconia grain size increases with increasing zirconia content while alumina grain sizes decrease, thus the grain size ratios $d_{[A]}/d_{[Z]}$ are between 4.35 for A1ZB and 2.29 for A4ZB (Fig. 5.3.5). This relationship reveals that the matrix grain size can be controlled with variation of introduction of second-phase.

5.3.3. Phase Analysis

The XRD patterns of ZTA ceramics after sintering at 1550°C for 4h are shown in Fig. 5.3.6, which demonstrates the difference of phase content. The XRD patterns of ZTA ceramics containing 5 to 7.5mol% ZrO_2 are almost the same; however, ~5% m-ZrO_2 can be detected for A2ZB. The ZrO_2 particles are mainly of tetragonal phase embedded in α-Al_2O_3. The main peaks of t-ZrO_2 are sharp and high. The A3ZB and A4ZB sintered samples contain over 90% and 85% t-ZrO_2 phase respectively, which reveals their good stability. The peak position is determined by the FWHM (full width of half-maximum) middle point method. The phase analysis of A3ZB shows the presence of t-ZrO_2 and α-Al_2O_3 as major phases along with small amount (~9%) of monoclinic zirconia. With addition of 15 mol% ZrO_2, the monoclinic phase increases sacrificing the t-ZrO_2 phase. Around 12% m-ZrO_2 is measured in case of A4ZB. It can be attributed to the easing of the constraining matrix, which helps in the microcrack toughening.

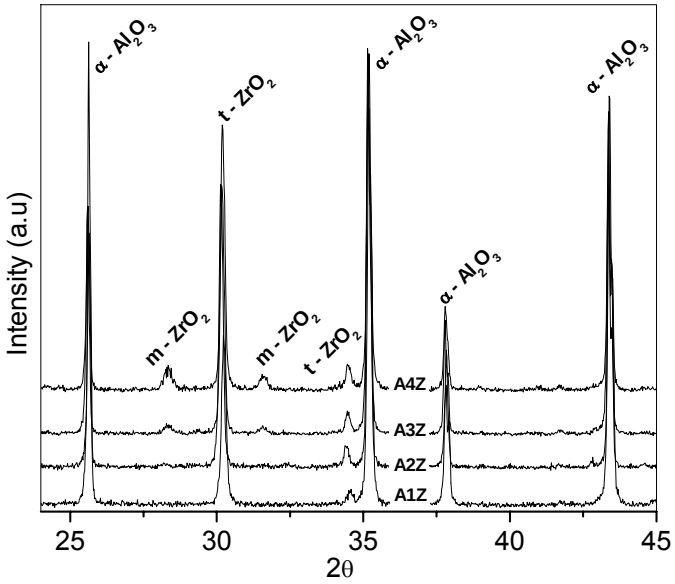

Fig 5.3.6. XRD of polished Al_2O_3-x ZrO_2 (where x = 5, 7.5, 10, 15 mol%) composites sintered at 1550°C for 4h.

On the other hand, the constraint is imposed by the surrounding alumina grains, which influence the zirconia transformation. Alumina matrix with high elastic modulus and thermal expansion coefficient restricts the expansion of zirconia occurring during t→m transformation and reduces the transformation temperature. Zirconia present in the composite is, therefore, retained in the tetragonal form because of its fine size and constraints imposed by the alumina grains. It also confirms that the nanocrystallinity of the microstructure has been maintained

even after high temperature treatment. This indicates that the nanosize alumina particles prevent the tetragonal to monoclinic transformation by matrix constraint and keeps the zirconia particles apart to avoid the growth of t-ZrO_2.

The obtained grain size versus holding time of A4ZB specimens are plotted in Fig. 5.3.7. At 1550^{o}C, the obtained average ZrO_2 grain size varied from ≥40nm (30min) to ≥170nm (240 min or 4h), whereas Al_2O_3 grain size varies within the range of 150nm to 350nm. The data demonstrates that the grain growth is rather limited at 4h holding period but increases dramatically as/and when the sintering temperature and duration increases.

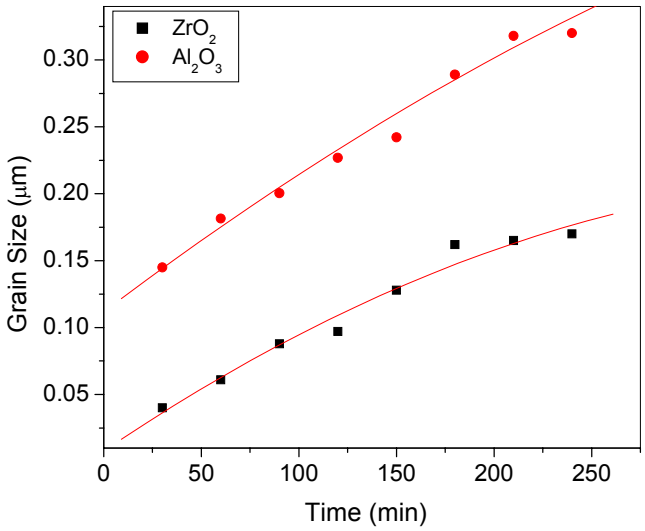

Fig 5.3.7. The effect of dwell time on the grain size of Al_2O_3-15ZrO_2.

Fig. 5.3.7 reveals most of the ZrO_2 grain growth occurs within the first 3 hrs., and the obtained data suggests that the grain size are not significantly changed even after prolonged heat treatment at 1550^{0}C. Thus, the grain growth is also very fast in this process above a certain critical temperature, and the underlying mechanisms are thermally activated. The process discussed above cannot be operative for fully densified samples; but the grain-boundary diffusion and grain-boundary migration processes are enhanced at high temperature. With 4h holding period, the average Al_2O_3 grain size is approximately 320nm, but accurate measurements are difficult due to the fine grain size and containing porosity at low temperature and time. XRD line broadening has been used to evaluate the grain size at lower-holding time sintering of nano-sized precursor powder, but this technique is only suitable for a crystallite size below ~40nm; thus, this technique cannot be applied for low temperature sintered specimens [149]. In order to obtain qualitative composition of the A3ZB specimen, X-ray mapping had been carried out using EPMA on the polished surface and the results are

presented in Fig. 5.3.8. The distribution of Zr is quite homogeneous as no part of the micrograph shows clustering of Zr-rich region. The Al is quite homogenously distributed throughout the matrix (Fig. 5.3.8a). Additionally, the X-ray image presented in Fig. 5.3.8b closely matches the composition of the composite reinforced with 10mol% ZrO_2.

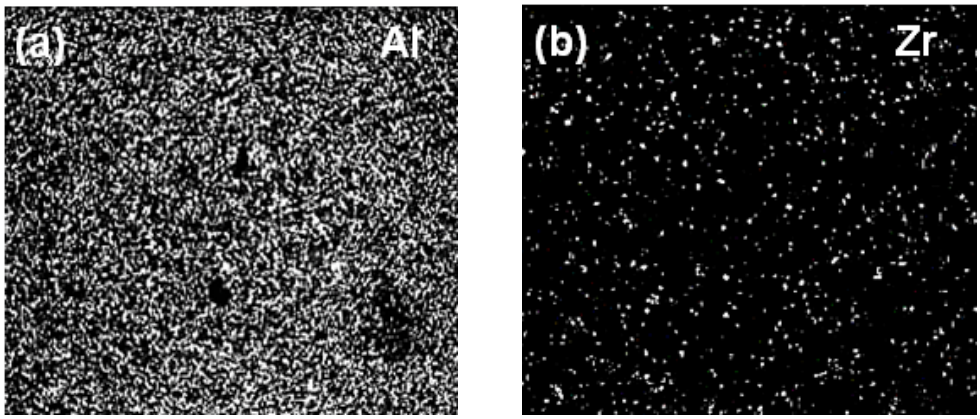

Fig 5.3.8. X-ray mapping micrographs of different elements (a) Al and (b) Zr of Al_2O_3-10ZrO_2

5.3.4. TEM Analysis

Fig 5.3.9 shows the TEM image of a 15mol% ZrO_2 dispersed A4ZB composite. Fig. 5.3.9a micrograph exhibits the laths of monoclinic formed within tetragonal zirconia. Selected area electron diffraction of the grain confirms it to be monoclinic phase (Fig 5.3.9b).

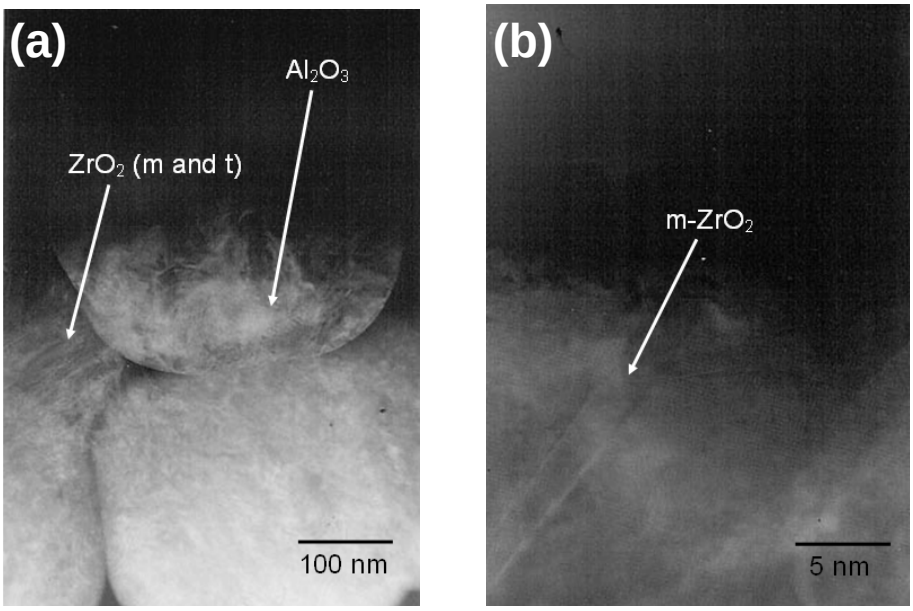

Fig.5.3.9. TEM of Al_2O_3-15ZrO_2 (a) and zirconia grain (b), where m-ZrO_2 lath could be noticed within ZrO_2 grain.

Substantial amount of zirconia (15mol%) addition was assisting the formation of larger grain size, which was transformed to monoclinic phase during cooling. The excess amount of monoclinic phase may have detrimental effect on thermal and mechanical properties of ZTA composite. The detail thermo-mechanical properties are thoroughly discussed in Section 5.4.

5.4. Mechanical and Thermal Properties

Oxide ceramics by themselves generally do not have very high fracture toughness and/or high fracture strength from room temperature to elevated temperature. Composite materials have the possibility of developing microstructures, where the mechanical properties can be tailor-made to suit the service requirements. Composite of zirconia toughened alumina (ZTA) have the possibility of developing high-strength and toughness ceramics. Mechanical strength of ceramic composites is depending mainly on two parameters. One is the intrinsic property of the phases present and the microstructure of the material. In multiphase material, microstructure of the materials, i.e. the amount and distribution of the phases play a crucial role in determining the mechanical strength.

5.4.1. Hardness and Elastic Modulus

The Vickers hardness of composites obeys a linear mixture rule. It can be observed that with increase in zirconia content, the hardness of the composite diminishes. The hardness of this CMC (Ceramic Matrix Composite) can be measured through indentation method, where the indentation load is critical in the measure of hardness and fracture toughness.

Table 5.4.1: Room Temperature Vickers hardness, elastic modulus and fracture toughness of sintered (1550^0C for 4h) specimens.

Identification	H_v(49N) GPa	Elastic Modulus (GPa)	Fracture Toughness (MPa.$m^{1/2}$)
A1ZB	16.83 ± 0.92	305 ± 16	5.3 ± 0.21
A2ZB	15.86 ± 0.65	294 ± 20	6.24 ± 0.32
A3ZB	15.21 ± 0.82	286 ± 12	6.84 ± 0.25
A4ZB	14.98 ± 0.32	267 ± 21	6.41± 0.36

The amount of load could affect the indentation size and the crack length (being dependent on the sample dimension and microstructure of the material). Many ceramic exhibits a decreasing trend in hardness with increase of load, which is a major problem to determine the precise hardness value. The solution is to measure of the Vickers hardness with

higher loads, where the influence of the load is the measure of the decrease in hardness and thus the standard hardness can be obtained[174]. In the present work, the hardness values are measured using 49N load and the average value of five indented values are listed in Table 5.4.1. Vickers Hardness and elastic modulus of sinter samples at different concentration of zirconia are shown in the Fig. 5.4.1. Hardness and elastic modulus of the studied materials may be explained on the basis of porosity and the grain size.

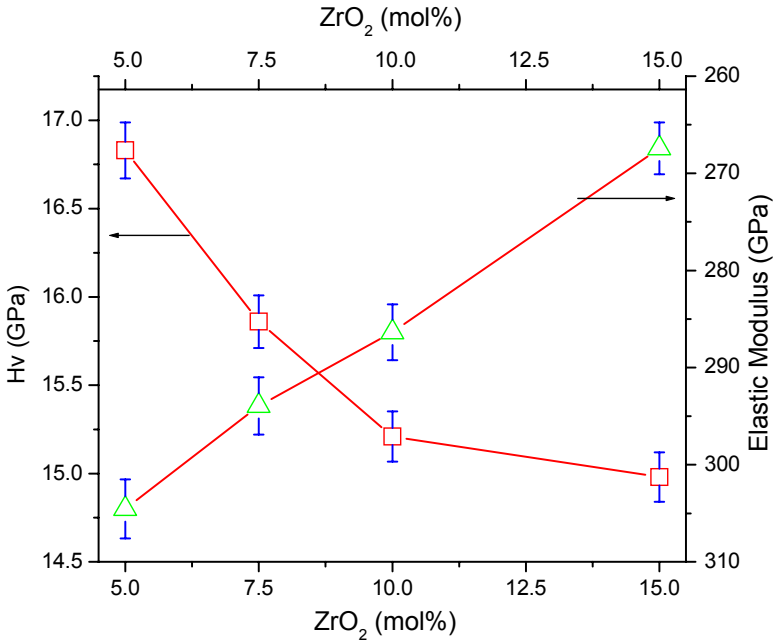

Fig. 5.4.1. Elastic modulus and Vickers hardness (at 49N load) as a function of zirconia content

The hardness of the ZTA composite decreases (~17 to 15GPa) with the addition of zirconia as alumina is harder than zirconia. Again, amount of zirconia has an adverse affect on the hardness of the composites due to coarsening of the zirconia grains and formation of subsequent porosity. It has also been noticed that these composite materials also obey Hall-Petch[175,176] relationship. The present study shows that the average particle size has significant impact on hardness value, which is controlled by the particle size.

Elastic modulus of the composite depends on the volume fraction of the phases present and their individual modulus of elasticity. At 1550^{o}C, densification of the composites is improved by reducing pore volume fraction of the matrix and as a result of which the modulus of elasticity improves. Alumina has a higher modulus of elasticity compared to zirconia. So, samples containing 5mol% zirconia have the highest modulus of elasticity, whereas specimen containing 15mol% zirconia has lower levels of densification at a given sintering temperature

compared to other samples having lower amount of zirconia. Simultaneously, the grain size of zirconia increases and hinders the grain growth of alumina at 1550°C, which contributes to the lowering of elastic modulus. Nicholson [177] established that both Young's modulus and hardness of ZTA composites containing particles of zirconia stabilized with 2 mol% Y_2O_3 followed a linear rule of mixtures. A typical Vickers indentation at 49N load on the polished surface of A3ZB composite is shown in Fig. 5.4.2.

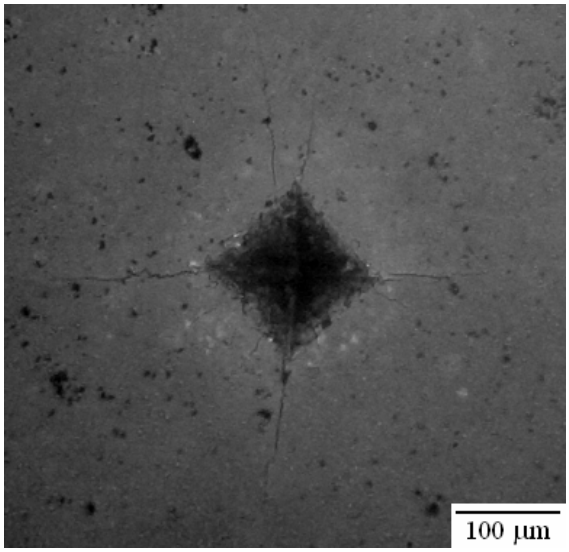

Fig. 5.4.2. SEM micrograph of Vickers indentation on Al_2O_3-10ZrO_2 and propagation of the radial cracks.

As shown in the SEM micrograph, the sign of noticeable plastic deformation around the Vickers indentation zone is absent and the length of radial cracks originating from the indentation corners is measured in order to evaluate the indentation toughness, a parameter indicative of the resistance to crack propagation. Despite measuring high hardness, the fracture toughness improves with respect to pure alumina to a value of around 7MPa.$m^{1/2}$.

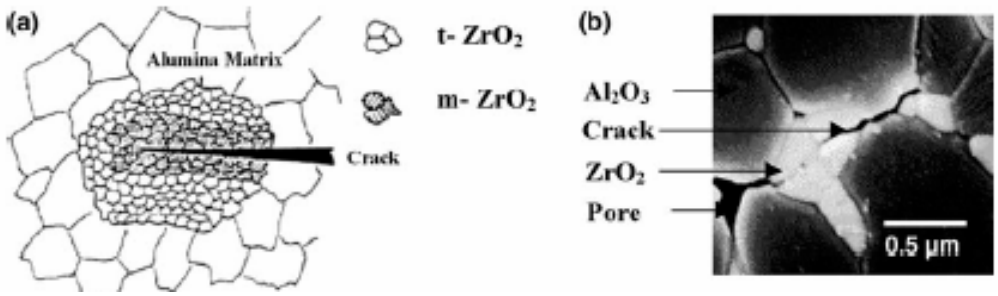

Fig 5.4.3. Schematic representation of martensitic transformation of ZrO_2 particles within the alumina matrix (a) crack propagation during indentation fracture (b).

Fig. 5.4.3 shows the propagation path of an indentation crack in the ZTA composite, which experiences along the ZrO_2 particle cluster. Hence, K_{Ic} changes with the addition of ZrO_2 may be rationalized by the relative predominance of the toughening mechanism, i.e., zirconia phase transformation of Zirconia. For the zirconia content of the ZTA studied in this work, it seems that the extent of transformation toughening is more significant, leading to an effective increase of K_{Ic}. Moreover, such transformability is also speculated to account for the reduction in hardness detected in the sintered ZTA composite, since hardness is inversely correlated with transformation easiness.

5.4.2. Fracture Toughness and Fracture Strength

In the present study, the zirconia grain size increases linearly with increasing zirconia content. The fracture toughness (K_{IC}) calculations are made based on the measurements of the radial crack length produced by Vickers (49N) indentations, according to Anstis formula. The fracture toughness and fracture strength of ZTA composite at different zirconia content are reported in Fig. 5.4.4.

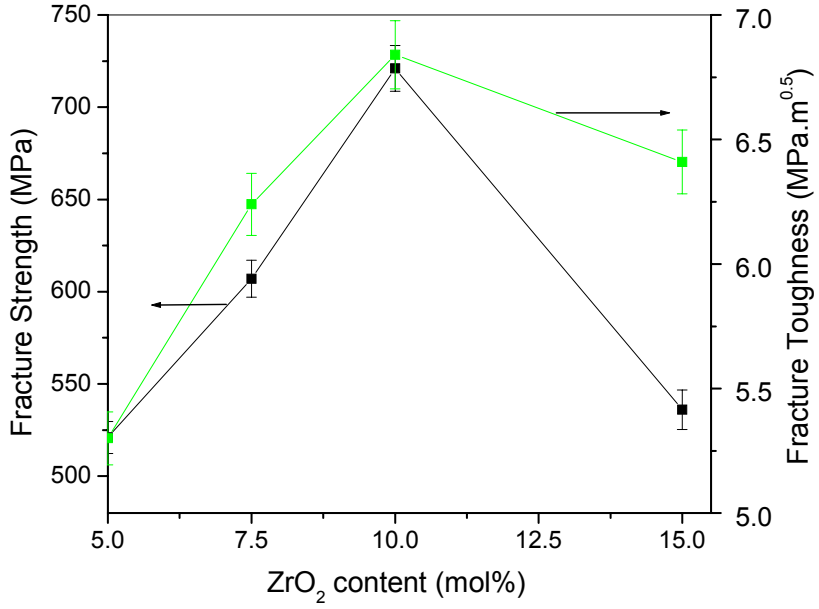

Fig.5.4.4. Flexural strength and fracture toughness as a function of ZrO_2 content

The fracture toughness as well as fracture strength increase linearly with increasing grain size/and interestingly it is limited up to 10mol% zirconia addition. The fracture toughness and strength of A3ZB could be observed 6.84MPa.$m^{1/2}$ and 721MPa respectively. Since the tetragonal zirconia grains do not undergo the stress-induced transformation to the monoclinic form when grain size is smaller than a critical size. The particle sizes lower than

the critical value does not affect the strength during fracture test. The reduction of size improves the bulk density but not the transformability of the tetragonal zirconia grains. Usually, the effect of grain size on toughness and strength in transformation-toughened ceramics is a complex phenomenon[129]. An increase in grain size improves the transformability (i.e., tetragonal to monoclinic), therefore, increasing toughness and strength. Microstructure reveals that the zirconia grain size increases with increasing zirconia content. The Zirconia particles (30-220 nm) in A3ZB are assisting to obtain the highest toughness and strength among these composites.

Depending on grain size, the spontaneous tetragonal to monoclinic transformation occurs in ZTA ceramics during cooling from the sintering temperature, leading to degradation in the mechanical properties of A4ZB specimens. After measurement of fracture strength, the fractured specimens are collected and simultaneously X-ray analysis was carried out. The comparative phase analysis of both the polished and fractured surface is presented in Table 5.4.2 and Fig. 5.4.5. The phase transformation behavior can be explained by XRD data.

The m-ZrO_2 phase increases with increase in ZrO_2 content and 12% m-ZrO_2 phase can be detected in composites containing 15mol% ZrO_2. The variation of t-ZrO_2 fraction in sintered and fractured specimens is shown in Fig. 5.4.5.

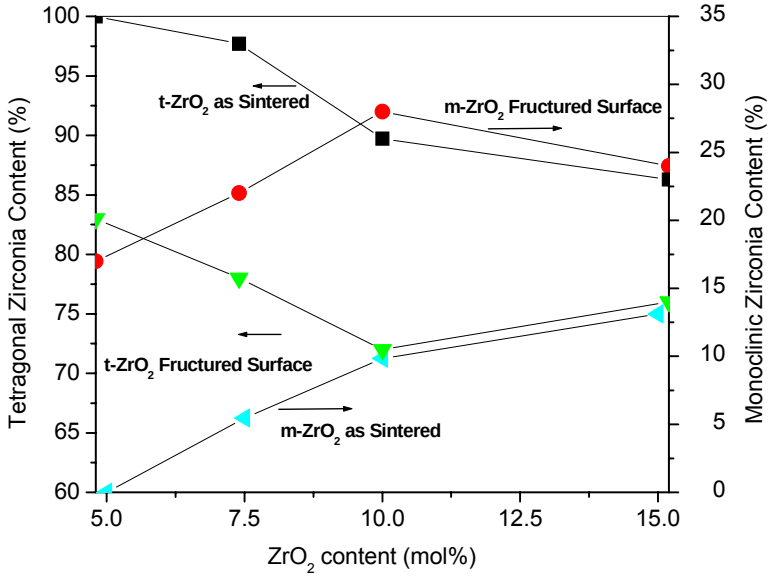

Fig.5.4.5. t-ZrO_2 and m-ZrO_2 content of sintered and fractured surfaces as a function of ZrO_2

The retention of t-ZrO_2 varies during fracture and t-ZrO_2 fraction decreases with increasing zirconia content. However, t-ZrO_2 retention becomes much easier to trigger the transformation to monoclinic. As a result, its contribution to transformation toughening

predominates although retention of m-ZrO_2 aids to microcrack toughening. However, fracture toughness value reduces abruptly when zirconia grain size is over a critical size and the ease of transformation accelerates above the critical size.

Table 5.4.2. Variation of phase content of polished and fractured surfaces

Identification	Tetragonal Phase Content (%)		Monoclinic Phase Content (%)	
	Polished	Fractured	Polished	Fractured
A1ZB	100	83	-	17
A2ZB	95	78	5	22
A3ZB	91	72	9	28
A4ZB	88	76	12	24

In sinter specimens, the monoclinic phase increases with the addition of zirconia, whereas under stress, the amount of monoclinic phase of fractured surface decreases under stress for the composite containing ZrO_2 more than 10mol%. The presence of large fraction of m-ZrO_2 in A4ZB is responsible for the strength degradation because it has been recognized that the increase in volume and shear strains accompanied by t → m phase transformation invariably cause microcracking.

To understand the effect of 4-point fracture strength on grain size of the sintered (1550^oC for 4h) specimens a detail fractographs were studied through scanning electron microscope. Fig. 5.4.6 shows the SEM images of Al_2O_3-xZrO_2 (x = 5, 7.5, 10 and 15 mol%) fractured surfaces after 4.point flexural strength carried out. Average alumina grain (gray contrast) sizes are 0.52μm and 0.35μm for A1ZB and A4ZB respectively are fairly uniform in each composite, which nearly resembles with the grain size of polished surfaces. ZrO_2 grains (white contrast) are homogeneously distributed throughout the Al_2O_3 matrix with a typical larger particle size, ($d_{average}$ [ZrO_2] varies from 150 nm in A1ZB to ~250 nm in A4ZB).

The present study shows that ZrO_2 grains are located at alumina triple points. However, the orientations of the ZrO_2 particles in ZTA are usually random. In the A1ZB material more than one of every two triple points are occupied by zirconia particles; two of

every three triple points are filled with zirconia particles in A2ZB; and zirconia particles are present in nearly all triple points for both A3ZB and A4ZB composites. The addition of zirconia is very effective in hindering the grain growth of alumina during sintering, even for the lowest zirconia content. The addition up to 10mol% ZrO_2 prevents grain growth without allowing the formation of zirconia agglomerates, which are very deleterious for the mechanical stability of the composite. However, the premature zirconia agglomeration can be observed in case of composites containing 15mol% ZrO_2. Fig. 5.4.6d reveals regular and almost spherical shaped grains with very small amount of isolated pockets of voids. A small fraction of intragranular zirconia particles can also be observed within the alumina matrix, which constrains the transformation.

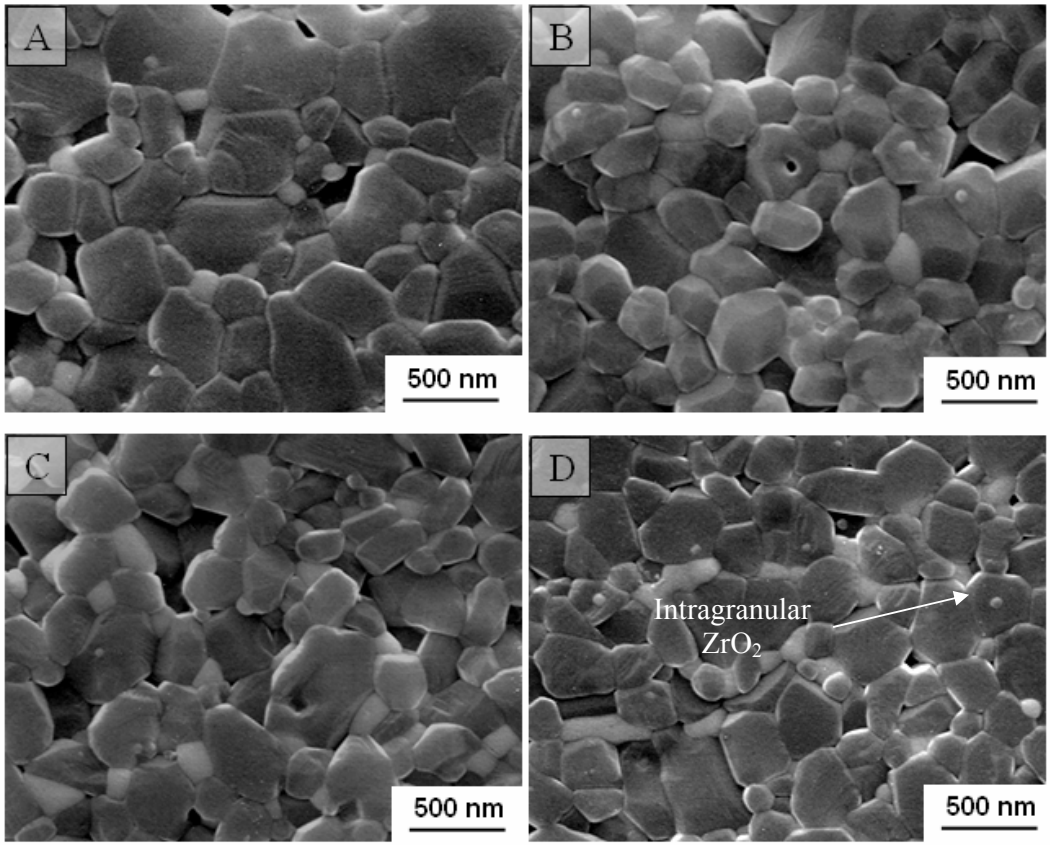

Fig.5.4.6. SEM microstructure of fracture surface of Al_2O_3–ZrO_2 composite sintered at 1550^0C for 4 h, represented as Al_2O_3-5ZrO_2 (a) Al_2O_3-7.5ZrO_2 (b) Al_2O_3-10ZrO_2 and (b) Al_2O_3-15ZrO_2 (d). The phases with gray and white contrast indicate Al_2O_3 and ZrO_2, respectively. The black irregular shape represents the corresponding pores in the sintered specimen.

The ZTA materials are fabricated by co-sintering from zirconia dispersed alumina synthesized precursor powders. This procedure results in an essentially isolated tetragonal ZrO_2 phase contained largely at three and four grain junctions. Such particles are thus strongly

irregular (Fig. 5.4.6C), as expected from dihedral angle considerations. When the sintering conditions allow appreciable grain growth of zirconia, ellipsoidal zirconia particles are present, and can be prevalent at low ZrO_2 concentration (e.g. ≤10 mol%). The angular ZrO_2 particles at the grain junctions have been observed to transform more readily than the intragranular particles, suggestive of an influence of the corners on the nucleation process.

From these data it can be noticed that the hardness varies from 17.6 to 15.3GPa with respect to zirconia content as well as elastic of modulus follows rule of mixture. The fracture toughness and fracture strength increases up to 10-mol% addition of zirconia and diminishes thereafter. However, previous researchers have reported that this indented fracture toughness values usually exhibit lower value than true K_{IC} of the composite[178]. Basu et. al[9] also used this same method to evaluate hardness and fracture toughness of WC-ZrO_2 composite material. The reported mechanical properties of WC-ZrO_2 composite are comparatively higher; and a typical composition of WC-6wt%ZrO_2 exhibits hardness of 22GPa and fracture toughness of ~5 MPa.$m^{1/2}$. However, Nawa et. al established that a small amount of TiO_2 addition and controlling sintering temperature can improve 17% fracture strength upto 1012MPa of 12Ce-TZP/30vol% $A1_2O_3$ composite[179]. High toughness of 10Ce-TZP/30 vol% Al_2O_3 (18.3 and 9.8MPa.$m^{1/2}$ by Indentation Fracture method and SEVNB method respectively) could also be achieved during transformation[180]. The mechanical properties of the studied materials can be explained on the basis of the intrinsic properties of the two components: Al_2O_3 and ZrO_2. The coefficient of thermal expansion (α) mismatch between the Al_2O_3 and ZrO_2 can alter the fracture properties of their composites[181]. The thermal expansion mismatch ($\alpha_{ZrO2}/\ \alpha_{Al2O3} > 1$) develop the hydrostatic tensile stress inside the dispersed particle (ZrO_2) and reduces the probability of plastic deformation, whereas, tensile fracture is possible along the dispersed phase. Freiman et. al reported that a sharp indenter can produce a compressive elastic zone, whereas rest of the area is tensile in nature[182]. Thus the radial cracks grow to their extension, as the indenter is unloaded, i.e. as the restraining elastic field is removed.

Anstis et. al measured the fracture toughness of ceramic material through the sharp-indenter method, where well-defined radial/median crack was measured under 40N load [152.] This technique has limitations on the effects of slow crack growth and possibilities of changing the original fracture toughness of the material by crack-microstructure interactions. The slow crack growth effect dominates to become an important factor for zirconia dispersed alumina composites[143]. Liang has shown that an addition of 5% of zirconia is very efficient in increasing crack resistance of alumina during slow crack growth, which is introduced by the

decrease of crack velocities by several orders[183]. Thus, depending on the indentation load and measurement of the cracks, the measured toughness is lower than the true K_{IC}, when using the Anstis formula. On the other hand, transformation toughening of second phase particle (ZrO_2) reduces the crack tip stress intensity and the crack velocity arresting within the zirconia particle. These zirconia particles may create many nanocracks along the sub-grain boundaries when a main crack tip approaches to this area and is expected to expand the crack size by frontal process zone (FPZ), which will improve the fracture toughness of the composite[184].

The martensitic transformation and frontal process zone are predominant mechanisms to increase the toughness of Al_2O_3-ZrO_2 nanocomposite. Hence, K_{Ic} changes with the addition of ZrO_2 may be rationalized by the relative predominance of the toughening mechanism, i.e. zirconia phase transformation. In the reported result it has been observed that the fracture toughness and fracture strength gradually increases upto 721MPa with addition of zirconia, with zirconia content of 10mol% and maximum grain size of ~220nm [34]. Moreover, the transformability is also expected to account for the reduction in hardness detected in the sintered ZTA composite, since hardness is inversely correlated with transformation easiness.

5.4.3. High Temperature Fracture Strength

Table 5.4.3 and Fig. 5.4.7 show the temperature dependence of the fracture strength (σ_f (T)) of different sintered specimens. For all ZTA composites, their strength decreases with increase in temperature. However, this decrease rate depends on the material composition and on the toughening mechanism, which operates on the material considered.

Table 5.4.3. High temperature fracture strength of sintered composites

Identification	Mechanical Properties	Temperature (^{0}C)					
		25	200	400	600	800	1000
A1ZB	Fracture Strength (GPa)	521	501	462	428	408	386
A3ZB		721	665	567	498	443	416
A4ZB		636	587	536	498	435	406

The strength of these composites varies within ~500 to 700MPa at room temperature, but a drastic drop of strength for A1ZB specimen at temperature above 600^{o}C. This

temperature (600°C) corresponds to the critical temperature, T_o, where transformation toughening is no longer effective and the free energy for transformation (ΔG_o), tends to zero. For A3ZB and A4ZB, where transformation toughening is the main toughening mechanism, we observed similar temperature dependence behavior is observed in the present work; but the critical temperature (T_o), seems to be much lower (about 500°C): This can be explained by the higher elastic modulus of the matrix. Another interesting point is the lack of plasticity observed during high-temperature bending test of ZTA composites. Since, zirconia particles distributed along Al_2O_3 grain boundaries prevents the grain-boundary sliding necessary for plastic deformation.

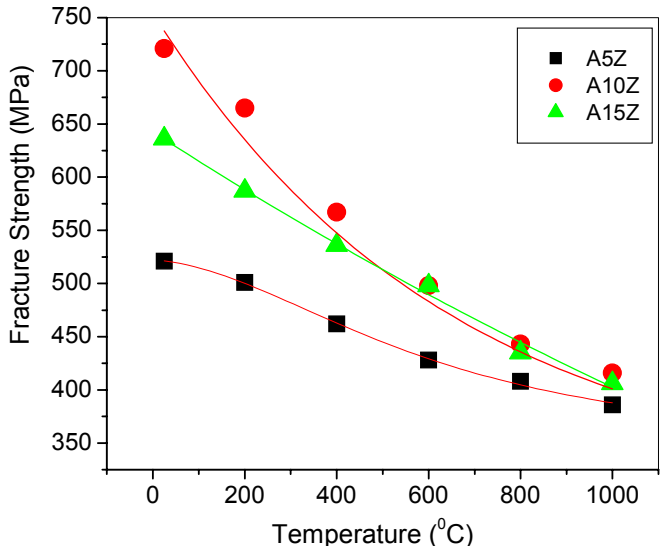

Fig.5.4.7. Temperature dependence fracture strength of ZTA.

5.4.4. Thermal Shock Resistance

The thermal shock resistance of ZTA nanocomposites fabricated from the sol-gel precursor powder is investigated by a water-quenching method. The samples are rapidly cooled by quenching them from T_{max} into water and experiment is repeated twice for each one. Fig. 5.4.8 shows the relative dependence of residual strength of the samples on the temperature difference of thermal shock. A rapid decrease in retained strength occurs around a critical temperature difference (ΔT_c) below which the original strength is retained. The strength reduces gradually with further increase in ΔT.

The dispersion of ZrO_2 increases the critical temperature difference (ΔT_c) of Al_2O_3, though the overall strength reduces significantly above 10mol% addition of ZrO_2. This behavior in ΔT_c can be discussed with the variations in mechanical and thermal properties of

the ZrO_2 dispersed ZTA composites as well as temperature difference dependence of the surface heat transfer coefficient at the water-ceramic interface during quenching. The fracture initiated through thermal shock has been given by [185]:

$$\Delta T_c = \sigma_f(1-\gamma)/ E\ \alpha.\beta \quad \text{and} \quad \beta = h_t\ x\ /\lambda$$

Where, ΔT_c = Critical temperature difference, σ_f = Flexural Strength, γ = Poisson's ration, E = Modulus of Elasticity, α = Thermal expansion coefficient. h_t = Heat transfer coefficient, λ = Thermal conductivity, x = Characteristic dimension.

A minimum temperature difference ΔT_c is required to initiate fracture. Below ΔT_c no change in crack length and/or strength is observed. Usually the fracture is initiated and strength decreases at ΔT_c. As the temperature difference of thermal shock increases beyond ΔT_c, crack growth occurs quasi-statically with decrease in strength. The decrease in retained strength up to 600^OC (ΔT) is marginal except in case of 5mol% zirconia. Retained strength of 5mol% zirconia reduces to about 40% of its original strength when quenched in water from 1200^OC. A3BZ and A4ZB composites lose their strength on quenching in water from 800 and 1000^OC, respectively. Based on the zirconia content, the retained strength varies from 25 to 40% in case of A3ZB and A1ZB respectively. The lowest retained strength is observed in case of 5mol% ZrO_2 samples. Critical temperature difference (ΔT_c) is in between 600 to 1000^OC for A3ZB. For Y-TZP/Al_2O_3 materials the drop in flexural strength is more than 50% at 1000^OC[170].

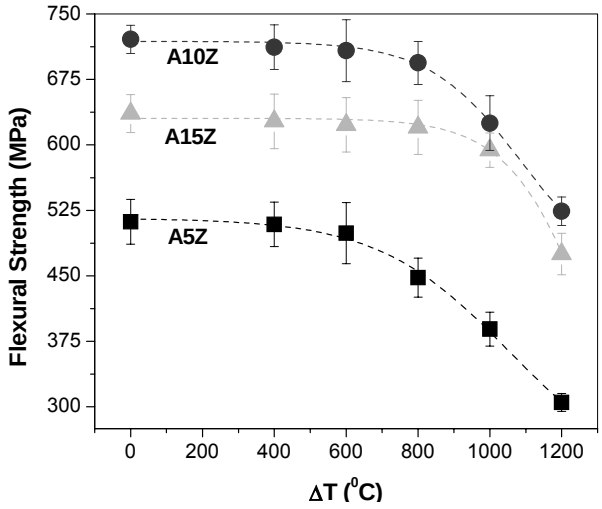

Fig.5.4.8. Plot of retained flexural strength versus (ΔT) thermal shock temperature for Al_2O_3 with variation of ZrO_2.

Thermal stress induced cracks dissipate their crack tip energy through stress induced phase transformation. It is expected that the crack propagates along the grain boundaries and

finally loose the energy to propagate while moving inside the grain. Therefore, stress induced phase transformation of monoclinic to tetragonal zirconia absorbs the energy of the crack tip thus arresting its propagation. The phase transformation of tetragonal to monoclinic zirconia reduces with increase in temperature.

This is presumably due to the reduction in differential free energy between the tetragonal and monoclinic phase. The disappearance of phase transformation strengthening and reduction in Young's Modulus contributes to the lowering of flexural strength at elevated temperature. In addition, thermal mismatch between two surfaces also enhances stresses and reduces mechanical properties beyond addition of 10 mol% ZrO_2.

5.4.5. Thermal Expansion Behavior

Since the thermally activated and stress induced reversible tetragonal to monoclinic transformation is always associated with 4–5% dilatation strain, a dilatometer study serves as an excellent tool in studying such transformations. In the starting material, the high temperature stable tetragonal phase is retained at room temperature during rapid cooling after sintering, and remains metastable in the microstructure of the nano-zirconia dispersed alumina composite.

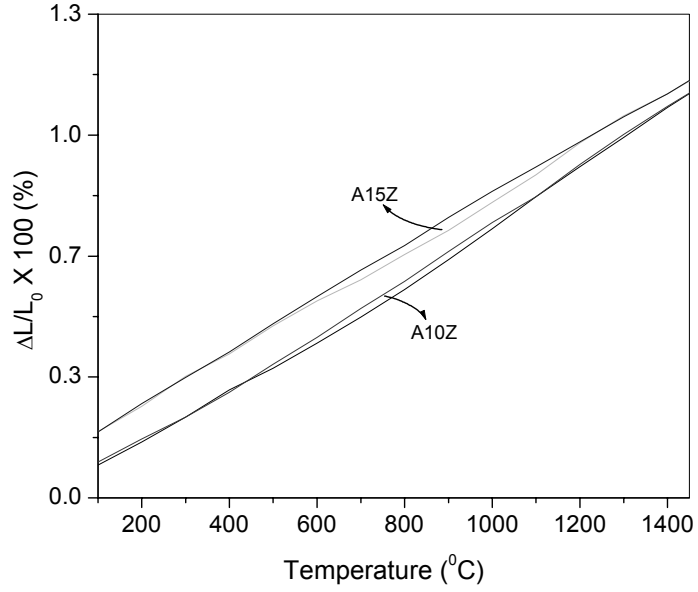

Fig.5.4.9. Thermal expansion behavior of Al_2O_3-xZrO_2 (where x = 10 and 15 mol%) composites.

The slope of the thermal expansion curve is basically the thermal expansion coefficient (α), and any appreciable change in slope can indicate a phase transition. To

understand this phenomenon, the dilatational measurement is carried out on the sintered materials (A3ZB and A4ZB) in the temperature range from room temperature (RT) to 1450^{o}C (Fig. 5.4.9).

The expansion in volume occurs linearly with temperature during heating and coefficient of thermal expansion in A3ZB can be encountered within the range of 8 to 9 x $10^{-6}K^{-1}$ at 1000^{O}C. However, the phase transformation during heating and cooling are different and consequently two curves are not identical until they coincide at temperature forming a thermal hysteresis loop. From the dilatation curve, it is proposed that the M_s temperature of A4ZB begins to alter at higher temperature (890^{o}C) compared to A3ZB (745^{o}C), because of larger inclusion size of ZrO_2 in A4ZB.

CHAPTER 6

6.0 CONCLUSIONS

The zirconia (5-15mol %) doped alumina precursor powder was synthesized through chemical route. The synthesized powder was characterized by DTA/TGA, XRD and IR spectroscopy. Finally, the particle characteristics of the synthesized powders were determined through BET surface area analyzer, particle size analyzer and transmission electron microscopy. The densification study was carried out with mixing of 5wt% uncalcined synthesized precursor as an additive of the corresponding batches. The sintered microstructures were analyzed through SEM and TEM studies. Subsequently, the thermo-mechanical properties were characterized systematically and analyzed with respect to zirconia addition. The overall experimental results and their analysis are represented as follows:

6.1. Thermal Analysis (DTA/TG) of Precursors

(a) Decomposition and crystallization of pseudoboehmite to γ-Al_2O_3 occurs in three-stages. The transition from γ-Al_2O_3 to α- Al_2O_3 followed the intermediate stage of θ-Al_2O_3 formation, whereas crystallization of t-ZrO_2 from $Zr(OH)_4$ occurs in single stage.

(b) The higher content of Zr^{4+} affects the transformation temperature of Al-hydroxide to α-Al_2O_3, which is increasing with addition of zirconia content.

6.2. Spectroscopy (FTIR) of Precursors

(a) The frequency of different vibrational modes of Al-OH and/or Zr-OH including the bending and stretching modes are altered due to change in the charge distribution among species.

(b) In the temperature range of 200- 400^oC the peaks are broadened due to overlapping of Al-O and Zr-O and individual peaks not able to detect, however, at higher temperature (1000^oC), peaks corresponding to Al-O and Zr-O can clearly be observed.

(c) It suggests the presence of both four and six coordinated Al while Zr is four coordinated. The number and intensity of M-OH and M-O bonds increase on increasing ZrO_2 content.

6.3. Microscopy (TEM) of Precursors

(a) The formation of amorphous material before crystallization is emphasized.

(b) Particles are exhibited different morphology; and show smooth, distinct and faceted surfaces at different temperature. The angularity and faceting of the crystal increases as diffusion predominate at high temperatures.

(c) Micrograph of a sample heated for two hour at 1000^{o}C shows the moderate particle growth. At this temperature, nearly all particles are spherical in nature in the range of 35-210nm and few particles are irregular and tiny clusters rather than spherical for 15mol % containing zirconia.

6.4. Phase Analysis of Precursors

(a) Broad peak of dried gel reveals the presence of bayerite with crystallite size of 5-20nm

(b) The XRD of hydrogel calcined at 200^{o}C for 2h shows the presence of both bayerite ($Al(OH)_3$) and boehmite (Al(O)OH).

(c) As temperature increases, the peak became more symmetric and narrower.

(d) X-ray diffractogram of powders calcined for 2h at 1000^{o}C show the presence of α-Al_2O_3, however, DTA could not find any such deformation because of any non-isothermal treatment at any peak temperatures.

(e) Usually α–Al_2O_3 completely crystallizes around 1200^{o}C, however, in the present study the lower crystallization temperature of α–Al_2O_3 could be related to the fine crystallite size and higher specific surface area.

(f) The m-ZrO_2, t-ZrO_2, δ-Al_2O_3, θ-Al_2O_3 and α-Al_2O_3 phases could be identified at 1000^{o}C in the synthesized precursor powder.

(g) Around 24% reduction of specific volume was detected during the phase transformation of boehmite (0.332cc/gm) to α-Al_2O_3 (0.251cc/g), which also presumably affects the formation of intraparticle porosity in the precursor.

(h) The major phases of Al_2O_3-15ZrO_2 (mol%) are t-ZrO_2 and α-Al_2O_3 present along with a small amount of m-ZrO_2 at 1400^{o}C, however, completion of phase transformation could be noticed at 1300^{o}C.

(i) The increase in m-ZrO_2 content at 1400^{o}C results from an increase in the grain size of zirconia, which induces partial t→m transformation during cooling.

(j) At 1400°C, m-ZrO_2 phase could not be detected below 10mol% ZrO_2 addition. The crystallite size gradually increases with increasing zirconia content as well as temperature, and it was 27nm for Al_2O_3-15ZrO_2 (mol%) at 1000°C.

6.5. Particle Size and Surface Area of Precursors

(a) Particle size analysis indicates a bimodal size distribution with both of the unagglomerated and agglomerated particles.

(b) The average particle size of Al_2O_3-5ZrO_2 (mol %) and Al_2O_3-15ZrO_2 (mol %) at 1000°C/2h in the calcined precursor is about 90 and 120nm respectively. The specific surface area of the powder decreases with zirconia content and minimum for highest zirconia content.

(c) An increase in crystal size leads to the t→m transformation, where, the free energy released during this transformation promotes crystal growth.

6.6. Densification Behavior of Compacts

(a) An influence of (5wt%) unclaicned powder on the solidification could be observed. The major shrinkage of green specimen at 970°C is associated with pore reduction and m → t zirconia transformation.

(b) At 1450°C, around 65% bulk density could be noticed during densification through dilatometer experiment, which is independent of ZrO_2 content.

(c) Entrapped porosity of higher zirconia containing specimens is nearly eliminated at 1550°C/4h but density decreases from 4.18 to 4.13 g/cc at 1600°C/4h because of faster grain growth and coarsening of zirconia.

(d) Differential Thermal Analysis reveals the alumina phase transformation shifts from 1160 to 1152°C with decreasing zirconia content; however, this phenomenon does not have any significant affect on the densification behavior of the sintered composites.

(e) Maximum ~98% densification could be noticed with addition of 5mol% ZrO_2 at 1550°C for 4h. However, for higher ZrO_2 content (15mol%), the relative density reduces to ~97% ρ_{th} at the same temperature, since m-ZrO_2 increases with temperature and zirconia content.

(f) A lower range of porosity (1.02 to 2.92%) could be noticed at 1600°C for 3h. An interesting observation can also be perceived that the apparent porosity increases with increase in zirconia content, although the average porosity decreases with temperature.

6.7. Microstructure and Phase Evaluation of Sinter Specimen

(a) Two kinds of zirconia grains is observed in the synthesized Al_2O_3-xZrO_2 (where x = 5, 7.5,10 and 15mol %) composite, faceted intergranular zirconia grains (mostly at the grain corners) and spherical intragranular zirconia grains. The large intergranular zirconia grains within alumina matrix may be related to the faster coarsening rate.

(b) The zirconia (Z) grain size increases with increasing zirconia content while alumina (A) grain size decreases, thus the grain size ratios d_A/d_Z vary between 4.35 for Al_2O_3-5ZrO_2 and 2.29 for Al_2O_3-15ZrO_2 (mol%). This relationship reveals that the control of the matrix grain size with variation of introduction of second-phase is possible.

(c) At 1550^oC, the obtained average ZrO_2 grain size demonstrates that the grain growth is rather limited at 4h holding period but increases dramatically as and when the sintering temperature and duration increases. However, the grain growth is very fast in this process above a certain critical temperature and the underlying mechanisms are thermally activated.

(d) The distribution of Zr is quite homogeneous as no part of the micrograph shows clustering of Zr-rich region. The Al is also quite homogenously distributed throughout the matrix of Al_2O_3-10ZrO_2 (mol%).

(e) Selected area electron diffraction of the Al_2O_3-15ZrO_2 (mol%) confirms the formation of lath of monoclinic within tetragonal zirconia, which may have detrimental effect on thermo-mechanical response.

6.8. Mechanical and Thermal Behavior of Sinter Compacts

(a) Hardness of the ZTA composite decreases (~17GPa to ~15GPa) with the addition of zirconia, however, higher amount of zirconia has an adverse affect on the hardness of the composites due to coarsening of the zirconia grains and formation of subsequent porosity.

(b) At 1550^oC, densification of the composites improves with reduction of pore volume fraction of the matrix and as a result of which the modulus of elasticity improves.

(c) The fracture toughness as well as fracture strength increases linearly with increase in grain size, interestingly it is limited up to 10mol% zirconia addition. The highest fracture toughness (6.84MPa.$m^{1/2}$) and fracture strength (721MPa) could be observed for Al_2O_3-10ZrO_2 specimen.

(d) The room temperature fracture strength of these composites vary within ~500 to 700MPa, but drastic decrease of strength for lowest zirconia containing specimen is observed above 600^{o}C, where transformation toughening is no longer effective.

(e) Retained strength of 5mol% zirconia reduces to about 40% of its original strength when quenched in water from 1200^{o}C. Based on the zirconia content; the retained strength varies from 25 to 40%.

(f) The disappearance of phase transformation strengthening and reduction in Young's Modulus contributes to the lowering of flexural strength at elevated temperature. In addition, thermal mismatch between two surfaces also enhances stresses and reduces mechanical properties beyond addition of 10mol% ZrO_2

(g) The expansion in volume occurs linearly with temperature during heating and coefficient of thermal expansion of Al_2O_3-10ZrO_2 can be encountered within the range of 8 to 9 x $10^{-6}K^{-1}$ at 1000^{o}C. The M_s temperature of Al_2O_3-15ZrO_2 (mol%) begins to alter at higher temperature (890^{o}C) compared to Al_2O_3-10ZrO_2 (745^{o}C), because of larger inclusion size of ZrO_2 in Al_2O_3-15ZrO_2.

CHAPTER 7

7.0. SCOPES FOR FUTURE WORKS

The detail analysis reveals that that the particle size of synthesized gel precursor powder is lower with compared to calcined powder. These fine nano-size particles have significant effect on sintering kinetics and mechanism of calcined powders. In the present work, only 5 wt% uncalcined powder of its corresponding batches is used. But the systematic densification study with the whole ranges of combination of uncalcined and calcined powder can provide the tailor made microstructure and other desired properties. Additionally, the determination of creep properties is an important aspect to develop excellent mechanical properties of these synthesized composites at high temperature. So, the scopes of the future works are proposed as:

a. Densification and Sintering Kinetics of combined uncalcined and calcined powders (for wide range of compositions).
b. Evaluation of the creep properties to understand the high temperature failure.

REFERENCES

1. Garvie RC, Critical Size Effects in Alumina-Zirconia Alloys, The Am. Ceram. Soc., Advanced in Ceramics, Vol 24: Science and Technology of Zirconia III, 55-69,(1988).
2. Porter DL, Heuer AH, Mechanism of Toughening Partially Stabilized Zirconia Ceramics (PSZ), J.Am.Ceram. Soc. 60 (3) 183-184,(1977).
3. Lange FF, Green DJ, Effect of Inclusion Size on the Retention of Tetragonal ZrO_2: Theory and Experiments, pp 184-201 in Advances in Ceramics, 3, Edited by Heuer AH and Hobbs LW, The American Ceramic Society, Columbus, OH,(1981).
4. Claussen N, Microstructural Design of Zirconia-Toughened Ceramics (ZTC), pp 325-52 in Advances in Ceramics, Vol.12. Edited by Claussen N, Rühle M and Heuer AH. The American Ceramic Society, Columbus, OH,((1984)).
5. Basu B, Toughening of Yttria-Stabilized tetragonal zirconia ceramics, International Matrial Reviews, 50 (4), 239-256 (18), (2005).
6. Curtis CE, Development of Zirconia resistant to Thermal Shock, J.Am.Ceram. Soc., 30 (6),180-96, (1947).
7. Creyke WEC, Sainsburg IEJ, Morrell R, Design with Non-Ductile materials, Applied Science Publishers, New York, (1982).
8. Green DJ, Critical microstructures for microcracking in Al_2O_3-ZrO_2 composites, J. Am.Ceram. Soc. 65, 610-614, (1982).
9. Basu B, Venkateswaran T, Sarkar D, Pressureless sintering and tribological properties of WC–ZrO_2 composites. J Eur Ceram Soc., 25 (9),1603–10, (2005).
10. Hannink RHJ, Swain MV, Progress in transformation toughening of ceramics. Annu. Rev. Mater. Sci., 24, 359–408, (1994).
11. Kobayashi S, Wada S, Strengthening of Si_3N_4 Ceramics by ZrO_2 additions, Adv. In Ceramics Vol. 24A, 127-32, (1988).
12. Garvie RC, Microstructure and Performance of an Alumina-Zirconia Tool Bit, J.Mater. Sci. Lett. 3(4), 315-18, (1984).
13. Messing GL, Kumagal M, Low-temperature sintering of seeding sol-gel-derived, ZrO_2-toughened Al_2O_3 composites, ibid, 72(1) 40-44, (1989).
14. Fegley B.JR., White P, Bowen HK, Preparation of zirconia-alumina powders by zirconium alkoxide hydrolysis. J. Am. Ceram. Soc., 68(2), (1985).

15. Sproson DW, Messing GL, Preparation of alumina-zirconia powders by evaporative decomposition of solutions. J. Am. Ceram. Soc., 67(5) C92-C93, (1984).
16. Hori S, Yoshimura M, Somiya S, $A1_2O_3$-ZrO_2 ceramics prepared from CVD powders. In Advances in Ceramics, Vol. 12, ed. Claussen N, Rühle M and Heuer AH. The American Ceramic Society, Columbus, OH, pp. 794-805, (1984).
17. Kagawa M, Kikuchi M, Syono Y, Nagae T, Stability of ultrafine tetragonal ZrO_2 coprecipiated with Al_2O_3 by the spray-ICP technique. J. Am.Ceram. Soc., 66 (11), 751-54,(1983).
18. Aksay IA, Lange FF, Davis BI, Uniformityof Al_2O_3-ZrO_2 composites by colloidal filtration. J.Am. Ceram. Soc., 66(10), C190-C92, (1983).
19. Yoshimura M, Kikugawa S, Somiya S, Alumina-zirconia fine powders prepared by hydrothermal oxidation, Yogyo-Kyokai-Shi, 91(4) 43-48, (1983).
20. Brinker CJ and Sherer GW, Sol-Gel Science, Academic Press, San Diego, (1990).
21. D.P. 220394 from 1907.
22. Dörre E, Hübner H, Alumina-Processing, Properties and Applications, Springer-Verlar, (1984).
23. Kingery WD, Bowen HK, Uhlmann DR, "Introduction of Ceramics", 2nd Edition, John Wiley & Sons, (1991).
24. Gitzen WH , Alumina as a ceramic material. Columbus: The American Ceramic Society, (1970).
25. Winchell H, Navigation in Crystallography. Bull. Geol. Soc. Am. 57 295-308, (1946).
26. Kronberg ML, Plastic deformation of single crystals of sapphire: basal slip and twining. Acta Met. 5 , 507-524, (1957).
27. Stumpf HC, Russell AS, Newsome JW, Tucker CM, Thermal Transformation of aluminas and alumina Hydrates, Industrial and Engineering Chemistry, 42,7, 1398-1403, (1950).
28. Tertain R, Papee D, Transformations thermiques et hydrothermiques de a'alumine, Journal ode chimie physique et de physico-chimie biologique, 55, 341-353, (1958).
29. Lange FF, Davies BI, Raleigh DO, Transformation strengthening of β"-Al_2O_3 with tetragonal ZrO2, J.Am. Ceram. Soc. 66 , C125-127, (1983).
30. Stevens R, Zirconia and Zirconia Ceramics, Magnesium Elektron Ltd, 1986, p18-19.
31. Mining Annual Review, p112, (1985).

32. Q. L. Ge, T. C. Lei, J. F. Mao and Y. Zhou; In situ transmission electron microscopy observations of the tetragonal-to-monoclinic phase transformation of ZrO_2 in Al_2O_3-ZrO_2 (2 mol % Y_2O_3) composites; J. Mat. Sc. Lett., 12 (1993) 819.
33. Lamas DG, Reca NEWD, Materials Letters, 41, 204-208, (1999).
34. Ge QL, Lei TC, Mao JF, Zhou Y, In situ transmission electron microscopy observations of the tetragonal-to-monoclinic phase transformation of ZrO_2 in Al_2O_3-ZrO_2 (2mol % Y_2O_3) composites; J. Mat. Sc. Lett., 12, 819, (1993).
35. R. H. J. Hannink, P. M. Kelly and B. C. Muddle, Transformation toughening in zirconia-containing ceramics; J. Am. Cer. Soc. 83 [3] (2000) 461-487.
36. Heuer AH, Chaim R, Lanteri V, The displacive cubic→tetragonal transformation in ZrO_2 alloys; Acta Mater. 35 (3), 661-666, (1987).
37. Mitra N, Vijayan K, Pramila BN, Biswas SK, Phase transformation induced by mechanical and chemical surface preparation of tetragonal zirconia polycrystals; J. Am. Cer. Soc. 76, 533-535, (1993).
38. Burke DP, Rainforth WM, Intermediate rhombohedral (r-ZrO_2) phase formation at the surface of sintered Y-TZP's; J. Mat. Sc. Lett. 16, 883-885, (1997).
39. Garvie RC, Hannink RH, Pascoe RT, Ceramic steel ?, Nature, 258,703, (1975).
40. Claussen N, J.Am. Ceram. Soc., 59, 49,(1976).
41. Evans AG, Heuer AH, Transformation toughening in Ceramics: Martensitic Transformation in crack tip stress fields, J.Am.Ceram. Soc., 63 (5-6) 241-48,(1981).
42. Green DJ, Lange FF, James MR, Residual Surface Stresses in Al_2O_3-ZrO_2 Composites, Advanced in Ceramics, Volume 12, Am Ceram Soc, Inc, Columbus, Ohio, p 240-250, (1984).
43. Lange FF, Evans AG, Erosive Damage depth in Ceramics: A study on Metastable Tetragonal Zirconia, J.Am.Ceram.Soc. 62 (1-2) 62-65,(1979).
44. Pascoe RI, Garvie RC, Ceramic Microstrucutres 1976, ed Fulrath RM and Pask JA, Westview Press, Boulder, pp 774-785, (1977).
45. Lange FF, J.Mat.Sci. 17 (1-4) 225-255,(1982).
46. McMeeking RM, Evans AG, Mechanics of transformation-toughening in brittle materials, J.Am. Ceram. Soc. 65 (5) 242,(1982).
47. Claussen N, Rühle M, Design of Transformation Toughened Ceramics, Advances in Ceramics, 3, science and Technology of Zirconia, The American Ceramic Society, Columbus, OH,1981, p-137.

48. Mondal B, Chattopadhyay AB, Virkar A, Paul A, Development and. Performance of Zirconia-Toughened Alumina Ceramic Tools. Wear, 156,. 365–383, (1992).
49. Aza AHD, Chevalier J, Fantozzi G, Schehl M, Torrecillas R, Crack growth resistance of alumina, zirconia and zirconia toughened alumina ceramics for joint prostheses, Biomaterials 23 , 937–945, (2002).
50. Ezugwu EO, Bonney J, Silva RB, Machado AR, Evaluation of the Performance of Different Nano-Ceramic Tool Grades when Machining Nickel-Base, Inconel 718, Alloy, J. of the Braz. Soc. of Mech. Sci. & Eng. 12- 16 , 26 (1), (2004).
51. Bansal GK, Heuer AH., Precipitation in partially stabilized Zirconia, J.Am. Ceram. Soc., 63 (5-6) 235-40 (1975).
52. Wheat TA, Microstructure of Thermal Shock Resistant Zirconia, J. Can. Ceram. Soc. 44, 7-15, (1975).
53. Green DJ. Maki DR, Nicholson PS, Microstructure Development in Partially Stabilized Zirconia in the system CaO-ZrO_2, J. Am. Ceram. Soc., 57 (3) 1136-9 (1974).
54. Sheikh El, Nicholson PS, Thermal Shock Structures in a PSZ in the system CaO-ZrO_2, J. Am. Ceram. Soc., 57 (1) 19-22 (1974).
55. Green DJ, Nicholson PS, Embury JD, Fracture Toughness of a partially stabilized in the system CaO-ZrO_2, J. Am. Ceram. Soc., 56 (12) 619-23 (1973).
56. Garvie RC, Nicholson PS, Structure and Thermomechanical Properties of partially stabilized in the system CaO-ZrO_2, J. Am. Ceram. Soc., 55 (4) 152-7 (1972).
57. Garvie RC, Hannink RHJ, Urbani C, Ceramurgia 6(1) 19 (1980).
58. Gulati ST, Helfinstone JD, Davis AD, Determination of some useful properties of Partially stabilized Zirconia and their application to Extrusion Dies, Am. Ceram. Soc. Bull. 59 (2) 211 (1980).
59. Gulati ST, Helfinstone JD, Dynamic Fatigue of three partially stabilized Zirconia Am. Ceram. Soc. Bull. 50 (6) 646 (1980).
60. Porter DL, Heuer AH, Microstructural Development in MgO-Partially stabilized ZrO_2, J. Am. Ceram. Soc., 62 (5-6) 298-305 (1979).
61. Hannink RHJ, Growth Morphology of the tetragonal phase in Partially stabilized ZrO_2, J. Mat. Sc. 13, 2487-96 (1978).
62. Garvie RC, Hannink RHJ, Hughan RR, Strong and Partially Stabilized Zirconia Ceramics, J. Aust. Ceram. Soc. 13 (1) 8-11.

63. Gupta TK, Ultrafine Y-PSZ powders from different routes, J. Mat. Sc. 12, 2421-26, (1977).
64. Chen M, Giachello A, Martinengo PC, Ultrafine Y-PSZ powders from different routes, Rev. Int. Hautes. Temp. Refract. Fr. 22/ 191-202 (1985).
65. Pujari VK, Javad I, Effect of Densification conditions on the stabilization of tetragonal phase in Zirconia, J. Am. Ceram. Soc. 68 (9) C 242-3 (1985).
66. Heuer AH, Thermal Shock Resistance of MgO- PSZ, J. Mat. Sc., 20 (10) 342-7 ((1985))
67. Matsumoto RLK, Strength Recovery in Degraded Y-TZP, J. Am. Ceram. Soc. 68 (8) C 213 (1985).
68. Hannink RHJ, Murray MJ, Marmach M, Magnesia Partially Stabilized Zirconia (Mg-PSZ) as wear resistant materials, Wear, 181-86, (1983).
69. Lanteri V, Heuer AH, Mitchell TE, Tetragonal phase in the system ZrO_2-Y_2O_3 , Adv. In Ceramics Vol. 12, pp 118-30.
70. Tsukuma K, Kabota Y, Nobugai, Thermal and Mechanical properties of Y_2O_3 – Partially stabilized Zirconia, J. Ceram. Soc. Japan, 92 (5) 233-41 (1984).
71. Hannink RHJ, Johnston KA, Pascoe RR, Garvie RC, Microstructural changes during isothermal ageing of a Calcia partially stabilized Zirconia alloy, Adv. In Ceramics, 3, 116-36.
72. Rühle M, Claussen N, Heuer AH, Microstructural Studies of Y_2O_3 –containing Tetragonal ZrO_2 polycrystals (T-TZP), Adv. In Ceramics, Vol. 12, pp 352-370.
73. Matsshita M, Soma T, Oda I, Effect of Microstructure on the strength of Y-TZP components, Adv. In Ceramics, Vol. 12, pp 371-81.
74. Tsukuma K, Kubota Y, Tsukidate T, Thermal And Mechanical Properties of Y_2O_3 – Stabilizes Tetragonal Zirconia Polycrystals, Adv. In Ceramics Vol. 12 pp 382-90.
75. Garvie RC, Hughan RG, Pascoe RR, Strengthening of Lime-Stabilised Zirconia by Post Sintering Heat Treatment, Mat. Sc. Research, Vol. 11, pp 263-74.
76. Hannink RHJ, Garvie RC, Sub-eutectoid aged Mg-PSZ alloy with enhanced thermal up-shock resistance, J. Mat. Sc.17, 2637-43, (1982).
77. Bhathena N, Hoagland RG, Meyrick G, Effects of particle distribution on transformation toughening in MgO-PSZ, J. Am. Ceram. Soc. 67, (2) 799-805 (1984).
78. Schmauder S, Schubert H, Significance of internal stresses for the Martensitic transformation in the Yttria-stabilised Tetragonal Zirconia Polycrystals during Degradation, J. Am. Ceram. Soc., 69 (7) 534-40 (1986).

79. Masaki T, Mechanical properties of Toughened ZrO_2- Y_2O_3 (ceramics), J. Am. Ceram. Soc., 69 (8) 638-40 (1986).
80. Masaki T, Microstructure of High Toughened Y-TZP, J. Ceram. Soc. Japan, 94 (8) 716-20 (1986).
81. Ashizuka M, Thermal Shock behavior of Y-PSZ., J. Am. Ceram. Soc., 94, (6) 577--82 (1986).
82. Gross M, Swain MV, Mechanical Properties and Microstructure of sintered and Hot Isostatically Pressed Y-PSZ, J. Aust. Ceram. Soc., 22 (1) 4-12 (1986).
83. Drennan J, Effect of SrO Additions on the Grain Boundary Microstructure and Mechanical Properties of Mg-PSZ., J. Am. Ceram. Soc., 69(7)541-46 (1986).
84. Hughan RR, Precipitation during controlled cooling of Mg-PSZ, J. Am. Ceram. Soc., 69 (7) 556-83 (1986).
85. Swain MV, Grain Size dependence of Toughness and Transformability of 2 mol% YTZP, J. Mat. Sc. Lett. 5 (11) 1159-62 (1986).
86. Lange FF, Degradation during ageing of Transformation-Toughened ZrO_2-Y_2O_3, J. Am. Ceram. Soc., 69 (3) 237-40(1986).
87. Masaki T, Mechanical properties of Y-PSZ after ageing at low temperature, Int. J. High. Technol. Ceram., 2 (2) 85-98 (1986).
88. Sato T, Shimada M, Control of the Tetragonal-to-Monoclinic phase transformation of Yttria-doped tetragonal ZrO_2 polycrystals by annealing in water, Br. Ceram. Proc. 37, pp 151-8 (1986).
89. Whalen PJ, Reidinger F, Antrim RF, Prevention of low temperature Surface transformation by Surface Recrystallisation in Yttria-doped Tetragonal Zirconia, J. Am. Ceram. Soc. 72 (2) 319-21 (1989).
90. Lepisto T., Lintula PV, Mentyle AT, TZP Ceramics in humid conditions at 150^0C, Ceram. Engg. Sc. Proc., 9 (9-10) 1517-24 (1988).
91. Druschitz AP, Schroth JG, Hot isostatic pressing of a presintered Zirconia, J. Am. Ceram. Soc. 72 (9) 1591-7 (1989).
92. Lu H, Bow J, Effect of MgO addition on the microstructure development of 3- mol% Y_2O_3-ZrO_2 J. Aust. Ceram. Soc. 72 (2) 220-31 (1989).
93. Ruiz L, Ready MJ, Effect of Heat treatment on Grain Size, Phase Assemblage and Mechanical Properties of 3mol% YTZP, J. Am. Ceram. Soc. 79 (9) 2331-40 (1996).

94. Hwang S, Chen I., Grain Size Control of Tetragonal Zirconia Polycrystals using the Space Charge Concept, J. Am. Ceram. Soc. 73 (11) 3269-77 (1990).
95. Wang J, Stevens R, Surface Transformation and Toughening of TZP, Br. Ceram. Proc. 42. pp 67-68 (1989).
96. Pan LS, Horibe S, An in-situ investigation on the critical phase transformation stress of tetragonal zirconia polycrystalline ceramics, J. Mater. Sci. 31, 6523-27, (1996).
97. Ishitsuka M, Sato T, Endo T, Raman Microprobe Spectroscopic Studies on the Thermal Shock Fracture of ZrO_2 based ceramics, J. Mat. Sc. Lett. 8 (6) 638-40, (1989).
98. Tikare V, Heuer AH., Temperature-dependent Indentation Behaviour of Transformation Toughened Zirconia based Ceramics, J. Am. Ceram. Soc. 74 (3) 593-7 (1991).
99. Gao L, Yen TS, Guo JO, Influence of ZrO_2 particle size on toughening in Hot pressed Y-TZP, Adv. In Ceramics, 24 A, pp 405-14 (1989).
100. Robert LJ, Richard FR, Derek M, Scandia, yttria-stabilized zirconia for thermal barrier coatings, Surface and Coatings Technology 82, 70-76, (1996).
101. Mehner A, Westkamp HK, Hoffmann F, Mayr P, Crystallization and residual stress formation of sol-gel-derived zirconia films Thin Solid Films 308–309, 363–368, (1997).
102. Hare'l G, Ravi BG, Chaim R, Effects of solvent and agitation on microstructural characteristics of sol–gel derived nanocrystalline Y-TZP powders, Mater. Let 39 63–68, (1999).
103. Bokhimi X, Morales A, Novaro O, Portilla M, Lopez T, Tzompantzi F, Gomez R, Tetragonal Nanophase Stabilization in Nondoped Sol–Gel Zirconia Prepared with Different Hydrolysis Catalysts, J Solid State Chem., 135, 28-35 (1998).
104. Mustafa EAA, Ca-PSZ prepared via polymeric sol-gel route, Ceram. Inter., 26, 215-220, (2000).
105. Wang JA, Valenzuela MA, Salmones J, Vázquez A, Garc´ıa-Ruiz A, Bokhimi X, Comparative study of nanocrystalline zirconia prepared by precipitation and sol–gel methods, Catalysis Today, 68, 21–30, (2001).
106. Chen Y, Liu W, Preparation and tribological properties of sol-gel zirconia thin films stabilized with ceria, Mater. Lett., 55, 407– 413, (2002).
107. Xu H, Qin DH, Yang Z, Li HL, Fabrication and characterization of highly ordered zirconia nano-wire arrays by sol–gel template method, Materials Chemistry and Physics 80, 524–528, (2003).

108. Rambo CR, Cao J, Sieber H, Preparation and properties of highly porous, biomorphic YSZ ceramics, Materials Chemistry and Physics 87, 345–352, (2004).
109. Heuer AH, Claussen N, Kriven WM, Ruhle M, Stability of Tetragonal ZrO_2 Particles in Ceramic Matrices, J. Am. Ceram. Soc. 65 (12) 642-9 (1985).
110. Tsukuma K, Ueda K, Matshushita K, Shimada M, High Temperature Strength and Fracture toughness of Y_2O_3-Partially Stabilised ZrO_2/Al_2O_3 composites, J. Am. Ceram. Soc. 68 (2) C 56-58, (1985).
111. Tsukuma K, Ueda K, Shimada M, Strength and Fracture toughness of Hot isostatic–pressed Y_2O_3 stabilized ZrO_2-Al_2O_3 composites, J. Am. Ceram. Soc. 68 (2) C4-6,(1985).
112. Mazerolle L, Mitchell D, Porter R, Microstructure and Mechanical Behaviour of Al_2O_3-ZrO_2 (Y_2O_3), Sci. of Ceram., 13, 335-38, (1985).
113. Hori S, Kurita R, Yoshimura M, Somiya S, Influence of Small Zirconia Additions on the Microstructure and Mechanical properties of Al_2O_3, Adv. In Ceramics, 24A pp 423-29.
114. Rytkonen T, Keskine K, Lintula P, Fabrication and Properties of Uniaxially and Hot Pressed Al_2O_3-ZrO_2 Composites, Ceram. Engg. Sci. Proc., 10 (9-10) 1449-61, (1989).
115. Rajendran S, Swain MV, Rossell HJ, Mechanical Properties and Microstructure of Co-Precipitation derived Tetragonal Y_2O_3- ZrO_2-Al_2O_3, J. Mat. Sc. 23 (5).
116. Alexander KB, Becher PF, Waters SB, Bleir A, Grain Growth Kinetics in Alumina-Zirconia Composites, J. Am. Ceram. Soc., 77, (4) 939-46, (1994).
117. Claussen N, Jahn J, Mechanical Properties of Sintered, In-situ reacted Mullite-Zirconia Composites, J. Am. Ceram. Soc. 63 (3) 228-32 (1980).
118. White P, Bowen HK, Fegley B, Preparation of Zirconia-alumina Ceramics from Narrow-sized Powders, Adv. In Ceramics, Vol. 24 A, pp 301-8 (1988).
119. Grahtwohl G, Liu T, Strengthening of Zirconiua Alumina during Cyclic Fatigue Testing, J. Am. Ceram. Soc. 72 (10) (1988)-90 (1989).
120. Park SS, Meek TT, Characterization of ZrO_2-Al_2O_3 composites using 2.45GHz radiation, Ceram. Engg. Sci. Proc. 11 (9-11) 1395-1404 (1990).
121. Srikrishna K, Thomas G, Moya JS, Sintering additives for mullite/ Zirconia Composites, Adv. In Ceramics, Vol. 24 A, pp 277-86,(1988).
122. Tsubakino H, Fujiwara T, Yamamoto A, Ioku S, Improvement of mechanical properties by the formation of a grain boundary phase in ZrO_2-3mol%Y_2O_3-Al_2O_3 ceramics, Ceram. Trans., 44, 265-74 (1994).

123. Kibbel BW, Heuer AH, Ripening of Inter and Intragranular ZrO_2 particles in ZrO_2-Toughened Al_2O_3, Adv. In Ceramics, Vol. 12, 415-24 (1988).
124. Oh KS, Kim DY, Chi SJ, Generation of Crack like Voids during Sintering of Al_2O_3-10 ZrO_2 Ceramics and their prevention with low sintering pressure (2MPa), J. Am. Ceram. Soc. 79 (6) 1723-5, (1996).
125. Wallace JS, Petzow G, Claussen N, Microstructure and Property development of In-situ Reacted Mullite- ZrO_2 Composites, Adv. In Ceramics, 12, 436-42 (1985).
126. Porter GD, Henney JW, The Microstructure and Mechanical Properties of Mullite-Zirconia Composites, Tr. & J. Brit. Ceram. Soc., 83 (2) 69-72 (1984).
127. Rincon JM, Moya J, Microstructural Study of Toughened ZrO_2/Mullite Ceramic Composites obtained by Reaction sintering with TiO_2 additions, Tr. & J. Brit. Ceram. Soc., 86 (6) 201-6 (1986).
128. Kladnig WF, Fracture Behavior of Duplex $Al_2O_3 – ZrO_2$ Ceramics, Materials Chemistry and Physics, 18 ,18 1-191, (1987).
129. Orange G, Fantozzi G, Homerin P, Thevenot F, Leriche A, Thermomechanical Properties of Zirconia-Toughened Alumina Materials: Effect of Microstructure and Temperature on Toughening Mechanisms, Advances in Ceramics, Vol24B, Science and Technology of Zirconia III, Edited by Somiya A, Yamamoto N, Yanagida H, The American Ceramic Society, Inc. Westerville, OH, (1988)., p-1075-82.
130. Leriche A, Moortgat G, Cambier F, Homerin P, Thevenot F, Orange G, Fantozzi G, Preparation Toughened (ZTA). Part I: Material Preparation. Characterization of Microstructure and Characterization of Ceramic for Thermomechanical, J Eur Ceram Soci., 9,169-176, (1992).
131. Lee HY, Riehemann W, Mordike BL, Sintering of Nanocrystalline ZrO_2 Toughened Alumina (ZTA) and Zirconia, J Eur Ceram Soci., 10, 245-253, (1992).
132. Chen CC, F S Yen & C Y Huang, Aging Effects on the Characteristics and Sintering Behavior of Coprecipitated Al_2O_3-ZrO_2 Powders Ceramics International 211 (1994) 379-384
133. Srdie V, L. Radonjie L, Interactions in the Sol-Gel Processing ofAlumina-Zirconia Composites, Journal of the European Ceramic Society 14, 237-244, (1994).
134. Balasubramanian M, Malhotra SK, Gokularathnam HCV, Sintering and mechanical properties of sol-gel derived alumina-zirconia composites, J Mater Process Tech. 67, 67 70, (1997).

135. Bhattacharya S, Jakus K, Hot Pressing of Annular Alumina–Zirconia Composites, J. Am. Ceram. Soc., 81 [3] 460–64 (1998).
136. Jayaseelan D, Nishikawa T, Awaji H, Gnanam FD, Pressureless sintering of sol-gel derived alumina–zirconia composites , Mater Sci and Engg., A256 265–270, (1998).
137. Jayaseelan D, Rani DA, Nishikawa T, Awaji H, Gnanam FD, Powder characteristics, sintering behavior and microstructure of sol-gel derived ZTA composites, J Euro Ceram Soci., 20, 267-275, (2000).
138. Viswanath RN, Ramasamy S, Sol-Gel Derived YSTZ-Al_2O_3 and YSTZ-Al_2O_3-SiO_2, Nanocomposites Nanosmtctured Materials, Vol. 12, pp. 1085-1088, (1999).
139. Ferkel H, Hellmig RJ, Effect of Nanopowder Deagglomeration on Thedensities of Nanocrystalline Ceramic Green bodies and their Sintering Behavior**,** Nano-Structured Materials, 11(5), 617–622, (1999).
140. Kerkwijk B, Winnubst AJA, Verweij H, Mulder EJ, Metselaar HSC, Schipper DJ, Tribological properties of nanoscale alumina–zirconia composites, Wear 225–229, 1293–1302 (1999).
141. Tang JM, Uehara M, Maeda H, Hojo J, Nakagawa Z, Enomoto N, Process study on alumina-zirconia nanocomposite via ammonolysis route, J Ceram Process Research, 1(2) 88-91, (2000).
142. Guo R, Guo D, Zhao D, Yang Z, Chen Y, Low temperature ageing in water vapor and mechanical properties of ZTA ceramics, Mater Let., 56 , 1014–1018, (2002).
143. Antonio H, Aza D, Chevalier J, Fantozzi G, Schehl M, Torrecillas R, Slow-Crack-Growth Behavior of Zirconia-Toughened Alumina Ceramics Processed by Different Methods, J. Am. Ceram. Soc., 86 (1) 115–20 (2003).
144. Huang XW, Wang SW, Huang XX, Microstructure and mechanical properties of ZTA fabricated by liquid phase sintering Ceramics International 29, 765–769, (2003).
145. Casellas D, Nagl MM, Llanes L, Anglada M, Fracture toughness of alumina and ZTA ceramics: microstructural coarsening effects, J Mater Process Tech., 143–144 148–152, (2003).
146. Quintina AP, Bergera MH, Bunsella AR, Kayab C, Butler EG, Woottonc A, Lewis MH, Processing and structures of bi-phase oxide ceramic filaments, Journal of the European Ceramic Society 24,101–110, (2004).
147. Dakskobler A, Kosmac T, The preparation and properties of Al_2O_3–ZrO_2 composites with corrugated microstructures, J Euro Ceram Soc., 24,3351–3357,(2004).

148. Aruna ST, Rajam KS, Mixture of fuels approach for the solution combustion synthesis of Al_2O_3–ZrO_2 nanocomposite, Mater Research Bulletin 39,157–167, (2004).
149. Cullity BD, Elements of X-Ray Diffraction, 2nd Ed, Addision-Wesley. INC,(1978).
150. Brunauer, Emmet, Teller, J Am. Chem. Soci., 60, 309, (1938).
151. Lawn BR, Swain MV, Microfracture Beneath Point Indentation in Brittle Solids, ibid, [1] 113-32.
152. Anstis GR, Chantikul P, Lawn BR, Marshall DB, Acritical evaluation of indentation techniques for measuring fracturetoughness: I. Direct crack measurements. J. Am. Cer. Soc., 64, 533, (1981).
153. Levin I, Brandon D, Metastable Alumina Polymorphs: Crystal Structures and Transition Sequences, J. Am. Ceram. Soc., 81 (8) 1995-2012 (1998).
154. Bhattacharyya S, Bharati S, Pratihar SK, Sinha RK, Behera RC, Ganguly RI, Sintering Behavior of Al_2O_3-ZrO_2 Microcomposites Prepared by a Combined Gel-Precipitation Route, Trans. Indian Ceram Soci., 62 (1), 18-21, (2003).
155. Lippens BC,Boer JHD, Study of Phase Transformation during Calcination of Aluminum hydroxides by Selected Area Electron Diffraction, Acta Crystallogra, 17, 1312 (1964).
156. Levin I, Gemming T, Brandon DG, Some metastable phases and transient Stages of Transformation in Alumina, Phys. Status Solids A , 166 [1] 197-218 (1998).
157. Willard HH, Merritt LL, Dean JA, Instrumental Methods of Analysis, Van Nostrand, East West Press, (1962).
158. Guo GY, Chen YL, High-quality zirconia powder resulting from the attempted separation of acetic acid from acrylic acid with zirconium oxychloride, J. Mater. Chem., 11, 1283–1287,(2001).
159. Chen SG, Yin YS, Wang DP, Experimental and theoretical investigation on the correlation between aqueous precursors structure and crystalline phases of zirconia, J. Molecular Structure, 690,181-187, (2004).
160. Colomban Ph, Structure of oxide gels and glasses by infrared and Raman scattering, J. Mater. Sci. 24, 3002–3010, (1989).
161. Low M, McPherson R, Crystallization of gel-derived alumina and alumina–zirconia ceramics, J. Mater. Sci. 24, 892– 898, (1989).
162. Livage J, Doi K, Mazieres C, Nature and thermal evolution of amorphous hydrated zirconium oxide, J.Am.Ceram.Soc. 51 [6] 349-353 (1968).

163. Srinivasn R, Davis BH, Cavin OB, Hubbard CR, Crystallization and phase transformation process in zirconia: an in situ high-temperature X-ray diffraction study, J.Am. Ceram.Soc. 75 (5)1217-1222 (1992).
164. Tseng TY, Lin CC, Liaw JT, Phase Transformation of Gel-Derived Magnesia Partially Stabilized Zirconias, J.Mater. Sci. 22, 965-972 (1987).
165. Mamott GT, Barnes P, Tarling SE, Jones SJ, Norman CJ, Dynamic studies of zirconia crystallization, J.Mater. Sci. 26, 4054-4061 (1991).
166. Rahaman MN, Ceramic Processing and Sintering, Marcel Dekker, Inc, New York ed. pp 115, (1995).
167. Wltek SR, Bulter EP, Zirconia particle coarsening and the effect of zirconia additions on the mechanical properties of certain commercial alumina, ibid, 69(7), 610-614, (1982).
168. Tuan WH, Brook RJ, Sintering of heterogeneous ceramic compacts: part2 ZrO_2–Al_2O_3, J. Mater. Sci. 24 (6), 1953–1958, (1989).
169. Basu B, Lee JH, Kim DY, Development of WC- ZrO_2 Nanocomposites by Spark Plasma Sintering , J. Am. Cer. Soc., 87 (2) 317-319, (2004).
170. Wang J, Stevens R, Review of Zirconia Toughened Alumina (ZTA) Ceramics, J Mater Sci, 24 (10) 3421-40, (1989).
171. Kim BN, Hiraga K, Morita K, Sakka Y, A high-strain-rate superplastic ceramic, Nature 413, 288-291, (2001).
172. Lange FF, Hirlinger MM, Grain Growth. in Two-Phase Ceramics. A1203 Inclusions in ZrO_2, J. Am. Ceram. SOC., 70, (11), 827-30 (1987).
173. Hellman P, Hillert M, Scandanavian J Metallurgy, 4, 211, (1975).
174. Lawn BR, Marshall DB, Hardness, Toughness and Brittleness: An Indentation Analysis, J.Am.Ceram.Soc., 62 [7-8] 347-50 (1979).
175. Hall EO, Proc. Phys. Soc. London Sect. B 64, 747(1951).
176. Petch NJ, J. Iron Steel Inst. 173, 25 (1953).
177. Khaund AK, Nicholson PS., Fracture of a brittle composite: Influence of elastic mismatch and interfacial bonding. J. Mater. Sci., 15,177, (1980).
178. Evans AG, Charles EA, Fracture Toughness Determination by Indentation, J.Am. Ceram. Soc., 59 (7-8) 371-72 (1976).
179. Nawa M, Bamba N, Sekinob T and Niiharab K, The Effect of TiO_2 Addition on Strengthening and Toughening in Intragranular Type12Ce-TZP/Al_2O_3 Nanocomposites, J Euro Ceram Soci. 18, 209-219, (1998).

180. Nawa M, Nakamoto S, Sekino T and Niihara K, Tough and Strong Ce -TZP/Alumina Nanocomposites Doped with Titania, Ceramics International 24, 497-506, (1998).
181. Niihara K, New design concept of structural ceramics—ceramic nanocomposites. Ceram. Soc. Jpn. The Centennial Memorial Issue, 99, 974– 981, (1991).
182. Freiman SW, Fracture Mechanics Applied to Brittle Materials, ASTM Spec.Tech Publ., No. 678, Philadelphia (1979).
183. Liang K. Contribution a` l'e´tude des me´canismes de fissuration des ce´ramiques de type oxyde. PhD thesis, INSA de Lyon, France, (1990).
184. Awaji H, Choi SM, Yagi E, Mechanisms of toughening and strengthening in ceramic based Nanocomposites, Mechanics of Materials 34, 411–422, (2002).
185. Barsoum MW, Fundamentals of Ceramics, McGRAW-HILL International Editions, (1997).

RECENT INTERNATIONAL PUBLICATIONS

In Peer-reviewed International Scientific Journals :

1. D.Sarkar, S.Ahn, S.Kang and B.Basu, Fretting Wear of TiCN-Ni cermet: Influence of secondary carbide content, *P/M Sci and Tech Briefs*, 5 [2] (2003) 5-11.

2. J.Bera and D.Sarkar, Formation of $BaTiO_3$ from Barium Oxalate and TiO_2, *J Electroceramics*, 11(3), 131-137, 2003.

3. D. Sarkar, B.V. Manoj Kumar, S. Ahn, S. Kang, B. Basu, Fretting Wear Behavior of Ti(CN)-Based Advanced Cermets, *Key Engg Mater*, 1115-19, 264-268 (2004).

4. B.Basu, T.Venkateswaran and D.Sarkar, Pressureless Sintering and tribological properties of WC-ZrO_2 composites, *J Eur. Ceram. Soc.,* 25, 9, 2005, 1603-1610.

5. T.Venkateswaran, D.Sarkar and B.Basu, Tribological properties of WC-ZrO_2 Nanocomposites, *J Am. Ceram. Soc.*, 88 (3), 691-697, 2005.

6. D. Sarkar, S.J. Cho., M. C. Chu, S. S. Hwang, S. W. Park and B. Basu, Tribological properties of Ti_3SiC_2, *J Am. Ceram. Soc.*, 88 [11] 3245–3248 (2005).

7. D.Sarkar, B V Manoj Kumar and B.Basu, Understanding the fretting damage of Ti_3SiC_2 *J Eur. Ceram. Soc.,* 26, 13, 2006, 2441-2452.

8. D.Sarkar, B.Basu, M.J.Chu and S.J.Cho, R-Curve Behavior of Ti_3SiC_2 (*Ceramics Inter*, 2006, Available online 18 April 2006, doi:10.1016/j.ceramint.2006.01.002).

9. M.C.Chu, S.J.Cho, D.Sarkar, B.Basu, G.J.Yoon, H. M. Park, Oxidation-induced strengthening in ground SiC, *J Mater. Sci.,* 41 (15), 2006, 4978-4980.

10. T. Venkateswaran, D.Sarkar and B. Basu, WC–ZrO_2 composites: processing and unlubricated tribological properties, *Wear*, Volume 260, Issues 1-2, Pages 1-9, 2006.

11. D.Sarkar, B.Basu, M.J.Chu, S.J.Cho, Is Glass Infiltration Beneficial to Improve Fretting Wear Properties for Alumina? (In Press *J Am. Ceram. Soc,* 2006*)*.

12. D.Sarkar, S.Adak, N.K.Mitra, Preparation and Characterization of Al_2O_3-ZrO_2 Nanocomposite, Part I: Powder Synthesis and Transformation Behavior during Fracture *Composite Part A:* 38 (2007) 124–131.

13. D.Sarkar, S.Adak, S.J. Cho., M. C. Chu, N.K.Mitra, Influence of ZrO_2 content and grain size on the thermo-mechanical Properties of Nano-ZTA, (*Ceramics Inter,* 2006, Available online 27 December 2005, doi:10.1016/j.ceramint.2005.09.012).

14. D.Sarkar, D. Mohapatra, S. Bhattacharya, S.Adak, N.K.Mitra, Synthesis and Characterization of Sol-Gel Derived ZrO_2 doped Al_2O_3 Nanopowder (*Ceramics Inter,* 2006, Available online 12 September 2006, doi:10.1016/j.ceramint.2006.05.002).

15. D.Sarkar, D. Mohapatra, S. Roy, S. Bhattacharya, S.Adak, N.K.Mitra, Nanostructured Al_2O_3-ZrO_2 composites Synthesis by Sol-Gel Technique - Powder Processing and Microstructure (In Press, *J Mater Sci for special 'Nano-May-2006*' issue).

In International/National Conference Proceedings :

16. A.Agarwal, N.R.Bhattacharya, D.Sarkar and P.Sengupta, The Effect of Temperature and Humidity on the Storage Life of Magnesia-Carbon Ramming Mass" *Unified International Conference On Refractories* -1997,Vol II page 1531-1539.

17. P. Sengupta, N.R.Bhattacharya, D.Sarkar and P.K.Das Poddar, An attempt to development of Sulfate bonded alumino-silicate refractory, *International Refractories Congress*-1998,Vol-II 240-244.

Under Review in International Scientific Journals :

18. D. Mohapatra, D. Sarkar, Preparation of MgO-$MgAl_2O_4$ Composite for Refractory Application, (Under review, *Journal of Materials Processing Technology*, 2006)

19. A. Singh, P. Dasgupta, A. Basak, D. Sarkar, K. M. Purohit and S. Adak, Synthesis of Hydroxyapatite from Snail Shell, (Under review, *Ceramics International*, 2006)